

# 学位論文

## Direct Measurement of Quantum Back-Action in a Macroscopic System

巨視系における量子的反作用の直接測定

平成 25 年 12 月博士（理学）

申請

東京大学大学院理学系研究科

物理学専攻

松本 伸之

# Acknowledgements

This research had been advanced under the supervision of Kimio Tsubono until he retired in 2012. My ex-supervisor Kimio Tsubono had enabled me to apply myself to research. When I belonged to Tsubono laboratory, I was never worried about a shortage of research equipment, a research fund, and so on. He also provided some opportunities to work as a TA. He prepared the best academic research environment not only for me, but to everybody who belonged to the laboratory . This environment has been maintained by the incredible support of Yoichi Aso and my present supervisor, Masaki Ando, even after his retirement. I would also like to thank Yoichi Aso for his much advice, especially for building the experimental apparatus. I am thankful to Masaki Ando for being interested in my experiment and his encouragement. I'm not sure if I would have been able to finish this work without their help.

I have had the biggest fortune to work with talented and inspiring people. First, I have to mention Noriaki Ohmae. In 2011, when I almost finished work of those days, he provided me much advice, which included something leading to the present research. I was able to find the theme of the present research due to his advice.

Kenshi Okada and Yuta Michimura were incredible supporters with whom I argued most about the experiment, the future, and so on. Kenshi Okada is a man of executive ability, and an *unconventional* discussion with him proved to be the most fun for me. I also thank him for carrying out congratulations whenever possible. Yuta Michimura is a person who can advance things steadily. He and I joined the laboratory at about the same time, and together we studied various things mutually. He has always been my first person to discuss various matters. I also thank him for telling me how to use the spectrum analyzer and many other things. Their help was helpful for not only from a research aspect, but also in the other aspects.

Ayaka Shoda, Takafumi Ushiba and Masayuki Nakano were the members of the seminar when I noticed the idea of a triangular cavity. I would like to thank them for useful discussions in those days.

I would like to thank Gen Hayase, who became a famous person as the developer of the Marshmallow-like Gel. At the beginning, the experiment

---

using a new low-density mirror made of silica aerogel had been planned, and he had been advancing the development. That plan is still in progress. I would also like to thank Kazuyoshi Kanamori and Kazuki Nakanishi for their help. Kazuki Nakanishi recommended that I use a thin mirror. I was truly surprised and impressed by the aerogel that they were developing.

I am grateful to Shigenori Moriwaki, Kei Oikawa and Norikatsu Mio for their help. When I tried to adhere a wire to the tiny mirror, they let me use a microscope that they had been using. I would also like to thank Shigenori Moriwaki for his advice.

I further thank Michiko Kudoh and Ami Ito. They always supported me. I am sorry for not beginning this acknowledgement from the gratitude to Michiko Kudo.

I am grateful to Koji Ishidoshiro and Wataru Kokuyama for their giving help to me. I also thank other colleagues in Ando laboratory: Kazunori Shibata, Kentaro Komori, Yuya Kuwahara and Kodai Tejima.

I would like to thank members in Kawamura laboratory at ICRR: Seiji Kawamura, Shihori Sakata, Takumi Mori, Kazuhiro Agatsuma, Daniel Friedrich, and Masayuki Nakano for making me do the seminar. Based on the findings of the Shihori's doctoral thesis, I was able to design the experiment.

I would like to thank Kentaro Somiya for giving me the opportunity to go to Germany.

I am thankful to Yutaka Shikano for providing me with some opportunities to join the workshop. I also thank Yutaka for giving much advice for writing a paper, a theoretical understanding of the quantum measurement problem, and so on. He is an impressive man and also fun to work with.

I personally admire doctoral theses by Kenji Numata, Yoichi Aso, Keisuke Goda, Kirk Mackenzie, Henning Vahlbruch, Thomas Corbitt, and Haixing Miao, since their quality was extremely important for my research.

This research was supported by a Grant-in-Aid for JSPS Fellows No. 25 · 10490.

Finally, I am thankful to my parents for their patient encouragement and support.

# Abstract

---

In recent years, significant improvements in optical and mechanical elements have led to the development of the field of *optomechanics*, where mechanical oscillators couple optical fields via the radiation pressure of light. As for force measurements, such as gravitational-wave (GW) detectors, in which the mechanical oscillator is used as a probe of external force, its sensitivity has almost been limited by the standard quantum limit (SQL). Also, theoretical analysis has proven to be a connection between reaching the SQL imposed on the free mass (so-called free-mas SQL) and the generation of entanglement states, even between massive mechanical oscillators, such as suspended mirrors. Because of the massiveness, such states might have a key to investigate both the quantum measurement problem and quantum gravity. Therefore, optomechanics is not only useful as sensitive probes for the weak force, but also leads to possibilities of testing fundamental problems.

One of the key milestones toward the SQL is the observation of quantum back-action, which is a measurement-disturbance derived from the Heisenberg uncertainty principle (HUP). Until now, this effect has been observed below the mesoscopic mass scale using cold atom, NEMS (Nano Electro Mechanical Systems) oscillators and a MEMS (Micro Electro Mechanical Systems) oscillator. However, it had not yet been observed on the macroscopic scale beyond the Planck mass ( $\sim 22 \mu\text{g}$ ) because a strong thermal fluctuating force induced by the environment usually dominates measurements. To reduce the environmental noise, one can freely suspend a massive mirror in order to allow the mirror to be isolated from the environment. Although this isolation largely reduces the noise, a stationary radiation force of the light exposes the free mass to instability in conventional experiments utilizing a *linear* optical cavity. This technical limitation had been a significant issue because there is a fundamental compromise between the technical limitation and the sensitivity; sufficient tolerance with firm suspension makes the mass differ from the free mass, which results in an increase of the thermal fluctuating force.

In this thesis, we describe how by using a *triangular* optical cavity it is possible to overcome this limitation, and then describe the first-ever observa-

---

tion of quantum back-action imposed on a massive mirror (5 mg) beyond the Planck mass. The origin of quantum back-action is momentum transferred to the mirror by light upon its reflection. Concerning the coherent light, the photon number fluctuates according to a Poisson distribution, which caused the radiation pressure fluctuation, termed radiation pressure shot noise (RPSN). The pendulum mode excited by this force fluctuation was observed.

Based on the isolation method developed in this thesis and the experimental results achieved, the next plans for achieving its ground state and reaching/beating the free-mass SQL will be proposed.

**Keywords:** Optomechanics, Quantum back-action, Gravitational-wave detectors, Macroscopic quantum mechanics, Planck mass

# Contents

---

<b>Acknowledgements</b>	<b>i</b>
<b>Abstract</b>	<b>iii</b>
<b>1 Introduction</b>	<b>1</b>
1.1 Optomechanical effects . . . . .	1
1.1.1 Quantum noise limit . . . . .	5
1.2 Observation of quantum back-action . . . . .	9
<b>2 Theory of Optomechanics</b>	<b>11</b>
2.1 Optical cavity . . . . .	11
2.1.1 The quantized electromagnetic field . . . . .	11
2.1.2 The Heisenberg uncertainty principle . . . . .	13
2.1.3 States of light . . . . .	14
2.1.4 Optical cavity . . . . .	16
2.2 Mechanical oscillator . . . . .	20
2.2.1 Mechanical normal modes . . . . .	20
2.2.2 Mechanical dissipation & Dilution techniques . . . . .	22
2.3 Optomechanical system . . . . .	25
<b>3 Application of Optomechanics</b>	<b>32</b>
3.1 Towards gravitational wave astronomy . . . . .	32
3.1.1 Background of this section . . . . .	34
3.1.2 Back-action evasion method . . . . .	35
3.2 Test of quantum mechanics . . . . .	36
3.2.1 The requirement . . . . .	39
<b>4 Optical Torsional Spring</b>	<b>41</b>
4.1 Model of a triangular cavity . . . . .	42
4.2 Experimental setup . . . . .	44
4.3 Experimental results & Discussions . . . . .	47

---

<b>5</b>	<b>Experimental Setup</b>	<b>49</b>
5.1	All aspects of the experiment . . . . .	50
5.2	Partial aspects of the experiment . . . . .	56
5.2.1	Mechanical oscillator . . . . .	56
5.2.2	Intensity stabilized laser . . . . .	59
5.2.3	Actuator efficiency . . . . .	65
5.2.4	Detection system, control system and vacuum system . . . . .	66
<b>6</b>	<b>Experimental Results</b>	<b>71</b>
6.1	Optical characterization . . . . .	72
6.2	Mechanical characterization . . . . .	73
6.3	Optomechanical characterization . . . . .	76
6.4	Direct measurement of quantum back-action . . . . .	78
6.5	Discussions . . . . .	80
<b>7</b>	<b>The Future</b>	<b>82</b>
7.1	Towards ground-state cooling . . . . .	83
7.2	Towards beating the SQL . . . . .	85
	<b>Conclusion</b>	<b>87</b>
	<b>A Intensity stabilization</b>	<b>89</b>
	<b>BIBLIOGRAPHY</b>	<b>91</b>

# CHAPTER 1

## Introduction

---

In this chapter, we provide a short history of optomechanical effects. This chapter presents the historical and physical background of this research.

### 1.1 Optomechanical effects

Light has momentum, and can thus exert pressure on objects through the exchange of momentum between the light and the objects. This fact was postulated by Johannes Kepler, who noted that the dust tails of comets pointed away from the Sun during a comet transit [1] in the 17<sup>th</sup> century. James Clerk Maxwell theoretically predicted radiation pressure by his Maxwell's equations in 1873. On the other hand, Adolfo Giuseppe Bartoli predicted it from the view point of thermodynamics in 1876 [2]. The first experimental demonstration of the (stationary) pressure of light was made by using a torsional balance by Peter Lebedew in 1901 [3]. Ernest Nichols and Gordon Hull also conducted a similar, but advanced, experiment in 1903 [4]. In 1909, Albert Einstein derived the statistics of the radiation-pressure force fluctuation acting on a movable mirror including the “radiation friction” (frictional force) [5]. This analysis allowed him to reveal the dual wave-particle nature of blackbody radiation.

Since then, various types of optomechanical effects have been both theoretically and experimentally explored using various types of optomechanical devices. Examples are given below.

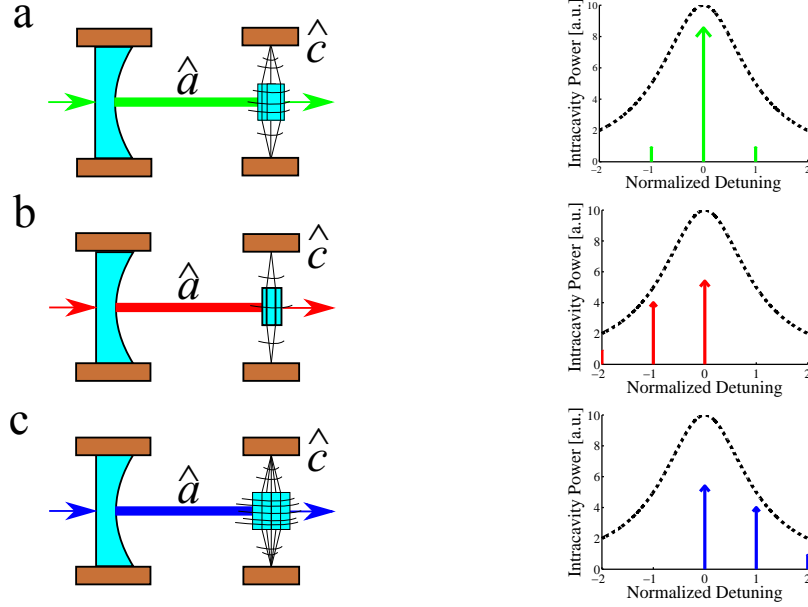


Figure 1.1: **Basic cavity optomechanical effects.** Consider an optical cavity that consists of fixed and movable mirrors. **Left:** These figures are schematic representations of three types of detuning: on-resonance, red-detuning (i.e., the frequency of the input light is lower than the resonant frequency of the optical cavity) and blue-detuning (i.e., the frequency is higher than the resonant). Here,  $\hat{a}$  is a photon annihilation operator and  $\hat{c}$  is a phonon annihilation operator of the movable mirror (See Chapter 2). **Right:** It shows the intracavity power as a function of the detuning normalized by a resonant frequency of the movable mirror. **a:** The input light is modulated by the resonant frequency of the movable mirror, such that the upper (lower) sideband component of the light acquires (sheds) energy from the mirror. (This is analogous to the generation of Stokes and anti-Stokes sidebands in Raman scattering.) As a result, there is no exchange of energy between the light and the mirror. This interaction can be characterized by  $(\hat{a} + \hat{a}^\dagger)\hat{x}$ , and thus it can be used as the displacement measurement. Here,  $\hat{x}$  represents the position of the movable mirror. **b:** The upper sideband component is enhanced by the optical cavity, and thus the motion of the mirror is damped (cooling). This interaction can be characterized by  $\hat{a}^\dagger\hat{c} + \hat{a}\hat{c}^\dagger$ , and thus it can be used to coherently transfer the state between the light and the mirror [56, 57]. **c:** The lower sideband component is enhanced by the optical cavity, and thus the motion of the mirror is anti-damped (heating). This interaction can be characterized by  $\hat{a}\hat{c} + \hat{a}^\dagger\hat{c}^\dagger$ , and thus it can be used to create the various types of entanglement states [42, 43, 45, 46, 47, 48].

- **Cooling**

The cooling of an object by a laser is one of the most attractive features of optomechanics. This cooling effect mainly occurs due to the frictional (damping) force of light. Because a laser field is almost in its ground state (e.g., infrared optical field having an effective temperature of about 15,000 K), this damping force reduces the velocity of the object without introducing other thermal fluctuating forces (i.e., this effect is “cold” damping, similar to that described in Ref. [6]). As a result, the object is effectively cooled.

So far, the cooling method has been widely used from atom-scale to kg-scale objects, partially for trapping [7, 8, 9], achieving the ground state [10, 11, 12] and eliminating technical limitations [13, 14, 15]. Another aspect of the cooling (or heating) is the optical spring effect [16, 17, 18, 19], which not only changes the damping constant of the mechanical system, but it also changes the spring constant. This effect is certainly useful for examining the quantum behavior of mechanical oscillators *free* from external control. In our case, the (double) optical spring effect [20] was one of three technical features of the experiment (See Chapters 5 & 6).

- **Instability**

The first cavity optomechanical experiment demonstrated bistability induced by the radiation-pressure force acting on a macroscopic mirror in the optical domain [21]. Since then, various types of instability, such as parametric instability [22, 23], have been reported. In our case, overcoming an optical anti-torsional effect (so-called Siddles-Sigg instability [24, 25]) was one of three technical features in the experiment. We realized it by an optical torsional spring effect in a triangular cavity, which was independently shown by Daniel Sigg and myself (See Chapter 4).

- **Measurement limit**

Braginsky represented the fundamental consequences of the Heisenberg uncertainty principle (HUP) [26], and demonstrated that it imposes a limit on any force measurement since the 1960s [27, 28]. This fundamental quantum limit for the measurement sensitivity is called the standard quantum limit (SQL). SQL is the sum of components derived from the quantization of light, and of a mechanical oscillator, which

lead to the generation of inevitable fluctuation, called *vacuum fluctuation* of the light and *zero-point fluctuation* of the oscillator, respectively (details are described in the next subsection). SQL applies universally to all devices that use a mechanical oscillator as a probe mass.

To overcome this limit, various types of techniques, such as input-squeezing [29, 30, 31], modification of the dynamics of the mechanical oscillator by an optical spring [32, 33, 34] and the measurement of a conserved dynamical quantity of the mechanical oscillator [35, 36], have been proposed. Today, all of them, which can overcome the SQL imposed on the free mass (so-called free-mass SQL) within a certain frequency range, are called QND (quantum nondemolition) measurements [37]. The QND measurement is a stronger necessary condition than the observation of quantum back-action for the generation of macroscopic entanglement states (See Chapter 3).

- **Squeezing**

When an oscillator is fluctuated by quantum radiation pressure fluctuation (i.e., observation of quantum back-action), a quadrature variance of the light is squeezed due to self-phase modulation, like that of Kerr squeezing in fibers [38, 39]. This effect is called ponderomotive squeezing, and has been observed using cold atoms [40], a NEMS oscillator [41] and a MEMS oscillator [14] after the observation of quantum back-action. Ponderomotive squeezing has a key to perform the QND measurement (See Chapter 3).

- **Entanglement**

Entanglement is a physical phenomenon in which multiple subsystems can only be described with reference to each other. In other words, entanglement can be considered as to be correlations between small quantum fluctuations around a carrier field in the frequency domain [42]. Entanglement is at the heart of physical investigations not just because of its critical role in marking the boundary between classical and quantum world, but also because of its key role for realizing quantum information processing.

Optomechanical coupling via radiation pressure is a promising approach to generate entanglement states, e.g. entanglement between mechanical degrees of freedom [42, 43, 44, 45] and entanglement between a light field and a mechanical oscillator [46, 47, 48, 49].

In addition, optomechanical effects have been expected to be utilized as an engine via radiation pressure [50] or a radiometer [51], and as a form of quantum memory [52, 53], and so on [54, 55, 56, 57]. Especially, the former was excellently realized as a space solar sail. IKAROS (Interplanetary Kite-craft Accelerated by Radiation Of the Sun) of the Japan Aerospace Exploration Agency (JAXA) [58] is the first spacecraft to successfully demonstrate the solar-sail technology in interplanetary space.

As described above, the optomechanical effects have a potential to allow for breakthroughs in a large variety of fields, such as precise weak-force measurements, quantum information, fundamental tests of quantum mechanics, and even satellite development. Effects induced by *stationary* radiation pressure, such as laser cooling, instability and the solar sail have been experimentally realized. However effects induced by quantum *fluctuation* of radiation pressure, such as the generation of entanglement states, squeezed states and reaching/beating the SQL are still challenging to be realized, particularly in the macroscopic regime.

### 1.1.1 Quantum noise limit

Measuring weak forces is at the heart of modern physics from the macroscopic scale to the atomic scale, e.g. gravitational-wave (GW) detectors [59, 60, 61, 62] and atomic-force microscopy [63]. In spite of the progress of lasers, optical components and mechanical oscillators, no optomechanical systems have yet reached the *free-mass* SQL [64]. The free-mass SQL is a next goal after the observation of quantum back-action, because it not only limits the sensitivity, but also defines a benchmark noise spectral density at which the door is opened to experimentally investigate macroscopic quantum mechanics, such as the generation of macroscopic entanglement states [44]. Here, we show the details of the SQL.

The force noise (double-sided) spectral density of the SQL,  $S_{\text{FF,SQL}}^{(2)}$  is given by [65]

$$S_{\text{FF,SQL}}^{(2)}(\omega) = \hbar |\chi_m(\omega)|^{-1} + 2\hbar\omega_m\gamma_m m. \quad (1.1)$$

Here,  $\omega$  is the angular frequency,  $\hbar$  the Dirac constant,  $m$  the mass of the oscillator,  $\gamma_m$  the amplitude mechanical decay rate (i.e., the mechanical quality factor  $Q_m$  is given by  $Q_m = \omega_m/2\gamma_m$ ) and  $\chi_m$  the mechanical susceptibility. The first term arises from the quantization of light and the second term

arises from mechanical quantization. This equation represents that the effect of the oscillator’s quantization can be easily removed at above the resonant frequency [65, 66] if the mechanical decay rate is small (i.e., high mechanical quality factor), as shown in Fig. 1.2. It is worth pointing out that this is close to the actual situation of GW detectors, in which a quasi-freely suspended mirror with eigenfrequencies of around 1 Hz and a very high quality factor about  $10^7$ , are monitored of above 10 Hz. Therefore, Eq. (1.1) is usually written as  $S_{\text{FF,SQL}}^{(2)}(\omega) = \hbar |\chi_m(\omega)|^{-1}$  in the field of GW detectors; this is just called “the SQL” in the field (in this thesis, we use the term ‘usual SQL’ as meaning this). Also, this equation tells us that: (i) both of the components in Eq. (1.1) are equal at the resonance; and (ii) the usual SQL, the free-mass SQL, and the SQL are all equal far above the resonance of the mechanical oscillator.

The part of the SQL derived from the quantization of light is understandable, as described below. Light is a continuous electromagnetic wave, and its energy is delivered in discrete packets, called photon. Concerning the light emitted by a laser, which is a good approximation to a coherent state and has Poissonian statistics, the photons arrive randomly on a mirror. This randomness, which is called the “vacuum fluctuation”, produces both direct phase noise and indirect phase noise, called shot noise and radiation pressure shot noise, respectively. The vacuum fluctuation of the *phase* quadrature (orthogonal to a carrier field) directly gives rise to phase noise (i.e., sensing noise), which is inversely proportional to the optical power, while the vacuum fluctuation of the *amplitude* quadrature (parallel to the carrier) creates a random radiation-pressure force on the mirror (i.e., force noise) that results in optical phase noise, which is directly proportional to the optical power. In general, the shot noise dominates at higher frequency and the radiation pressure shot noise dominates at lower frequency because the mechanical susceptibility of an oscillator has a frequency dependence of  $f^{-2}$  beyond a resonant frequency (furthermore, the quantum radiation pressure fluctuation does not have any frequency-dependence within the cavity linewidth; see Chapter 2). If these two types of noise are *not* correlated, they will induce a lower bound on the detector sensitivity independent of the optical power, which leads to the SQL [65, 67], as shown in Fig. 1.2.

Another part of the SQL derived from the quantization of an oscillator is understandable as described below. The oscillator consists of various types of normal modes, and its energy is delivered in discrete packets, called phonon.

We now consider the specific normal mode, and naturally assume that the other modes are sufficiently sparse, such that there is no spectral overlap with each other. For a specific mechanical mode being sufficiently cooled [e.g., by laser cooling and direct cooling], which is a good approximation to the ground state and has zero-point energy, the oscillator undergoes inevitable fluctuation. This fluctuation, which is called the “zero-point fluctuation”, also limits the sensitivity as force noise.

So far, no experiment has yet reached the free-mass SQL, since the thermal fluctuating force induced by a thermal bath is usually far above the free-mass SQL. In general, reaching the free-mass SQL requires that (i) the force noise be dominated by quantum back-action, (ii) the readout noise be dominated by shot noise, and (iii) the readout laser power be optimized such that their sum is minimized. Therefore, our observation of quantum back-action imposed on the macroscopic oscillator is the first step toward the free mass SQL. On the other hand, reaching the SQL on the resonance represents the ground-state cooling, because the approximate phonon occupation number  $k_B T / \hbar \omega_m$  represents the ratio of the thermal fluctuating force to the SQL (See Eq. (7.1)). On the macroscopic scale, ground-state cooling is very difficult, because the cavity condition is usually *bad* (See Chapter 2) due to the low resonant frequency of the oscillator. This results in an increase of the quantum back-action, even if the thermal excitation can be removed. The double optical spring technique [20] (See Chapter 2) and a *back-action evasion* method (See Chapter 3) might enable the macroscopic mirror to reach its ground state.

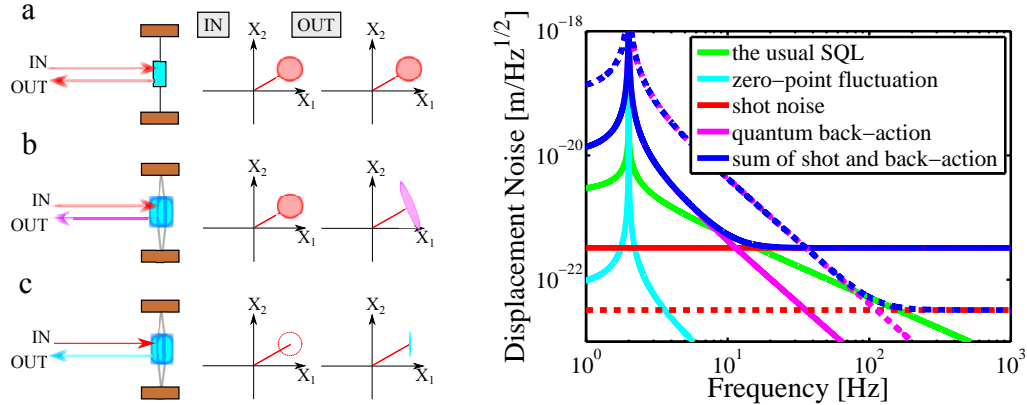


Figure 1.2: **Various types of quantum noise.** Consider measurement of weak force imposed on a mirror (the force is encoded in the sequence of displacements) using an interferometer. **Left:** Schematic representations, which are called *ball-on-stick* pictures, of quantum noise. The amplitude of the laser is represented as a stick, while the fluctuation of light is represented as a ball on the stick. Here,  $X_1$  is the amplitude quadrature and  $X_2$  is the phase quadrature (See Chapter 2). In the conventional scheme, the displacement fluctuation is read out using information concerning the phase quadrature. **a:** Shot noise is drawn. It limits the sensitivity, even if there is no zero-point fluctuation of the mirror, because it is just the *optical* effect. **b:** Quantum back-action is drawn. It limits the sensitivity even if there is no zero-point fluctuation because it is the *optomechanical* effect induced by the quantum radiation pressure fluctuation through the mechanical susceptibility. Due to the self-phase modulation, the state of light is squeezed such that the noise level of the phase quadrature increases. This effect is enhanced at lower frequency according to the frequency dependence of the mechanical susceptibility. As a result, the noise level of the quantum back-action is equal to the shot noise and more. **c:** Zero point-fluctuation is drawn. It limits the sensitivity even if there is no vacuum fluctuation of light because it is just the *mechanical* effect. **Right:** Shows the amplitude power spectrum of the quantum noise for a 1-kg test mass. The contribution of the zero-point fluctuation subtracted from the SQL [(usual for the field of the GW detectors) depicted as a green line], the contribution of zero-point fluctuation (cyan), quantum back-action (magenta), shot noise (red) and the sum of the shot noise and the radiation pressure shot noise (blue) are shown. The dotted magenta and red represent the case of 10-times higher power than the above. If the sum of the quantum back-action and the shot noise is minimized with respect to the input power, the minimum noise is equal to the (free-mass) SQL.

## 1.2 Observation of quantum back-action

Lastly in this chapter, we provide a short history of the observation of quantum back-action.

The first measurement of quantum back-action was performed using cold atoms by Dan M. Stamper-Kurn *et al.* in 2008 [68]. Using copper wires embedded in an atom chip, they magnetically trapped and loaded an ultracold ensemble of Rb 87 (the number of atoms is  $10^5$ ) into the cavity. They then transferred the ensemble into a laser trap (wavelength of 850 nm), a very far detuned longitudinal mode of the cavity. The probe light (wavelength of 780 nm) was coupled to another longitudinal mode, which drives the ensemble through the optical dipole force. Its transmission was recorded while exiting the ensemble, because the ensemble behaves similarly to that of a dispersive piece of glass, changing the effective length of the cavity (i.e., “dispersive” optomechanical coupling). By blue-detuning the probe laser, such that it deposited phonons into the ensemble, the quantum back-action could be observed as a heating of the ensemble. As a result, they were able to measure the cavity-light-induced heating of the intracavity atomic ensemble. After this measurement, they also measured the ponderomotive squeezing in 2012 [40].

The second measurement was performed using a photonic crystal nanobeam by Amir H. Safavi-Naeini *et al.* in 2012 [69]. At first, they reported their experiment as being an observation of the quantum motion of a nanomechanical resonator. Farid Ya. Khalili *et al.* [65] showed that the results of this experiment not only characterized the quantum motion, but also demonstrated the existence of quantum back-action noise, just as in 2012.

In their experiment, they used a patterned silicon nanobeam, which formed an optomechanical crystal capable of localizing both optical and acoustic waves. An optical fiber taper was used to couple light evanescently into the breathing mechanical mode of the silicon optomechanical device (effective mass off 311 fg). The cavity was designed to have two optical resonances, one for cooling (wavelength is 1460 nm) and one for readout of mechanical motion (wavelength is 1545 nm). In this case, the cooling had the key to characterize the zero-point motion. After this measurement, they also measured ponderomotive squeezing in 2013 [41].

The third measurement was performed using a SiN membrane (effective mass of 7 ng) by Tom P. Purdy *et al.* in 2013 [13]. The membrane motion could be coupled to a cavity through the dispersive interaction. This inter-

action imprinted phase and amplitude modulations onto transmitted laser light, thus allowing for readout of the membrane motion. In addition, the laser applied an optical gradient force to the membrane, while pushing it toward higher optical intensity. They used one laser source (wavelength of 1064 nm) being split into two components by an acousto-optical modulator (AOM): one for cooling and the other for readout of the mechanical motion. In this case, the cooling was used for reducing the technical difficulties (e.g., parametric instability), not for enhancing the ratio of the quantum back-action to thermal noise, similarly to our case (See Chapter 6). After this measurement, they also measured the ponderomotive squeezing in 2013 [14].

A fourth measurement was performed using a suspended 5-mg mirror by us [15]. Concerning the macroscopic scale, there have been intensive studies at MIT, NAOJ, etc. [70, 71, 72] since the mid-2000s. The MIT group used a 1-g suspended mirror, and they reported the usefulness of the double optical spring [20]. The NAOJ group (currently, ICRR group) used a 22-mg suspended mirror, and they reported the measurement of an anti-torsional spring effect [25] in a linear optical cavity. Based on their findings, we were able to observe quantum back-action. The details will be described after this chapter.

# CHAPTER 2

## Theory of Optomechanics

In this chapter, we describe the basic aspects of optical cavities, mechanical resonators, and cavity optomechanical systems. This chapter presents the basic concepts and mathematical tools for understanding later chapters.

### 2.1 Optical cavity

There are two equally important aspects in the physical theory: the mathematical formalism of the theory, and its intuitive interpretation. In this section, we describe the mathematical formalism for the quantization of light and the result; we also present intuitive interpretations of classical/quantum fluctuation: the *ball-on-stick* picture. The interested reader is referred to excellent textbooks [73, 74] for further details.

#### 2.1.1 The quantized electromagnetic field

In 1927, Paul Dirac proposed quantization of the electromagnetic field to solve the problem of the wave-particle duality. In this quantum theory, each mode of a radiation field can be understood by a quantized simple harmonic oscillator. The properties of the quantized field are introduced in the context of an optical cavity mode with angular frequency of  $\omega_{\mathbf{k}}$ . The positive and negative components of the electric field can be written in terms of the boson creation and annihilation operators,  $\hat{a}_{\mathbf{k}}^\dagger$  and  $\hat{a}_{\mathbf{k}}$ , and the spatial mode

function,  $\mathbf{u}(\mathbf{r})$ :

$$\mathbf{E}^{(+)}(\mathbf{r}, t) = i \sum_{\mathbf{k}} \left( \frac{\hbar\omega_{\mathbf{k}}}{2\epsilon_0} \right)^{1/2} \hat{a}_{\mathbf{k}} \mathbf{u}(\mathbf{r}) \exp(-i\omega_{\mathbf{k}}t), \quad (2.1)$$

$$\mathbf{E}^{(-)}(\mathbf{r}, t) = -i \sum_{\mathbf{k}} \left( \frac{\hbar\omega_{\mathbf{k}}}{2\epsilon_0} \right)^{1/2} \hat{a}_{\mathbf{k}}^{\dagger} \mathbf{u}(\mathbf{r})^* \exp(i\omega_{\mathbf{k}}t). \quad (2.2)$$

Here  $\hbar$  is the Dirac constant and  $\epsilon_0$  is the permittivity of free space. The sum of the positive and negative components gives the whole electric field,

$$\mathbf{E}(t) = i \sum_{\mathbf{k}} \left( \frac{\hbar\omega_{\mathbf{k}}}{2\epsilon_0} \right)^{1/2} \left[ \hat{a}_{\mathbf{k}} \mathbf{u}(\mathbf{r}) \exp(-i\omega_{\mathbf{k}}t) - \hat{a}_{\mathbf{k}}^{\dagger} \mathbf{u}(\mathbf{r})^* \exp(i\omega_{\mathbf{k}}t) \right]. \quad (2.3)$$

The creation and annihilation operators are dimensionless and satisfy the boson commutation relations,

$$[\hat{a}_{\mathbf{k}}, \hat{a}_{\mathbf{k}'}] = [\hat{a}_{\mathbf{k}}^{\dagger}, \hat{a}_{\mathbf{k}'}^{\dagger}] = 0, \quad [\hat{a}_{\mathbf{k}}, \hat{a}_{\mathbf{k}'}^{\dagger}] = \delta_{\mathbf{k}\mathbf{k}'}. \quad (2.4)$$

These commutation relations account for an important distinction between classical and quantum optics. In classical optics, an equivalent of equation (2.3) can be found by replacing the annihilation and creation operators with complex field amplitudes. The amplitudes in classical optics commute, and thus they are not limited by the Heisenberg uncertainty relation and its consequences. In quantum mechanics, however, the operators must be Hermitian in order to represent observable quantities. The annihilation and creation operators are not Hermitian, and are thus not observables. They can be written in terms of a Hermitian operator pair for the amplitude quadrature,  $\hat{X}_1$ , and the phase quadrature,  $\hat{X}_2$ :

$$\hat{a} = \frac{1}{2}(\hat{X}_1 + i\hat{X}_2), \quad (2.5)$$

$$\hat{a}^{\dagger} = \frac{1}{2}(\hat{X}_1 - i\hat{X}_2), \quad (2.6)$$

The quadrature operators for the amplitude and phase are:

$$\hat{X}_1 = \hat{a} + \hat{a}^{\dagger}, \quad (2.7)$$

$$\hat{X}_2 = -i(\hat{a} - \hat{a}^{\dagger}). \quad (2.8)$$

The amplitude and phase quadratures represent non-commuting observable parameters. The operator for an arbitrary quadrature,  $\xi$ , can be defined using a linear combination of  $\hat{X}_1$  and  $\hat{X}_2$ ,

$$\hat{X}_\xi = \hat{X}_1 \cos(\xi) + \hat{X}_2 \sin(\xi). \quad (2.9)$$

### 2.1.2 The Heisenberg uncertainty principle

The Heisenberg uncertainty principle (HUP) [26] quantifies the ultimate precision of continuous measurement of non-commuting observable parameters, as described in Chapter 1. HUP tells us that if any two observable parameters,  $\hat{O}_1$  and  $\hat{O}_2$ , satisfy the commutation relation,

$$[\hat{O}_1, \hat{O}_2] = \xi, \quad (2.10)$$

they are bounded by HUP,

$$\Delta\hat{O}_1\Delta\hat{O}_2 \geq \frac{|\xi|}{2}, \quad (2.11)$$

where  $\Delta\hat{O}$  is the standard deviation of the operator  $\hat{O}$ . The standard deviation is defined by

$$\Delta\hat{O} = \sqrt{\langle\hat{O}^2\rangle - \langle\hat{O}\rangle^2}. \quad (2.12)$$

The variance of the operator is the square of the standard deviation,

$$V = (\Delta\hat{O})^2. \quad (2.13)$$

The commutator relation of the amplitude and the phase quadratures of the electromagnetic field is

$$[\hat{X}_1, \hat{X}_2] = 2i, \quad (2.14)$$

and thus HUP is

$$\Delta\hat{X}_1\Delta\hat{X}_2 \geq 1. \quad (2.15)$$

This relation shows that the trade-off between the fluctuation of the amplitude quadrature and that of the phase quadrature. Therefore, this also shows the trade-off between the shot noise and the radiation pressure shot noise for the force measurement.

### 2.1.3 States of light

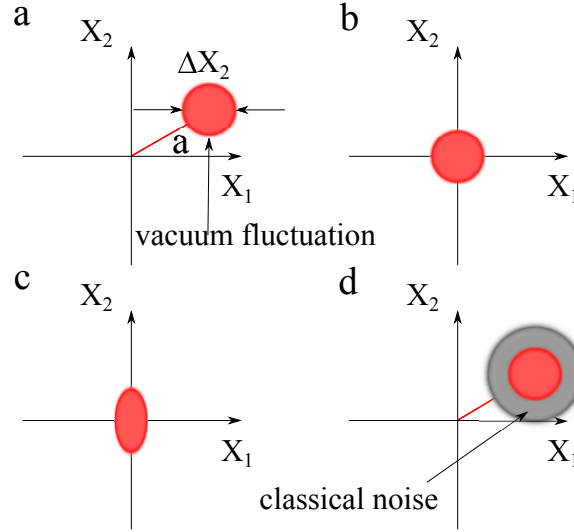


Figure 2.1: **Ball-and-stick pictures for states of light.** **a:** Coherent state is represented. **b:** Vacuum state is represented. **c:** Amplitude squeezed state is represented. **d:** Classically noisy state is represented.

Here, several common states (a coherent state, a vacuum state, a squeezed state of light, and a classically noisy state) are described and shown in *ball-on-stick* pictures. In the ball-on-stick pictures, the classical steady-state coherent amplitude of the field is represented as a stick, while the fluctuation of light is represented as a ball on the stick, which is analogous to the phasor diagram used in classical physics where the orthogonal axes are the real and imaginary parts of an electromagnetic field. Various states of light can be visually understood by this.

- **The coherent state**

A coherent state is a minimum-uncertainty state with equal uncertainties in the two quadrature components, so that

$$\Delta\hat{X}_1 = \Delta\hat{X}_2 = 1. \quad (2.16)$$

The quadrature fluctuations of the coherent state have no frequency dependence, and obey Poissonian statistics. For the coherent state,

the sidebands are randomly distributed in phase, and thus there is no special phase. Although the coherent state is theoretically realized by the laser, the laser light has excess noise below the MHz region, whereas we measured a pendulum motion at around 130 Hz. Therefore, stabilization of the laser intensity fluctuation is necessary for us (See Chapter 5).

- **The vacuum state**

A vacuum state is also a minimum-uncertainty state with equal uncertainties in the two quadrature components, but it has no coherent amplitude ( $\bar{a} = \langle \hat{a}(t) \rangle = 0$ ). It always occupies all frequency, spatial, and polarization modes. The vacuum state is important in quantum-optics experiments, since it enters optical systems in any unfilled ports of the beam splitters, cavities, and partially transmissive mirrors. In our case, the vacuum state prevents stabilization of the laser intensity noise from achieving the minimum uncertainty level (See Chapter 5 & Appendix).

- **The squeezed state**

A squeezed state is a non-classical state in which fluctuation is reduced below the symmetric quantum limit in one quadrature component. In order to satisfy HUP, the standard deviation of the orthogonal quadrature must be greater than the quantum noise limit and the product of the two quadratures greater than or equal to unity. If the amplitude quadrature is reduced, it is called the amplitude squeezed state, and vice versa. Thus, the minimum uncertainty amplitude squeezed state, for example, has

$$\Delta \hat{X}_1 = 1/z, \quad (2.17)$$

$$\Delta \hat{X}_2 = z, \quad (2.18)$$

where  $z$  is a real and a positive number. The amplitude-squeezed state is shown in Fig. 2.1.

- **Classically noisy states**

In general, lasers produce non-minimum-uncertainty states, which have excess noise of classical origin at sideband frequencies below the MHz region. The classical noise of a laser is often many times greater than

the quantum noise in both quadratures,

$$\Delta\hat{X}_1 \geq 1, \Delta\hat{X}_2 \geq 1. \quad (2.19)$$

The classical noise can be reduced via: passive noise suppression using an optical cavity [75]; active feedback control (See Chapter 5 & Appendix); or both. The noisy state is characterized by comparing with the shot noise level in units of dB (so-called the relative to the shot-noise level) and its coherent laser power in units of  $1/\text{Hz}^{1/2}$  (so-called relative intensity noise). The former is an useful index for quantum measurements, such as observation of the quantum back-action and generation of the squeezed state. The latter is an useful index for force measurement, such as that used in gravitational-wave detectors.

### 2.1.4 Optical cavity

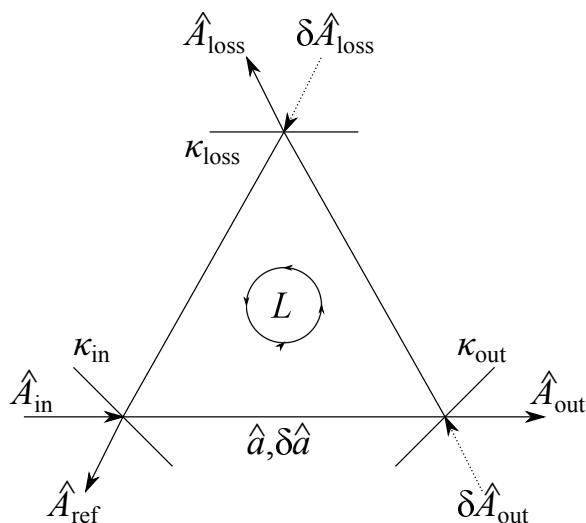


Figure 2.2: **Layout of the optical cavity.** Consider a cavity composed of two mirrors: an input coupler, with a decay rate of  $\kappa_{\text{in}}$ ; an output coupler, with a decay rate of  $\kappa_{\text{out}}$ ; a mirror to represent intracavity loss, with a decay rate of  $\kappa_{\text{loss}}$ ; and the roundtrip length of the cavity,  $L$ . The cavity mode is labeled  $\hat{a}$ . The extracavity fields are:  $\hat{A}_{\text{in}}, \hat{A}_{\text{out}}, \hat{A}_{\text{ref}}, \hat{A}_{\text{loss}}, \delta\hat{A}_{\text{out}}$  and  $\delta\hat{A}_{\text{loss}}$ .

Fabry-Perot interferometers, often referred to as (optical) cavities, consist of two or more partially transmissive mirrors in order to make the light

resonate inside it. In this section, the equation of motion for a cavity mode is introduced; we then obtain the reflected and transmitted fields using this equation.

### Equation of motion

Consider the empty cavity shown in Fig. 2.2. It is made of three partially transmissive optics labeled, in, out, and l, referring to the input coupler, the output coupler, and the partially transmissive mirror used to simulate losses, respectively. The equation of motion for cavity mode  $\hat{a}$  in units of  $\sqrt{\text{photon}}$  is [76]

$$\dot{\hat{a}} = -(i\omega_c + \kappa)\hat{a} + \sqrt{2\kappa_{\text{in}}}\hat{A}_{\text{in}}e^{-i\omega_A t} + \sqrt{2\kappa_{\text{out}}}\hat{A}_{\text{out}} + \sqrt{2\kappa_{\text{loss}}}\hat{A}_{\text{loss}}, \quad (2.20)$$

where the driving field,  $A_{\text{in}}$ , in units of  $\sqrt{\text{photon/s}}$  has a coherent amplitude at frequency  $\omega_A$ ; the other fields,  $A_{\text{out}}$  and  $A_{\text{loss}}$ , are assumed to be in the vacuum state. The cavity mode has a resonant frequency of  $\omega_c$ .

The equation of motion can be written in the rotating frame of reference by setting

$$\hat{a} \rightarrow \hat{a}e^{-i\omega_A t}, \quad (2.21)$$

$$\hat{A}_{\text{in}} \rightarrow \hat{A}_{\text{in}}e^{-i\omega_A t}, \quad (2.22)$$

and thus

$$\dot{\hat{a}} = (i\Delta - \kappa)\hat{a} + \sqrt{2\kappa_{\text{in}}}\hat{A}_{\text{in}} + \sqrt{2\kappa_{\text{out}}}\hat{A}_{\text{out}} + \sqrt{2\kappa_{\text{loss}}}\hat{A}_{\text{loss}}, \quad (2.23)$$

where  $\Delta = \omega_A - \omega_c$  is the cavity detuning [i.e., the positive (negative) detuning means the blue-detuning (red-detuning)]. In the mean-field approximation [77, 78], the amplitude decay rates for each mirror are given by the amplitude transmissivity divided by the round trip time,  $\tau = L/c$ , where  $L$  is the roundtrip of the cavity. That is,

$$\begin{aligned} \kappa_{\text{in}} &= \frac{\sqrt{T_{\text{in}}}}{\tau} \simeq \frac{T_{\text{in}}}{2\tau} \\ \kappa_{\text{out}} &\simeq \frac{T_{\text{out}}}{2\tau} \\ \kappa_{\text{loss}} &\simeq \frac{1 - \mathcal{L}_c}{2\tau}, \end{aligned} \quad (2.24)$$

where  $\mathcal{L}_c$  is the cavity round-trip loss. The total decay rate is given by

$$\kappa = \kappa_{\text{in}} + \kappa_{\text{out}} + \kappa_{\text{loss}}. \quad (2.25)$$

In the steady state, the cavity mode can be found by setting  $\dot{\hat{a}} = 0$  and considering the time-independent component  $\bar{a}$ . Given that the steady state amplitudes of the fields  $\bar{A}_{\text{out}} = \bar{A}_{\text{loss}} = 0$ , the steady state cavity mode is given by

$$\bar{a} = \frac{\sqrt{2\kappa_{\text{in}}}}{\kappa - i\Delta} \bar{A}_{\text{in}}. \quad (2.26)$$

This equation enables us to obtain the reflected and transmitted fields as a function of detuning in the following way. We are also interested in the Fourier components of the cavity mode. These can be found by Fourier transforms of the operators,

$$Q(\omega) = \int_{-\infty}^{\infty} Q(t) \exp(-i\omega t) dt, \quad (2.27)$$

for  $Q = \hat{a}, \hat{A}_{\text{in}}, \hat{A}_{\text{out}},$  and  $\hat{A}_{\text{loss}}$ . The equation of motion in the frequency domain is

$$-i\omega\delta\hat{a} = (i\Delta - \kappa)\delta\hat{a} + \sqrt{2\kappa_{\text{in}}}\delta\hat{A}_{\text{in}} + \sqrt{2\kappa_{\text{out}}}\delta\hat{A}_{\text{out}} + \sqrt{2\kappa_{\text{loss}}}\delta\hat{A}_{\text{loss}}, \quad (2.28)$$

where  $\omega$  is the sideband frequency. Simply put, this fluctuating term induces the quantum back-action force (details are described in Sec. 2.3).

### Reflected and transmitted fields

Using the cavity input-output relations [76], the reflected field,  $A_{\text{ref}}$  and transmitted field,  $A_{\text{trans}}$ , can be determined:

$$\begin{aligned} A_{\text{trans}} &= \sqrt{2\kappa_{\text{out}}}a - A_{\text{out}}, \\ A_{\text{ref}} &= \sqrt{2\kappa_{\text{in}}}a - A_{\text{in}}, \end{aligned} \quad (2.29)$$

which give

$$\bar{A}_{\text{trans}} = \frac{2\sqrt{\kappa_{\text{in}}\kappa_{\text{out}}}}{\kappa - i\Delta} \bar{A}_{\text{in}}, \quad (2.30)$$

$$\bar{A}_{\text{ref}} = \frac{2\kappa_{\text{in}} - \kappa + i\Delta}{\kappa - i\Delta} \bar{A}_{\text{in}}. \quad (2.31)$$

The amplitude transmissivity and reflectivity of the cavity can be defined by the parameters

$$t(\Delta) = \frac{\bar{A}_{\text{trans}}}{\bar{A}_{\text{in}}} = \frac{2\sqrt{\kappa_{\text{in}}\kappa_{\text{out}}}}{\kappa - i\Delta}, \quad (2.32)$$

$$r(\Delta) = \frac{\bar{A}_{\text{ref}}}{\bar{A}_{\text{in}}} = \frac{2\kappa_{\text{in}} - \kappa + i\Delta}{\kappa - i\Delta}. \quad (2.33)$$

From these equations, one can experimentally estimate important parameters, i.e,  $\kappa$ ,  $\kappa_{\text{in}}$  and  $\kappa_{\text{out}}$  (See Chapter 6).

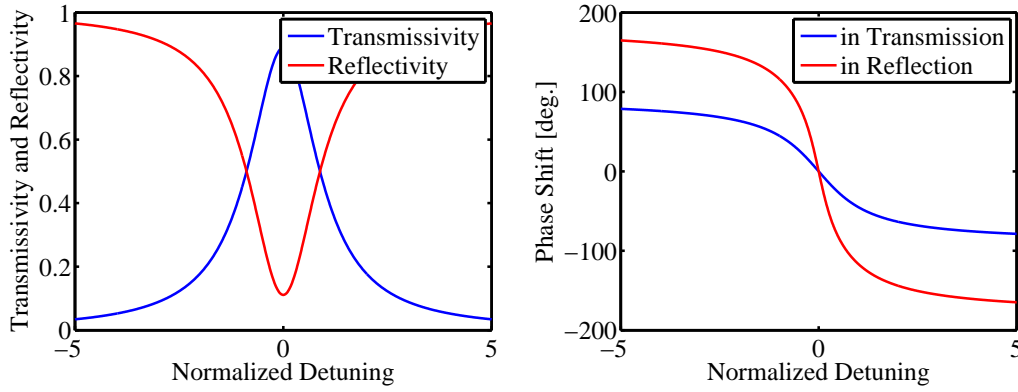


Figure 2.3: **Optical cavity.** These show the reflected and transmitted fields as a function of detuning normalized by the cavity decay rate. **Left:** The (power) reflectivity and transmissivity are shown. **Right:** The phase shifts in reflection and transmission are shown.

## 2.2 Mechanical oscillator

In this section, we describe the mechanical oscillator, especially concerning mechanical dissipation. Mechanical dissipation is one of the most important parameters, because the Fluctuation-Dissipation Theorem (FDT) [79] connects the spectrum of the thermal fluctuating force to the mechanical dissipation in the system, which is given by

$$S_{\text{FF,th}}^{(2)} = \frac{2k_{\text{B}}T}{\omega} \text{Im}\chi_{\text{m}} \propto T_{\text{th}}\gamma_{\text{m}}. \quad (2.34)$$

Here,  $k_{\text{B}}$  is the Boltzmann constant,  $T_{\text{th}}$  is the temperature of the thermal bath,  $\chi_{\text{m}}$  is the mechanical susceptibility derived below,  $\omega$  is the sideband frequency,  $\gamma_{\text{m}}$  is the mechanical damping rate (i.e, it represents the dissipation) and  $m$  is the mass of the mechanical oscillator. This equation represents that the reduction of the thermal noise requires a low mechanical dissipation and a low bath temperature. To reduce the dissipation, we used two types of *dilution* techniques. Details are described below.

### 2.2.1 Mechanical normal modes

Consider a suspended mirror (i.e., pendulum) having a resonant frequency of  $\omega_{\text{m}}$ , naturally assuming that the mode spectrum is sufficiently sparse such that there is no spectral overlap with other mechanical modes, such as a rocking mode and a violin mode. This condition can be easily satisfied by choosing appropriate parameters [80]. The equation of motion for the position of the mirror,  $x(t)$ , can be described by

$$m\ddot{x} + 2m\gamma_{\text{m}}\dot{x} + m\omega_{\text{m}}^2x = F_{\text{ext}}. \quad (2.35)$$

Here,  $m$  denotes the mass of the pendulum,  $\gamma_{\text{m}}$  the amplitude damping rate (i.e., the mechanical quality factor is  $Q_{\text{m}} = \omega_{\text{m}}/2\gamma_{\text{m}}$ ),  $\omega_{\text{m}}$  the resonant frequency of the oscillator, and  $F_{\text{ext}}(t)$  the external force acting on the mirror. Even if there is no external force, it is given by the thermal fluctuating force.

To solve this equation, we again introduce the Fourier transform via  $x(\omega) = \int_{-\infty}^{\infty} dt \exp(-i\omega t)x(t)$ . Then, the mechanical susceptibility  $\chi_{\text{m}}(\omega)$  connecting the external force to the displacement of the oscillator is given by

$$\chi_{\text{m}}(\omega) \equiv \frac{x(\omega)}{F_{\text{ext}}(\omega)} = (m(\omega_{\text{m}}^2 - \omega^2) + 2im\omega\gamma)^{-1}. \quad (2.36)$$

The stationary response is given by  $\chi_m(0) = (m\omega_m^2)^{-1} = 1/k_m$ , where  $k_m$  is the spring constant. In our experiment, the pendulum was effectively cooled down to about 40 mK by laser cooling, but it is still a *classical* pendulum (i.e., thermal occupation number  $k_B T/\hbar\omega_m$  is about  $7 \times 10^7$ ). Therefore, although quantum mechanics is not necessary until now, it is necessary after the pendulum reaches its ground state.

A quantum-mechanical treatment of the mechanical harmonic oscillator leads to the Hamiltonian

$$\hat{H} = \hbar\omega_m \hat{c}^\dagger \hat{c} + \frac{1}{2} \hbar\omega_m. \quad (2.37)$$

Here, the phonon creation,  $\hat{c}^\dagger$ , and annihilation,  $\hat{c}$ , operators have been introduced similarly to Eqs. (2.7), (2.8), with

$$\hat{x} = x_{\text{zpf}}(\hat{c} + \hat{c}^\dagger), \quad \hat{p} = -im\omega_m x_{\text{zpf}}(\hat{c} - \hat{c}^\dagger), \quad (2.38)$$

where

$$x_{\text{zpf}} = \sqrt{\frac{\hbar}{2m\omega_m}} \quad (2.39)$$

is the zero-point fluctuation amplitude of the mechanical oscillator. The quantity  $\hat{c}^\dagger \hat{c}$  is the phonon number operator, whose average is denoted by  $\bar{n} = \langle \hat{c}^\dagger \hat{c} \rangle$ . In general, the mechanical oscillator is coupled to a high-temperature bath, and thus the average phonon number will evolve according to the expression

$$\frac{d}{dt} \langle n \rangle = -2\gamma_m (\langle n \rangle - \bar{n}_{\text{th}}). \quad (2.40)$$

For an oscillator that is initially in the ground state, the time dependence of the occupation is given by

$$\frac{d}{dt} \langle n \rangle_{t=0} = 2\bar{n}_{\text{th}}\gamma_m \simeq \frac{k_B T_{\text{th}}}{\hbar Q_m}, \quad (2.41)$$

where  $\bar{n}_{\text{th}}$  is the average phonon number of the thermal bath and  $T_{\text{th}}$  is the temperature of the thermal bath. Equation (2.41) represents the thermal decoherence rate, because it gives the inverse time of the absorption of a phonon from the environment. This expression shows that in order to attain a low thermal decoherence, a high mechanical quality factor,  $Q_m$ , and a

low temperature bath are important. In addition, from this equation, the number of coherent oscillations in the presence of thermal decoherence is given by  $\omega_m \hbar Q_m / k_B T_{\text{th}} = Q_m \cdot f_m \times (h / k_B T_{\text{th}})$ . Therefore, the “ $Q_m \cdot f_m$ ” product quantifies the decoupling of the mechanical resonator from a thermal environment. Note that full coherence over one mechanical period is obtained for  $Q_m \cdot f_m = k_B T_{\text{th}} / \hbar$ , i.e.  $Q_m \cdot f_m > 6 \times 10^{12}$  Hz is a minimum requirement for room-temperature quantum optomechanics. One might consider that satisfying the criteria is impossible on the macroscopic scale; however, the *dilution* techniques described below enable us to realize it.

### 2.2.2 Mechanical dissipation & Dilution techniques

The loss of mechanical excitations, i.e. phonons, is quantified by the amplitude dissipation rate,  $\gamma_m = \omega_m / 2Q_m$ . Here, we introduce the loss mechanisms:

- Viscous damping is mainly caused by interactions with the surrounding gas atoms. A resistance force proportional to the velocity is applied to the oscillator. In our case, the gas damping will become an issue in future (See Chapter 7).
- Clamping losses are due to radiation of elastic waves into the substrate through the supports of the oscillator. In our case, a thin tungsten wire is clamped between two aluminum plates at the top, while a mirror is attached to the wire using an epoxy glue at the bottom (See Chapter 6). Although this lossy configuration has sufficient quality factor for observing the quantum back-action, it will not be sufficient for future experiments. Therefore, we must change it to other relatively lossless materials, such as stainless steels (See Chapter 7).
- A thermoelastic damping is a fundamental anharmonic effect, which is caused by heat flow along the temperature gradients. This effect often causes problems, such as a mirror thermal noise, because the temperature gradients often occur at around the laser beam spot on the mirror. In our case, the mirror thermal noise has been negligible until now; however, it will also become an issue in the future (See Chapters 5 & 7).
- An intrinsic loss of a material is caused by the relaxation of intrinsic defect states in the bulk or surface of the material. In general, intrinsic

loss could not be measured directly because of the loss coming from the support for the measurement. To solve this problem, a nodal support system, which does not introduce any external loss to the sample by supporting it at their nodal points, was proposed by Kenji Numata in 2000 [81]. Since then, this technique has been used [82, 83]. In our case, it was estimated using a torsional mode (See Chapter 6), similarly to that described in Ref. [84].

The various dissipation processes contribute independently to the overall mechanical losses, and hence add up incoherently. The resulting mechanical quality factor,  $Q_{\text{total}}$ , is given by  $1/Q_{\text{total}} = \sum_i 1/Q_i$ , where  $i$  labels the different loss mechanisms.

Since the loss of the energy is only associated with the elastic part of the stored energy, the mechanical dissipation can be mitigated by storing most of the mechanical energy in a nearly lossless gravitational or optical potential, thereby strongly diluting the effect of the dissipation.

- **Gravitational dilution:** The total mechanical loss of an oscillator is diluted with gravity by a factor of  $k_{\text{grav}}/k_{\text{el}}$ , where  $k_{\text{grav}}$  and  $k_{\text{el}}$  are the gravitational and elastic spring constants [85]. As a result, the mechanical quality factor becomes  $k_{\text{grav}}/k_{\text{el}}$ -times larger (i.e.,  $Q_m \cdot f_m$  becomes  $k_{\text{grav}}/k_{\text{el}}$ -times larger). In our case, an ultimate thin wire (the radius is  $1.5 \mu\text{m}$ ) assures that the amount of energy stored in the pendulum is dominated by the gravitational potential over the elastic bending energy of the wire. More concretely, the mechanical dissipation is about 1000-times diluted (See Chapter 5 & 6).
- **Optical dilution:** Mechanical energy is stored in the lossless potential provided by the optical restoring forces, which dilutes the effects of internal material dissipation. As a result, the minimum requirement for room-temperature quantum optomechanics imposed on “ $Q_m \cdot f_m$ ” is  $(f_{\text{eff}}/f_m)^2$ -times mitigated. Here,  $f_{\text{eff}}$  is the effective resonant frequency of the mechanical oscillator trapped by the optical spring. In the case of the *soft* suspension, such as the suspended mirror, this effect is relatively increased, and thereby it is often used with pendulums [86, 87, 88]. In our case, the original  $Q_m \cdot f_m$  is about  $1 \times 10^6$  Hz, which is about  $6 \times 10^6$ -times lower than the original requirement, even though the gravitational potential increases the mechanical quality factor. The optical spring further reduces the difference to

$6 \times 10^6 \cdot (2.2/130)^2 \simeq 2 \times 10^3$ . This is due to the double optical-spring technique [20] (See Chapters 5 & 6). In the future, the difference can be furthermore reduced (See Chapter 7).

The dilution techniques mentioned above have a key to experimentally investigate the macroscopic quantum mechanics because any macroscopic object is strongly affected by thermal decoherence as just it is.

## 2.3 Optomechanical system

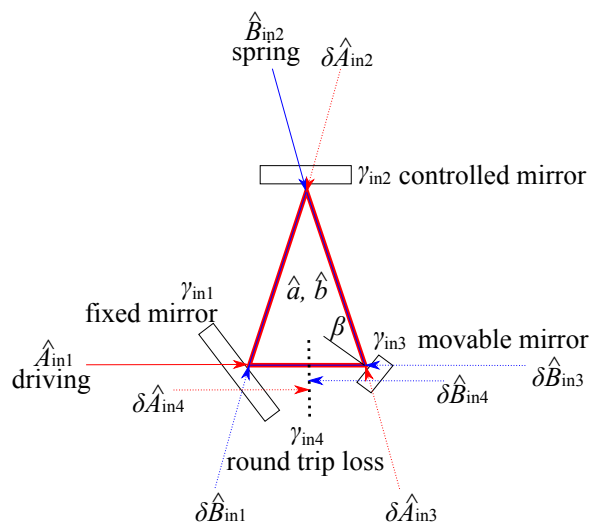


Figure 2.4: **Layout of the triangular cavity.** The cavity consists of three mirrors: the input coupler for the driving beam, with a decay rate of  $\kappa_{in1}$ ; the input coupler for the spring beam, with a decay rate of  $\kappa_{in2}$ ; the movable mirror, with a decay rate of  $\kappa_{in3}$ ; and a mirror to represent intracavity loss, with a decay rate of  $\kappa_{in4}$ . The cavity mode is labeled  $\hat{a}$  and  $\hat{b}$ . The extracavity fields are:  $\hat{A}_{in1}$ ,  $\delta\hat{A}_{in2}$ ,  $\delta\hat{A}_{in3}$ ,  $\delta\hat{A}_{in4}$ ,  $\delta\hat{B}_{in1}$ ,  $\hat{B}_{in2}$ ,  $\delta\hat{B}_{in3}$ , and  $\delta\hat{B}_{in4}$

**Theoretical derivation of quantum back-action** Here, we calculate the quantum back-action in the optomechanical system shown in Fig 2.4. We again start from Newton's law to describe the mechanical response,

$$m\ddot{x} + 2m\gamma_m\dot{x} + k_mx = F, \quad (2.42)$$

where  $m$  is the mass of the movable mirror (mechanical oscillator),  $\omega_m$  is the mechanical resonant frequency,  $\gamma_m$  is the mechanical amplitude decay rate,  $k_m$  is the mechanical spring constant, and  $x$  is the position for the mirror. To derive the mechanical susceptibility, we Fourier transform Eq.(2.42) according to the following conventions:  $f(\omega) \equiv \int_{-\infty}^{\infty} dt f(t) \exp(-i\omega t)$ ,

$$\chi_m \equiv \frac{x}{F} = \frac{1}{m(\omega_m^2 - \omega^2 + i2\omega\gamma_m)}. \quad (2.43)$$

Secondly, we calculate the response of an optomechanical system to two independent laser driving fields. The Hamiltonian describing the optomechanical coupling [89] can be written and linearized in the form

$$\begin{aligned}\hat{\mathcal{H}} &= \hbar\omega_c(x)\hat{a}^\dagger\hat{a} + \hbar\omega_c(x)\hat{b}^\dagger\hat{b} + \hat{\mathcal{H}}_\kappa \\ &\simeq \hbar\omega_c\hat{a}^\dagger\hat{a} + \hbar\omega_c\hat{b}^\dagger\hat{b} + \hbar g\hat{a}^\dagger\hat{a}x + \hbar g\hat{b}^\dagger\hat{b}x + \hat{\mathcal{H}}_\kappa,\end{aligned}\quad (2.44)$$

where  $g = 2\omega_c \cos\beta/L$  is the optomechanical coupling constant,  $\omega_c$  is the cavity resonance frequency,  $\beta$  is the incident angle on the movable mirror,  $L$  is the round-trip length and  $\hat{\mathcal{H}}_\kappa$  represents the optical input and output coupling; and  $\hat{a}$  and  $\hat{b}$  are the annihilation operators (cavity modes) for two counterpropagating directions in the triangular cavity, respectively. The Heisenberg Langevin equations of motion for the cavity modes are:

$$\dot{\hat{a}} = -(\kappa + i\omega_c)\hat{a} - ig_a x \hat{a} + \sum_1 \sqrt{2\kappa_1} \hat{A}_1, \quad (2.45)$$

$$\dot{\hat{b}} = -(\kappa + i\omega_c)\hat{b} - ig_b x \hat{b} + \sum_1 \sqrt{2\kappa_1} \hat{B}_1, \quad (2.46)$$

where the  $\kappa_{\text{in}1}, \kappa_{\text{in}2}, \kappa_{\text{in}3}$  are the cavity amplitude decay rates for each mirror,  $\kappa_{\text{in}4}$  is the decay rate for the cavity round-trip loss and  $\kappa$  is the total decay rate;  $\hat{A}_1$  and  $\hat{B}_1$  are the input optical fields. The equation of motion can be written in a rotating frame of reference by setting  $\hat{a} = \exp(-i\omega_a t)\hat{a}$  and linearized in the following form:

$$\dot{\delta\hat{a}} = -(\kappa - i\Delta_a)(\bar{a} + \delta\hat{a}) - iG_a \delta x + \sqrt{2\kappa_{\text{in}1}} \bar{A}_{\text{in}1} + \sum_1 \sqrt{2\kappa_1} \delta\hat{A}_1, \quad (2.47)$$

$$\dot{\delta\hat{b}} = -(\kappa - i\Delta_b)(\bar{b} + \delta\hat{b}) - iG_b \delta x + \sqrt{2\kappa_{\text{in}2}} \bar{B}_{\text{in}2} + \sum_1 \sqrt{2\kappa_1} \delta\hat{B}_1, \quad (2.48)$$

where  $\Delta_a = \omega_a - \omega_c - G_a \bar{x}$  and  $\Delta_b = \omega_b - \omega_c - G_b \bar{x}$  are the cavity detuning;  $G_a = \bar{a}g$  and  $G_b = \bar{b}g$  are the light-enhanced optomechanical couplings for the linearized regime;  $\bar{a}$  and  $\bar{b}$  are the average parts for each cavity mode;  $\delta\hat{a}$  and  $\delta\hat{b}$  are the fluctuating parts for each cavity mode;  $\bar{A}_{\text{in}1}$  and  $\bar{B}_{\text{in}2}$  are the real valued coherent amplitudes for input lasers;  $\delta\hat{A}_1$  and  $\delta\hat{B}_1$ , for  $l = \text{in}1, \text{in}2, \text{in}3, \text{in}4$  are the vacuum fluctuation entering from each port.

The average intracavity field amplitudes are described by Eqs. (2.47) and

(2.48):

$$\bar{a} = \frac{\sqrt{2\kappa_{\text{in}1}}}{\kappa - i\Delta_a} \bar{A}_{\text{in}1}, \quad (2.49)$$

$$\bar{b} = \frac{\sqrt{2\kappa_{\text{in}2}}}{\kappa - i\Delta_b} \bar{B}_{\text{in}2}. \quad (2.50)$$

From these equations, the intracavity power is given by

$$\begin{aligned} \bar{P}_{\text{circ}} &= \frac{\hbar\omega_c |a|^2}{\tau} + \frac{\hbar\omega_c |b|^2}{\tau} \\ &= \bar{P}_{\text{in}1, \text{circ}} + \bar{P}_{\text{in}2, \text{circ}} \\ &= \frac{2\kappa_{\text{in}1}}{\tau(\kappa^2 + \Delta_a^2)} \bar{P}_{\text{in}1} + \frac{2\kappa_{\text{in}2}}{\tau(\kappa^2 + \Delta_b^2)} \bar{P}_{\text{in}2}, \end{aligned} \quad (2.51)$$

where  $\tau$  is the cavity round-trip time.

The fluctuation components of Eqs. (2.47) and (2.48) are similarly at given by

$$\delta\hat{a} = -(\kappa - i\Delta_a)\delta\hat{a} - iG_a\delta x + \sum_1 \sqrt{2\kappa_1}\delta\hat{A}_1, \quad (2.52)$$

$$\delta\hat{b} = -(\kappa - i\Delta_b)\delta\hat{b} - iG_b\delta x + \sum_1 \sqrt{2\kappa_1}\delta\hat{B}_1. \quad (2.53)$$

In terms of the frequency components, these can be rewritten by

$$\delta\hat{a} = \chi_a(-iG_a\delta x + \sum_1 \sqrt{2\kappa_1}\delta\hat{A}_1), \quad (2.54)$$

$$\delta\hat{b} = \chi_b(-iG_b\delta x + \sum_1 \sqrt{2\kappa_1}\delta\hat{B}_1). \quad (2.55)$$

Here,  $\chi_a = (\kappa + i(\omega - \Delta_a))^{-1}$  and  $\chi_b = (\kappa + i(\omega - \Delta_b))^{-1}$  are the cavity susceptibilities for the two modes. These lead to forces induced by the cavity modes, being applied to the movable mirror, which are given by:

$$\bar{F}_{\text{BA}} = -\frac{(g_a + g_b)\tau}{\omega_c} \bar{P}_{\text{circ}}, \quad (2.56)$$

$$\delta F_{\text{BA}} = i\hbar|G_a|^2\delta x(\chi_a(\omega) - \chi_a^*(-\omega)) + i\hbar|G_b|^2\delta x(\chi_b(\omega) - \chi_b^*(-\omega)), \quad (2.57)$$

$$\begin{aligned} \delta\hat{F}_{\text{BA}} &= -\hbar G_a^* \chi_a(\omega) \sum_1 \sqrt{2\kappa_1}\delta\hat{A}_1 - \hbar G_a \chi_a^*(-\omega) \sum_1 \sqrt{2\kappa_1}\delta\hat{A}_1^\dagger \\ &\quad - \hbar G_b^* \chi_b(\omega) \sum_1 \sqrt{2\kappa_1}\delta\hat{B}_1 - \hbar G_b \chi_b^*(-\omega) \sum_1 \sqrt{2\kappa_1}\delta\hat{B}_1^\dagger, \end{aligned} \quad (2.58)$$

where  $\bar{F}_{\text{BA}}$  is the average back-action force,  $\delta F_{\text{BA}}$  is the dynamic back-action, which influences the dynamics of the harmonically bound mirror, and  $\delta \hat{F}_{\text{BA}}$  is the quantum back-action force.

From the dynamic back-action, the optical spring effect is

$$\begin{aligned} K(\omega) &= -\frac{\delta F_{\text{BA}}}{\delta x} = 2\hbar|G_{\text{a}}|^2 \frac{\Delta_{\text{a}}}{(\kappa + i\omega)^2 + \Delta_{\text{a}}^2} + 2\hbar|G_{\text{b}}|^2 \frac{\Delta_{\text{b}}}{(\kappa + i\omega)^2 + \Delta_{\text{b}}^2} \\ &= \frac{8P_{\text{in1,circ}}\omega_{\text{c}}}{Lc} \frac{\Delta_{\text{a}} \cos^2(\beta)}{(\kappa + i\omega)^2 + \Delta_{\text{a}}^2} + \frac{8P_{\text{in2,circ}}\omega_{\text{c}}}{Lc} \frac{\Delta_{\text{b}} \cos^2(\beta)}{(\kappa + i\omega)^2 + \Delta_{\text{b}}^2}. \end{aligned} \quad (2.59)$$

The experiment is performed under the ‘‘slowly varying’’ condition,  $\omega \ll \sqrt{\Delta_{\text{a}}^2 + \kappa^2}$ ; then, the spring effect can be written by

$$\begin{aligned} K &= 2\hbar|G_{\text{a}}|^2 \left[ \frac{\Delta_{\text{a}}}{\kappa^2 + \Delta_{\text{a}}^2} - \frac{2i\kappa\Delta_{\text{a}}}{(\kappa^2 + \Delta_{\text{a}}^2)^2}\omega \right] + 2\hbar|G_{\text{b}}|^2 \left[ \frac{\Delta_{\text{b}}}{\kappa^2 + \Delta_{\text{b}}^2} - \frac{2i\kappa\Delta_{\text{b}}}{(\kappa^2 + \Delta_{\text{b}}^2)^2}\omega \right] \\ &\equiv K_{\text{opt}} + i\Gamma_{\text{opt}}\omega. \end{aligned} \quad (2.60)$$

This condition is also called the ‘‘bad’’ cavity condition because of the weakness of the cooling effect due to the decay of light, itself. Under this condition, the intracavity optical power is largely increased as an effect of the laser cooling being increased, and thereby the back-action is also increased. If the light-enhanced optomechanical coupling constant,  $G$ , is larger than  $\sqrt{m\kappa\gamma_{\text{m}}\omega_{\text{m}}}/\hbar$ , the back-action becomes larger than the SQL on resonance of the mechanical oscillator. Therefore, in general, this condition is not appropriate for the laser cooling of the object for achieving its ground state. The optical dilution described in the above section has the key to reduce this difficulty. On the other hand, in the resolved sideband regime, defined as  $\omega_{\text{m}} \gg \kappa$ , one can reduce the occupation number to  $(\kappa/2\omega_{\text{m}})^2$  [90, 91]. Therefore, this condition is called the ‘‘good’’ cavity condition.

This spring modifies the dynamics of the mirror as

$$\omega_{\text{eff}}^2 = \omega_{\text{m}}^2 + \frac{K_{\text{opt}}}{m}, \quad (2.61)$$

$$\gamma_{\text{eff}} = \gamma_{\text{m}} + \frac{\Gamma_{\text{opt}}}{2m}, \quad (2.62)$$

which indicates that the positive (negative) rigidity is always accompanied by negative (positive) damping. In either case, the system is unstable if we use a single optical spring. To stabilize the system, one can use a feedback

control; however, it is difficult to control if we use a tiny oscillator. An appropriate alternative is to implement the idea of the double optical spring [20], by inputting two lasers to the cavity at different frequencies. One laser with a small detuning provides a large positive damping, while the other higher input-power beam with a large detuning provides a strong restoring force. The resulting system is self-stabilized with both positive rigidity and positive damping, as shown in Fig 2.5. In addition, unlike mechanical springs, the optical spring effect does not change the thermal excitation spectrum of the mirror, since the optical field is almost in its ground state (in our case, the infrared optical field has an effective temperature of 15,000 K). We can measure the quantum back-action force fluctuation as a displacement fluctuation via the effective susceptibility,  $\chi_{\text{eff}}$ .

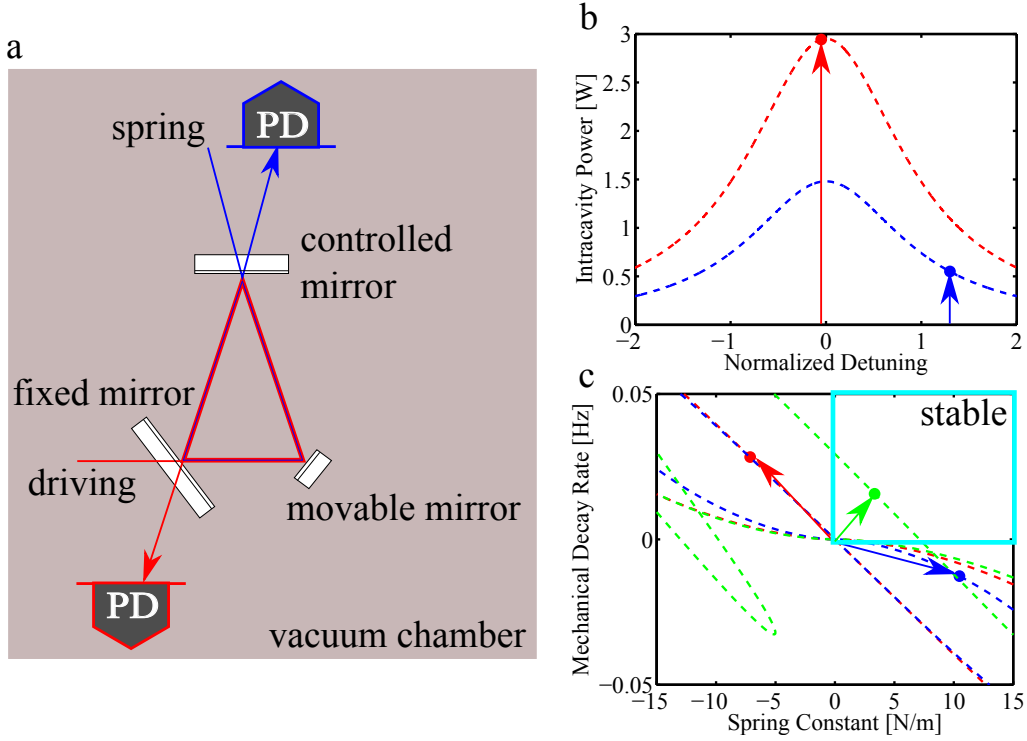


Figure 2.5: **The double optical spring effect in our experiment.** **a:** The driving (red) and spring (blue) beams incident on the fixed and controlled mirrors, respectively. **b:** The intracavity power and detuning for each beam. The red and blue points show both laser-cavity detuning and the intracavity power. The dashed red and blue curves show the optical power as a function of the cavity detuning for each beam. The driving beam dominates the quantum back-action due to the higher intracavity power than the spring beam. **c:** The optical spring effect. The red point represents the driving beam at  $\Delta_a/\kappa = -0.05$ , the blue point represents the spring beam at  $\Delta_b/\kappa = +1.3$ , and the dashed green represents their sum. The dashed red and blue curves show parametric plots of the optical spring as a function of the detuning for each beam, and the dashed green curve is their sum. Inside the cyan frame, both the spring and the mechanical decay rates have a positive values, and thus the mirror is stably trapped. It is impossible for single optical spring.

The double-sided force spectrum,  $S_{FF,q}^{(2)}$ , is written as

$$\begin{aligned}
S_{FF,q}^{(2)} &= \langle \delta \hat{F}_{BA}(-\omega) \delta \hat{F}_{BA}(\omega) \rangle \\
&= 2\hbar^2 \kappa |G_a|^2 |\chi_a(-\omega)|^2 + 2\hbar^2 \kappa |G_b|^2 |\chi_b(-\omega)|^2 \\
&= 2N_{\text{in1,circ}} \frac{\hbar^2 g^2}{\kappa} \left( 1 + \left( \frac{\omega + \Delta_a}{\kappa} \right)^2 \right)^{-1} + 2N_{\text{in2,circ}} \frac{\hbar^2 g^2}{\kappa} \left( 1 + \left( \frac{\omega + \Delta_b}{\kappa} \right)^2 \right)^{-1}.
\end{aligned} \tag{2.63}$$

Therefore, the quantum back-action is given by  $|\chi_{\text{eff}}|^2 S_{FF,q}^{(2)}$ . In practice, a laser has a classical intensity fluctuation generating the ‘‘classical’’ back-action force. This effect is given by

$$\begin{aligned}
S_{FF,c}^{(2)} &= 2(B_{\text{in1}} - 1) \hbar^2 \kappa_{\text{in1}} |G_a|^2 (|\chi_a(\omega)|^2 + |\chi_a(-\omega)|^2) \\
&\quad + 2(B_{\text{in2}} - 1) \hbar^2 \kappa_{\text{in2}} |G_b|^2 (|\chi_b(\omega)|^2 + |\chi_b(-\omega)|^2),
\end{aligned} \tag{2.64}$$

where  $B_{\text{in1}}$  and  $B_{\text{in2}}$  are the relative shot noise levels for each beam. In the slowly varying regime, the ratio of the classical back-action to the quantum back-action for each beam is  $S_{FF,c,j}^{(2)}/S_{FF,q,j}^{(2)} \propto \kappa_j/\kappa$ , for  $j = \text{in1, in2}$ , which enables us to estimate the requirement for the intensity stability of the input beam.

# CHAPTER 3

## Application of Optomechanics

In this chapter, we describe how an observation of the quantum back-action is related to the gravitational-wave (GW) detectors and macroscopic quantum mechanics.

### 3.1 Towards gravitational wave astronomy

Gravitational waves are ripples of space-time curvature that propagate across the universe at the speed of light. They were theoretically predicted from the Einstein equation in the General Theory of Relativity [92]. Their existence was indirectly proved by an observation of a binary pulsar, PSR1913+16 [93]. The observed decrease in the period of its revolution agrees with the theoretical expectation of the orbital decay due to gravitational radiation. There is no doubt that gravitational waves exist. However, gravitational waves have not been directly detected yet, because of the weakness of the gravitational interaction. On the other hand, due to the weakness, these waves enable us to view the dark ages of the universe through direct measurements. Their direct observation requires modern laser technology and highly sensitive measurements at almost the standard quantum limit (SQL). Furthermore, for gravitational-wave astronomy, the GW detection rate should be increased through ultimate sensitive measurements beyond the (free-mass) SQL.

In the past two decades, an international array of ground-based, kilometer-scale Michelson interferometers composed of quasi-freely suspended mirrors (shown in Fig. 3.1), has been set up aiming at the first direct observation. The Michelson interferometer makes it possible to naturally decompose the optical fields and the corresponding motion of the suspended mirrors into common and differential modes. Since the Michelson interferometer is usually operated on a dark fringe (i.e., the beam splitter can be regarded as

having a perfect reflectivity for the carrier light), ideally only optical signals induced by the differential motion of the suspended mirrors exit the unused port shown in Fig. 3.1. This signal enables us to measure the gravitational waves because one can consider the gravitational waves as being tidal force imposed on the suspended mirror [94].

These interferometric GW detectors have been operating all over the world. GEO600 in Germany [61] is currently the only large detector taking data, while the two LIGO observatories in the US [59] and the Virgo detectors in Italy [62] are being upgraded to their advanced state, and KAGRA in Japan [60] is under construction. These ground-based GW detectors target signals at audio frequencies in a band of 10 Hz to 10 kHz above the resonant frequency of the suspended mirror. At higher frequencies, their sensitivity will be limited by the shot noise. This shot-noise arises from the vacuum fluctuation of light, which enters the interferometer through the unused port. At lower frequencies, the quantum noise will be dominated by the quantum back-action (radiation pressure shot noise, RPSN) from the same vacuum fluctuation giving shot noise, but at the orthogonal quadrature phase. At any given frequency, the spectral density of the quantum noise is the sum of those of the shot noise, the RPSN, and a term arising from their correlation. Note that the zero-point fluctuation of the mirror does not affect the sensitivity because the GW detectors only pay attention to the sideband frequency above the resonant frequency of the suspended mirror, in which the mirror can be considered to be a free mass. The standard quantum limit (SQL) on the force measurement arises when the two noise sources are uncorrelated [27, 67]. Therefore, the correlation between the shot noise and the RPSN becomes a key to overcome the SQL.

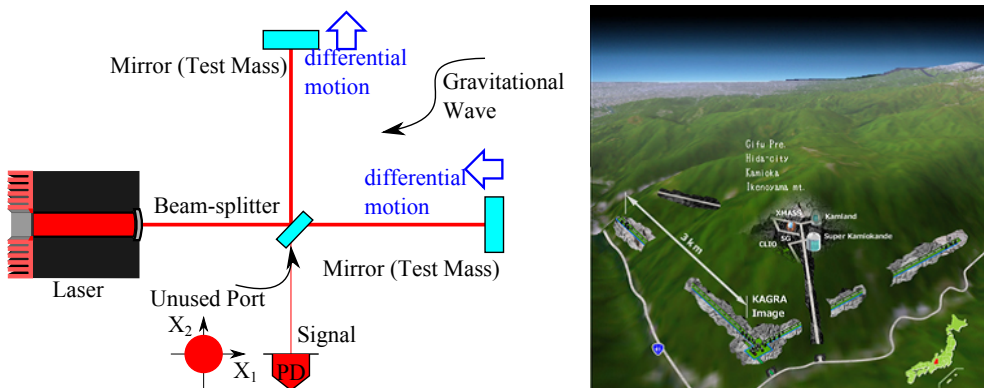


Figure 3.1: **Schematic of the gravitational-wave detector.** **Left:** A classic Michelson interferometer as a GW detector consists of a laser, a 50/50 beamsplitter (BS), two suspended test mass mirrors and a photodetector (PD). The gravitational wave can be considered to be a tidal force imposed on the mirrors, thereby shortening the length of one arm while expanding the length of the other. The vacuum fluctuation entering from the unused port masks the GW signal because the detector is operated at the dark fringe. **Right:** The GW detector in Japan is called KAGRA, with an armlength of 3 km [60].

### 3.1.1 Background of this section

One of the most important features of future GW detectors is that they will operate at sufficiently high laser powers such that the quantum back-action acting on the suspended mirrors will become a dominant force at a lower frequency band (typically below 100 Hz). The effects of the radiation pressure will be manifested mainly in two ways in terms of the *fluctuation* of the pressure or the *stationary* pressure; the vacuum fluctuation will drive the mirror and the light is squeezed (called ponderomotive squeezing) through the self-phase modulation, which increases the phase noise of the measurement; also, the optical spring effects will alter the mechanical dynamics of the mirrors. Although the latter has been sufficiently studied [20, 25, 37], the former has not been observed yet on the macroscopic scale. Our result concerning the observation of quantum back-action changed the situation, and will provide the field of the GW detectors with a suitable platform to experimentally investigate a *back-action evasion* method in order to overcome the free-mass SQL.

### 3.1.2 Back-action evasion method

In order to overcome the free-mass SQL, there are primarily three types of techniques: (i) creating correlations between the shot noise and the back-action noise [29, 30]; (ii) measuring the conserved dynamical quantity of the mechanical oscillator, e.g., momentum [35, 36]; (iii) an *effective* modification of the mechanical dynamics, e.g., using the optical spring effect created by the detuning of a signal recycling (SR) cavity in the GW detectors (unlike our case, it creates *frequency-dependent* rigidity called ponderomotive rigidity) [32, 33, 34]; and a variety of other techniques [13, 95]. Although these QND techniques have been theoretically developed, almost all of them have not been implemented in the quantum regime because the preparation of a platform, whose sensitivity must be limited by the quantum back-action, is very difficult.

Here, we introduce the first technique of creating correlations between the shot noise and the RPSN for the QND measurement, because our setup will be suitable to investigate this technique. It includes: (i-i) modifying the input optics called input (frequency-dependent) squeezing; (i-ii) modifying the output optics, called (frequency-dependent) homodyne measurement. This technique evades the quantum back-action and achieves a sensitivity limited only by the shot noise.

- **Input-squeezing**

Since both the shot noise and the RPSN can be attributed to the same vacuum fluctuation entering the detector from the unused port, injecting a squeezed vacuum into this port can improve the sensitivity of the interferometer. In practice, this technique was experimentally implemented so as to reduce the shot noise using the phase-squeezed vacuum [31]. For overcoming the free-mass SQL, however, the required squeezed vacuum is very different, because a nearly phase-squeezed vacuum is required for higher frequencies, at which the shot noise dominates. However, a nearly amplitude-squeezed vacuum is required for lower frequencies, at which the radiation pressure noise dominates. To meet the demand, the squeezing angle should have an appropriate frequency-dependence, thereby creating the correlation between the shot noise and the RPSN (i.e., it includes not only back-action evasion, but also reduces the readout noise). Frequency-dependent squeezing can be created using the optical cavity, which was demonstrated at around 10 MHz [96]. At around the more suitable frequency for GW detectors, it

is being prepared at MIT [97]. However, there is no platform to test the input frequency-dependent squeezing for the QND measurement. We can prepare the platform in the near future (See Chapter 7).

- **Utilization of ponderomotive squeezing**

Unlike input-squeezing, ponderomotive squeezing has a superb feature, i.e., it does not need an external squeezed vacuum generator (squeezer), such as an OPO (optical parametric oscillator). However, similarly to input-squeezing, the *frequency-dependence* is ideally necessary not for the squeezer, but for the readout of the optical signal. In the conventional interferometer, shown in Fig. 3.1, the displacement signal is measured in the phase quadrature, and then the anti-squeezing limits the sensitivity. To utilize the correlation created by the ponderomotive squeezing, the output signal should be appropriately read out in a frequency-dependent quadrature, because the ponderomotive squeezing also has a frequency dependence. This is because the quantum radiation pressure fluctuation in Eq. (2.63) has no frequency dependence inside the cavity linewidth; however, the mechanical susceptibility in Eq. (2.36) has a dependence above the resonant frequency. Although the frequency-dependent readout can also be realized by using the optical cavity, it is not always necessary for the QND measurement, unlike in the case of input-squeezing. This is because the correlation already exists without the frequency-dependent readout, due to ponderomotive squeezing. Therefore, this back-action technique is more achievable than the others.

## 3.2 Test of quantum mechanics

Although quantum mechanics has proven to be highly successful in explaining physics below the microscopic scale, its validity at the macroscopic scale is still being debated. Recent advances in technology have gradually enabled experimental tests of quantum mechanics at scales close to the macroscopic scale of our everyday life [13, 98, 99]. However, the superposition of positions of macroscopic objects beyond the Planck mass has not been observed, even though quantum mechanics predicts it. This is at the heart of the so-called “quantum measurement problem”. Until now, intense theoretical and experimental studies have revealed that the environment, such as a thermal bath,

plays an important role in the decoherence – the loss of quantum interference [100, 101, 102, 103]. Under the many-world interpretation [104], this decoherence effect will make us understand the problem without any inconsistency [105]. From a positivistic point of view, however, it is not a fundamental solution, because linear quantum mechanics cannot destroy superposition.

Turning now to general relativity, gravity might prohibit the superposition of massive objects (i.e., gravity field) due to its non-linearity. In addition, there are several intriguing facts that: (i) the consistency between the scale of the Planck mass ( $\sim 22$  ug) and the scale where the micro-to-macro transition takes place; (ii) the absence of a theory of quantum gravity; and (iii) the conflict between the general covariance and the unitary time evolution of quantum physics [106, 107]. Remarkable proposals were put forwarded by Diósi [106] and Penrose [107] based on the incompatibility of general relativity and the unitary time evolution of quantum physics. According to their models, dimensional analysis suggests that the quantum superpositions vanish within a timescale of  $\tau = \hbar/\Delta E$ , where  $\Delta E$  is the spread of the mutual gravitational energy among components of the quantum superposition or the self-energy of the mass-distribution-difference, respectively.

To test the effect of gravity, the utilization of optomechanical oscillators combined with light, such as a levitated micro-sphere (e.g., satellite mission MAQRO [108]) and suspended mirrors (e.g., gravitational-wave detectors such as LIGO [44, 59]) have been proposed. The former system enables us to test the effect of gravity, because the cooled micro sphere behaves like an electron in the *double slit* experiment. The latter system enables us to test the effect of gravity, because the mirror is expected to be entangled with the laser field, and the resulting entanglement causes the position of the oscillator to be superposed. [42, 44]. If we prepare a massive object sufficiently isolated from the environment so that the superposition state is expected to be prepared from the viewpoint of the quantum mechanics, we can test the gravity-collapse model. Especially the suspended mirror attracts considerable attention, since the massive mirror, which enhances the effect of gravity, can enable us to precisely test the effect of gravity [109, 110, 111].

For the entanglement states between separated oscillators created by ra-

diation pressure, these give [109]

$$\tau_{\text{D}} \sim \frac{\sqrt{\hbar\Omega_{\text{q}}}L^2}{Gm^{3/2}}, \quad (3.1)$$

$$\tau_{\text{P}} \sim \frac{\Omega_{\text{q}}}{G\rho}, \quad (3.2)$$

where  $\tau_{\text{D}}$  is the timescale for the Diósi's model,  $\tau_{\text{P}}$  is the timescale for the Penrose's model,  $L$  is the distance between two oscillators,  $G$  is the gravitational constant,  $\rho$  is the density of the oscillator,  $m$  is the mass of the oscillator, and  $\Omega_{\text{q}}$  is the characteristic frequency introduced in the next subsection. In Ref. [109],  $\tau_{\text{D}} = 1 \times 10^{-5}$  s,  $\tau_{\text{P}} = 4.3 \times 10^9$  s, which were obtained for GW detectors. In our case shown in Fig. 7.2, we estimate  $\tau_{\text{D}}$  and  $\tau_{\text{P}}$  to be  $1.8 \times 10^{-5}$  s and  $4.4 \times 10^{10}$  s, respectively [ $L = 1$  cm,  $\Omega_{\text{q}}/2\pi = 4.5 \times 10^3$  Hz and  $m = 5$  mg]. Therefore, our table-top system can have a comparable life-time to that of the GW detectors, and it might be possible to test the Diósi's model similarly to GW detectors [110]. To distinguish these models (furthermore, there are many other models [105, 108]), it should be tested for various macroscopic mass scales.

In an optomechanical system, the quantum back-action represents a quantum fluctuation (vacuum fluctuation) of the light derived from the Heisenberg uncertainty principle (HUP). Therefore, the observation of quantum back-action identifies the connection between the oscillator and the quantumness of light, and thus it is a necessary condition for generating an entangled state. In the following subsection, we describe the stronger necessary condition.

### 3.2.1 The requirement

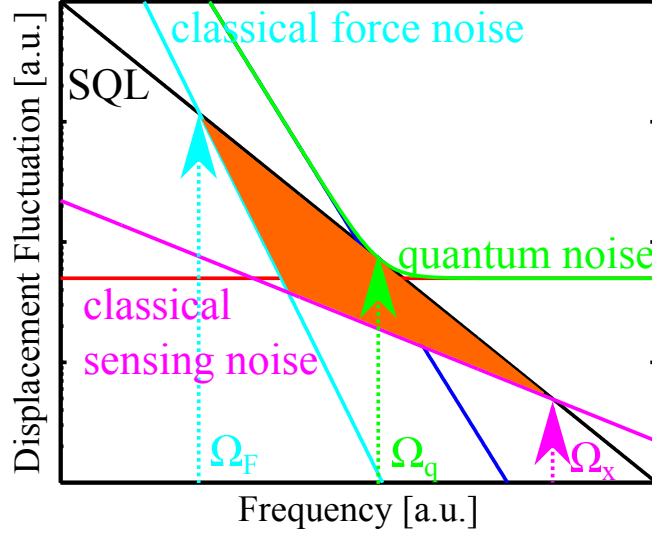


Figure 3.2: **The sub-SQL window:**  $\Omega_F$ ,  $\Omega_q$ , and  $\Omega_x$  are the frequencies at which the classical force noise (e.g., the suspension thermal noise), the quantum back-action, and the classical sensing noise (e.g., the mirror thermal noise) intersect the free-mass SQL, respectively. The quantum back-action (blue), shot noise (red), sum of the quantum back-action and the shot noise (green), classical force noise (cyan), classical sensing noise (magenta) and free-mass SQL (black) are shown. In order to generate the entanglement states, a sub-SQL accuracy, with an error area smaller than the free-mass SQL, is essential [109]. The orange-colored area represents the sub-SQL window.

In order to test the quantum mechanics, entanglement states involving massive objects have the key, like in the case of GW detectors [44]. Here, we only pay attention to the cavity-assisted entanglement states, similarly to GW detectors [112]. In this case, the generation requires, in terms of the force measurement, that the sensitivity should be limited by the free-mass SQL, shot noise, and quantum back-action. The area under the free-mass SQL, which is reachable through the QND technique, is called the sub-SQL window, shown in Fig. 3.2. We have to realize a low  $\Omega_F$  and a high  $\Omega_x$ ,

which represent an inverse time of thermalization and a characteristic frequency for the sensing noise, respectively. For  $\Omega_x/\Omega_F > 2$ , there is a nonzero frequency band (in between  $\Omega_F$  and  $\Omega_x$ ) in which the classical noise is completely below the free-mass SQL. Therefore, our next goal is to prepare a cavity that satisfies this condition (Chapter 7). In Ref. [44, 109, 112], the *logarithmic negativity* [113], which characterizes the degree of entanglement of the quantum state, is also calculated as a function of  $\Omega_x/\Omega_F$ .

# CHAPTER 4

## Optical Torsional Spring

---

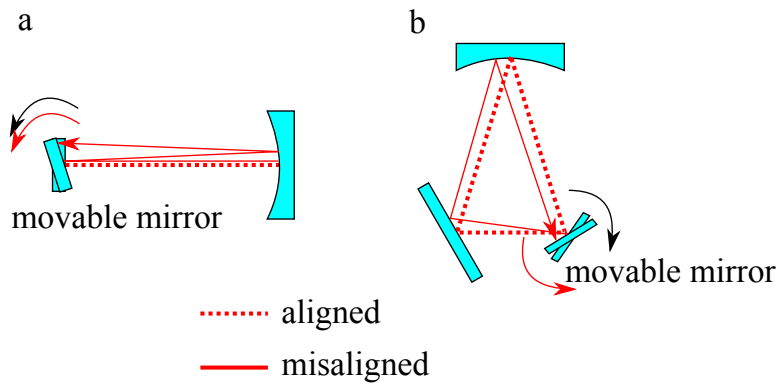


Figure 4.1: **Schematic of optical torsional effects.** The schematic responses of the optical axes to the angular motion of the movable mirror are shown. The detailed response for the triangular cavity is given in Ref. [114]. An optical torque occurs through the stationary radiation pressure. **a:** In the case of the linear optical cavity, the optical torque occurs in the same direction as the angular motion. This results in an anti-restoring force. **b:** In the case of the triangular optical cavity, the optical torque occurs in the opposite direction as the angular motion. This results in a restoring force.

The *positive* torsional spring effect is the key effect in our experiment because it enables us to use both the large gravitational dilution effect (See Chapters 5 & 6) and the powerful double optical spring effect (See Chapters 5 & 6). This effect was independently discovered by Daniel Sigg [115] and myself. Unlike a linear cavity, light experiences *odd* numbers of reflections on mirrors inside a triangular cavity. This results in a *positive* torsional spring effect. Figure. 4.1 enables us to intuitively and visually understand the difference

between the linear and triangular optical cavities. Although one can calculate the optical positive torsional effect using the result described in Ref. [114], we use the result described in Ref. [115] for simplicity. Also, we describe an experimental demonstration of the effect.

## 4.1 Model of a triangular cavity

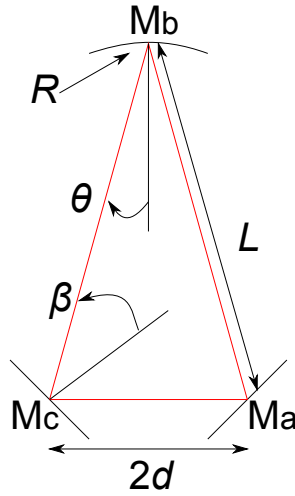


Figure 4.2: **Schematic of the triangular cavity.** This figure represents the layout of the triangular cavity. The triangular cavity formed by two flat mirrors, labeled  $M_a$  and  $M_c$  (the movable mirror), and a curved mirror, labeled  $M_b$ .  $L$ , represents the distance between the curved mirror and the flat mirror;  $d$  is half the distance between the two flat mirrors,  $R$  is the radius of curvature of mirror  $M_b$ ,  $\theta$  is the incident angle on the curved mirror, and  $\beta$  is the incident angle on the flat mirror.

Here, we derive the torsional spring effect around the suspension axis (yaw) due to the radiation-pressure torque in a triangular cavity. We use Sigg's result[115], and begin by considering a two-dimensional triangular cavity formed by two flat mirrors, labeled  $M_a$  and  $M_c$ , and a curved mirror, labeled  $M_b$ , as shown in Fig. 4.2. We decompose the rotations of the two flat mirrors into two basis modes: the common-mode (same the rotation direction, the same amount) and the differential-mode (opposite rotation direction, the same amount). Any misalignment state of the two mirrors can be expressed

as a linear combination of these two basis modes. In this picture, the relationship between the misalignment angle,  $\Delta\alpha$ , of the basis modes and the change in beam position on each of the mirror,  $\Delta x$ , is given by [115]

$$\Delta x = LK_h\Delta\alpha \quad (4.1)$$

with

$$K_h = \frac{1}{L(d+L-R)} \begin{pmatrix} \frac{-2d(L-R)}{\cos\beta} & 0 & \frac{-\sqrt{2}dR}{\cos\beta} \\ 0 & \frac{-2L(d+L-R)}{\cos\beta} & 0 \\ -\sqrt{2}dR & 0 & (d+L)R \end{pmatrix}. \quad (4.2)$$

Here,  $L$  is the distance between the curved mirror and the flat mirror,  $d$  is half the distance between the two flat mirrors,  $R$  is the radius of curvature of mirror  $M_b$ , and  $\beta$  is the incident angle on the flat mirror. The torque,  $N_{\text{rad}}$ , on each mirror induced by the radiation pressure is given by

$$N_{\text{rad}} = \frac{2P_{\text{circ}}}{c} LTK_h \quad (4.3)$$

with

$$T = \begin{pmatrix} \cos\beta & 0 & 0 \\ 0 & \cos\beta & 0 \\ 0 & 0 & \cos\theta \end{pmatrix}, \quad (4.4)$$

where  $c$  is the speed of light in a vacuum,  $P_{\text{circ}}$  is the circulating power in the triangular cavity,  $\theta$  is the incident angle on the curved mirror, and  $\beta$  is the incident angle on the flat mirror. When the acute-angled isosceles triangular optical cavity with a positive g-factor is considered, the optical spring constant is always positive, because all eigenvalues of Eq. (4.3) become negative [115]. This suggests that the triangular cavity is intrinsically stable in the yaw direction.

For simplicity we consider the situation where only the mirror  $M_a$  is movable and others are fixed. In this case, the equations of motion are given by

$$I_a\ddot{\alpha}_a = -(k_{t,\text{opt}} + k_{t,\text{m}})\alpha_a, \quad (4.5)$$

$$k_{t,\text{opt}} \equiv -\frac{P_{\text{circ}}}{c} l \cos\beta (K_h(1,1) + K_h(2,2)), \quad (4.6)$$

where  $I_a$  is the moment of inertia about the wire axis of mirror  $M_a$ ,  $k_{t,\text{opt}}$  is the angular spring constant of mirror  $M_a$  induced by the radiation pressure, and  $k_{t,\text{m}}$  is the mechanical torsional spring constant of mirror  $M_a$  in yaw.

From this equation, we can derive the resonant frequency of the yaw motion as

$$f_a = \frac{1}{2\pi} \sqrt{\frac{k_{t,\text{opt}} + k_{t,\text{m}}}{I_a}}. \quad (4.7)$$

From Eqs. (4.6) and (4.7) it is found that the angular resonant frequency is increased with increased circulating power.

## 4.2 Experimental setup

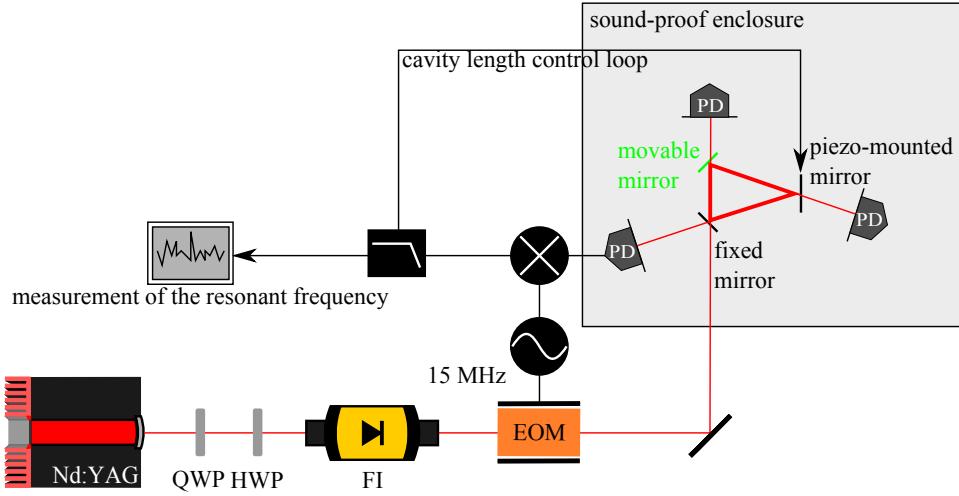


Figure 4.3: **Detailed experimental setup for observing the optical torsional spring effect.** The laser beam (red line) was fed into the triangular cavity. An electro-optic modulator (EOM) was used to apply frequency sidebands for a Pound-Drever-Hall (PDH) method. Light was detected at various points using photodetectors (PD). HWP, Half-Wave Plate; QWP, Quarter-Wave Plate; FI, Faraday Isolator.

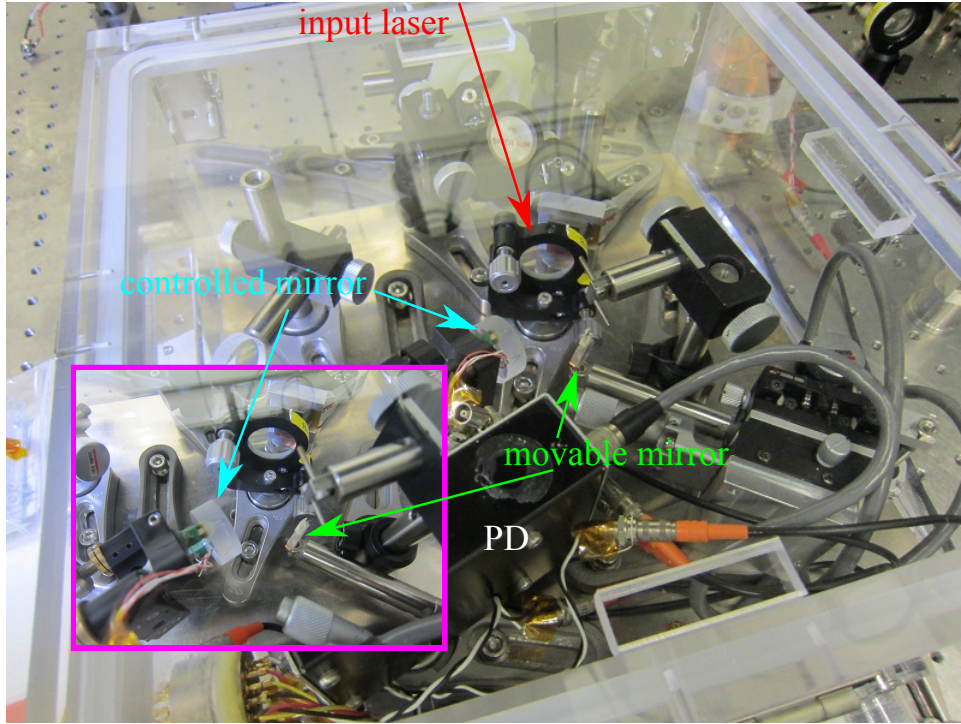


Figure 4.4: **Photograph of the experiment for observing the optical torsional spring effect.**

In order to quantitatively verify the model described in the previous section, we measured the angular resonant frequency of a mirror in a triangular cavity. By changing the internal power of the cavity, thus changing  $k_{t,opt}$ , we expect the resonant frequency to change according to Eq. (4.7).

A schematic of the experimental setup is shown in Fig. 4.3. The laser source was a monolithic non-planar Nd:YAG ring laser with a 2 W continuous-wave single-mode output power at 1064 nm. We used an electro-optic modulator (EOM) as a phase modulator at 15 MHz to lock the triangular cavity via a Pound-Drever-Hall (PDH) locking scheme. The triangular cavity with a length of 100 mm and a finesse of 223 was composed of two flat mirrors and a fixed curved mirror with a radius of curvature of 75 mm. One of the two flat mirrors was a half-inch fused silica mirror suspended by a tungsten wire of 30  $\mu\text{m}$  diameter and 100 mm length. The suspended mirror was attached to an oxygen-free copper cylinder of 3 mm diameter and 3 mm thickness, which was damped by an eddy-current using a doughnut-shaped magnet. Because

of its shape, the magnet damps only the pendulum motion without decreasing the mechanical quality factor of the yaw motion. The curved mirror was fixed, and was mounted on a piezoelectric transducer (PZT), which was used as an actuator to keep the cavity in resonance with the laser. The triangular cavity and a photodetector were placed in a vacuum desiccator for acoustic shielding.

The reflected light was received by a photodetector, and its output signal was demodulated at the modulation frequency. This signal was then low-pass filtered with a cutoff frequency of 1 Hz, and fed back to the PZT actuator. The unity gain frequency of the length control servo was approximately 1 kHz. We used this signal to stabilize the cavity length and also to measure the angular (yaw) resonant frequency. The yaw motion of the suspended mirror generated the PDH signal, because there was a slight miscentering of the beam position on the suspended mirror. The transmitted light was also detected in order to measure the intracavity power. The incident light power into the cavity was varied from 60 mW to 1 W in order to measure the change in the angular resonant frequency.

### 4.3 Experimental results & Discussions

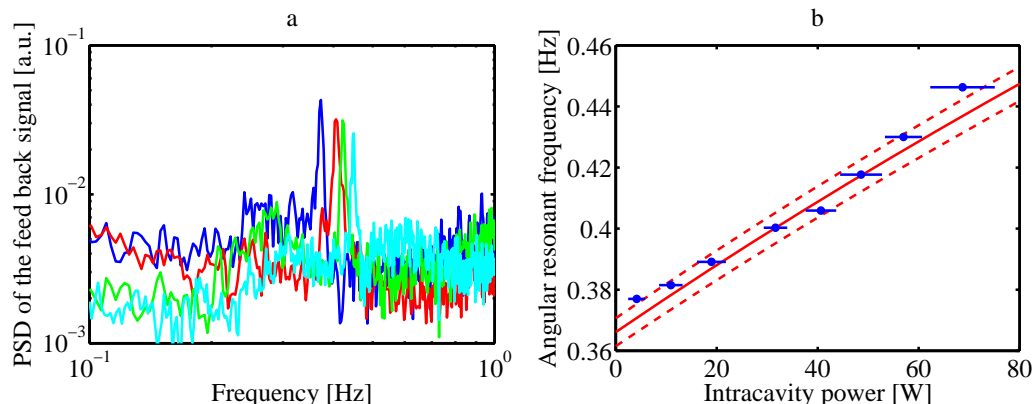


Figure 4.5: **Optical torsional spring response for various power levels.** **a:** Observed spectra of the feedback signal. The peaks correspond to the yaw resonance of the suspended mirror with the intracavity power (4 W(blue), 32 W(red), 46 W(green) and 68 W(cyan)). **b:** Angular resonant frequency of the mirror suspension against the intracavity power. The blue circles are the measurement data and the blue horizontal lines are the statistical errors. The solid red curve is the theoretical prediction obtained from Eqs. (4.6) and (4.7) and the dashed red curve shows the systematic error.

Figure 4.5a shows the observed spectra of the feedback signal with the intracavity power at 4 W, 32 W, 46 W, and 68 W. The peaks at around 0.4 Hz are the yaw resonances. The angular resonant frequency increases with increasing circulating power. The measured angular resonant frequencies are plotted against the intracavity power in Fig. 4.5b. The blue circles are the measured values and the horizontal lines are the statistical errors. The dashed red curves are the theoretical predictions, obtained from Eqs. (4.6) and (4.7) with  $l = 44$  mm,  $d = 10$  mm,  $\beta = 0.67$  rad,  $k_{t,\text{opt}} = 1.0 \times 10^{-9} \times P_{\text{circ}}$  Nm/rad,  $I_a = 2.4 \times 10^{-8}$  kgm<sup>2</sup>, and  $k_{t,m} = 1.3 \times 10^{-7}$  Nm/rad. The theoretically calculated values show good agreement with the experimental results, which suggests that Eq.(4.6) is suitable for modeling the torsional spring effect caused by the optical restoring force.

Until now, we have only paid attention to the yaw. Note that this is a sufficient discussion in order to consider the stability of our triangular cavity. Because the suspended mirror can easily have sufficient mechanical positive

torsional spring constants for a pitch without increasing the suspension thermal noise, even though the anti-torsional spring effect occurs for the pitch. This is due to the fact that the stiffness of the pitch does not depend on the radius of the wire, which mainly determines the dilution factor, but depends on the radius of the mirror.

From this result and the following consideration, the advantage of the triangular cavity can be understood. When the linear cavity is used, the instability can be mitigated by, e.g., (i) reducing the optical power; (ii) shortening the cavity length; (iii) using a thick wire for suspension; (iv) using multiple wires for suspension; (v) active control; and (vi) using a linear optical cavity that consists of fixed and suspended mirrors under the *negative-g* condition (i.e., both focal points are inside the cavity; in other words, both mirrors have a concaved structure). However, those induce: (i) a reduction of the quantum back-action; (ii) no issue; however, in practice it is insufficient only by it; (iii) a reduction of the gravitational dilution (i.e., increasing the suspension thermal noise); (iv) introducing an unexpected thermal noise through the unexpected normal mode generated by the complicated suspension system [116]; (v) the necessity of using a more macroscopic mirror to be attached along with the actuator, which would result in decreasing the quantum back-action (i.e., relatively increase all technical noise), and also might introduce some other dissipation through the actuator [to avoid these issues, using the lossless control system via radiation pressure without attached actuators has been proposed [117]]; and (vi) the necessary of using a sufficiently concaved and small mirror in order to make the cavity length shorten (as a supplemental explanation, the linear optical cavity demands the condition given by  $0 \leq (1 - L/R_1)(1 - L/R_2) \leq 1$ , where  $L$  is the cavity length,  $R_1$  is the curvature of the one mirror and  $R_2$  is the curvature of the other mirror) and avoid the same issue of (v). (If an appropriate mirror can be manufactured, this method has no issue. We have been trying, but it is still challenging.) On the other hand, the triangular cavity has an *intrinsic* stability for yaw motion. As a result, one can conclude that the triangular cavity overcomes the fundamental compromise between the sensitivity and the instability for the linear cavity.

# CHAPTER 5

## Experimental Setup

---

Figure 5.1 shows the displacement noise induced by the quantum back-action that sets our goal of sensitivity. At the resonant frequency of the pendulum (130 Hz), the displacement noise is approximately  $1 \times 10^{-12}$  m/ $\sqrt{\text{Hz}}$ . Every component was specially designed to achieve the sensitivity needed to detect the quantum back-action. In this chapter, we describe an experimental setup for a direct measurement of the quantum back-action.

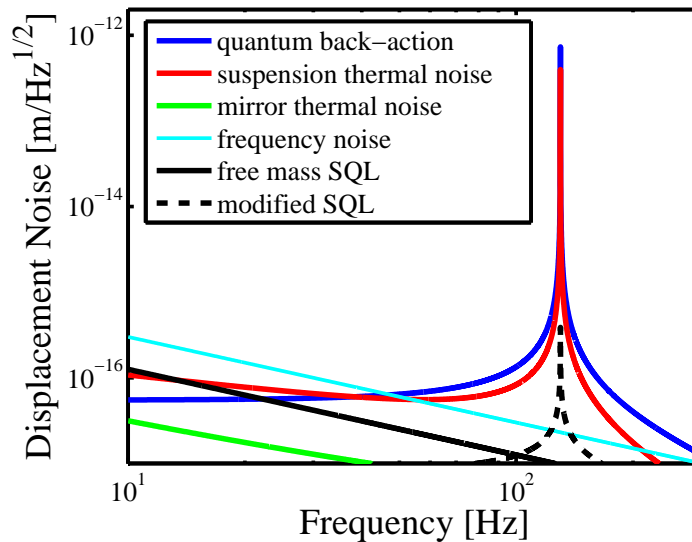


Figure 5.1: **Goal sensitivity for observing the quantum back-action.** The quantum back-action (blue), the suspension thermal noise (red), the mirror thermal noise (green), the laser frequency noise (cyan), the SQL for the free mass (dotted black) and the SQL for the modified mirror (black line) are shown.

## 5.1 All aspects of the experiment

In this section, we describe all aspects of the experiment: both the experimental setup and the technical features.

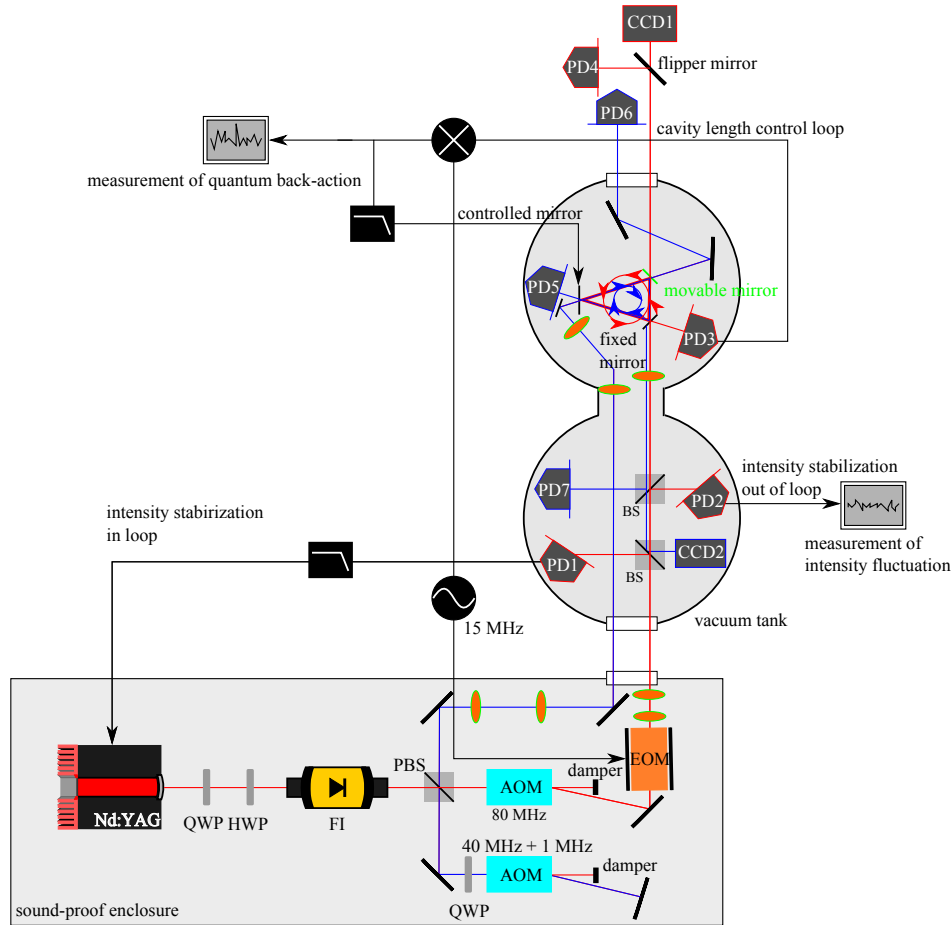


Figure 5.2: **Detailed experimental setup for observing the quantum back-action.** The driving beam (red line) and the spring beam (blue line) were fed into the triangular cavity in the same spatial mode, but in different directions. Acousto-optic modulators (AOM) were used to shift the laser frequency. An electro-optic modulator (EOM) was used to apply frequency sidebands for the PDH method. Light was detected at various points using photodetectors (PD). HWP, Half-Wave Plate; QWP, Quarter-Wave Plate; FI, Faraday Isolator.

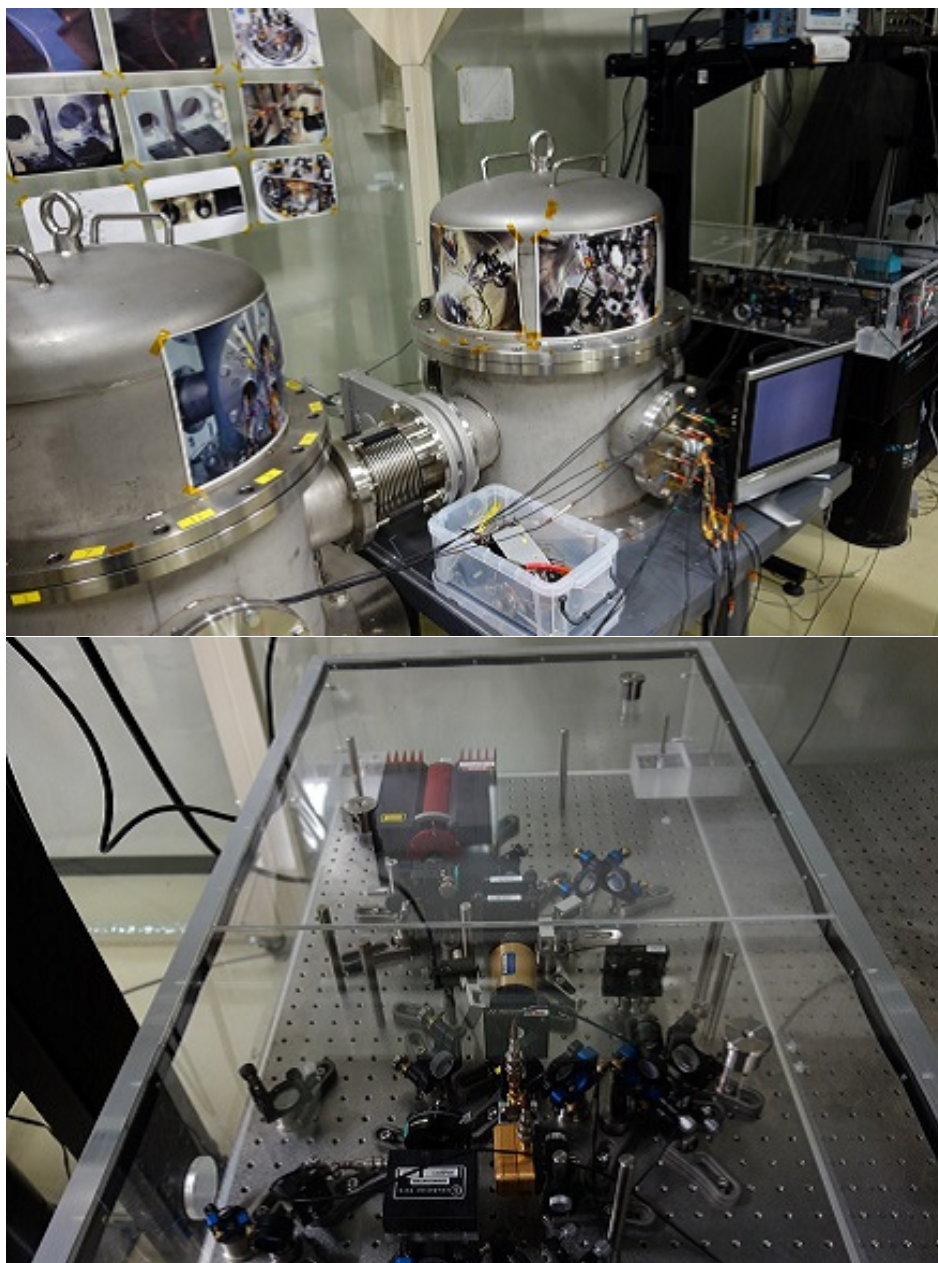


Figure 5.3: Photographs of the experiment for observing the quantum back-action.

**Experimental Setup** The detailed experimental setup is shown in Fig. 5.2. Our optical cavity had a triangular configuration constructed from one movable mirror (mass, 5 mg; shown in Fig. 5.4), one half-inch fixed mirror, and one half-inch suspended mirror with a coil-magnet actuator attached onto its aluminum mirror holder for cavity length control (mass, 97 g; radius of curvature, 200 mm) (Figs. 2.5 a and 5.2). The 5-mg mirror was suspended by a tungsten wire of 50 mm length with 3  $\mu\text{m}$  diameter, attached to the mirror with epoxy resin. On the top of the wire, a picomotor-actuated stage for yaw alignment was attached. The fixed mirror and the controlled mirror had picomotors for both pitch and yaw alignment. Also, there were two picomotor-actuated folding mirrors for aligning each incident beam. These adjustment mechanisms allowed us to align the optics inside the vacuum chamber remotely. The triangular cavity, which was suspended by a double pendulum on a double-stage pre-isolation stack, was installed in a vacuum chamber ( $10^{-3}$  Pa) in order to sufficiently reduce any seismic motion, acoustic vibration, gas damping and so on.

The shape of the optical path of the cavity was an isosceles triangle, which had round-trip length of  $L = 90$  mm. The incident angle to the movable mirror was  $\beta = 0.64$  rad. The finesse of the cavity was  $1.10 \times 10^3$ , and each mirror had a (power) transmittance of  $T_{\text{in}1} = 4.8 \times 10^{-3}$ ,  $T_{\text{in}2} \simeq 1 \times 10^{-4}$ , and  $T_{\text{in}3} < 8 \times 10^{-4}$ . In other words, the half linewidth of the cavity is  $\kappa/2\pi = 1.5$  MHz and the optomechanical coupling constant is  $g/2\pi = 2.8\omega_c$  Hz/m, where  $\omega_c$  is the cavity resonant frequency.

The Nd:YAG laser source at the operational wavelength of 1064 nm was used, and the whole input optics system was covered by a sound-proof acryl box so as to reduce any jitter of the input beams. Two beams split from the same laser source were injected to the cavity in the same spatial mode, but in opposite directions. One of the two beams was injected from the fixed mirror in a clockwise direction (spring beam, illustrated as the blue line in Figs. 2.5 and 5.2), and the other one was injected from the controlled mirror in a counterclockwise direction (driving beam, illustrated as the red line in Figs. 2.5 and 5.2). The frequency of the driving beam was slightly red-detuned ( $\Delta_a/\kappa \simeq -0.05$ ), and the frequency of the other was largely blue-detuned ( $\Delta_b/\kappa = +1.3$ ) from the cavity resonance (Figs. 2.5 b, c). The incident beam powers were  $P_{\text{in}1} = 5$  mW and  $P_{\text{in}2} = 0.1$  W, and the intra-cavity power values were  $P_{\text{in}1,\text{circ}} = 2.9$  W and  $P_{\text{in}2,\text{circ}} = 0.5$  W, respectively. Since the driving beam has a larger intra-cavity power and a smaller detuning, this beam was the major source of the quantum back-action.

The driving beam was frequency shifted by 80 MHz with an AOM and phase modulated in 15 MHz with an EOM. A portion of the driving beam was picked-off and detected by a photodetector with a high quantum efficiency (Perkin Elmer, C30632, InGaAs photodiode). In order to stabilize the intensity of the laser beam sufficiently, we have to take into account the vacuum fluctuation,  $\delta\hat{a}_1$  and  $\delta\hat{a}_2$ , inevitably injected from the open ports of BS1 and B2, respectively. Because the vacuum fluctuation,  $\delta\hat{a}_1$ , has an anti-correlation between an in-loop (PD1) and an out-of-loop (PD2), a correlation between the laser intensity fluctuation and the vacuum  $\delta\hat{a}_1$  will be generated in the out-of-loop after stabilization (See Appendix). This results in increasing the noise level in out-of-loop, which is so-called “noise penalty” [118]. In addition, a possible minimum relative to the shot noise level in out-of-loop is also limited by the uncorrelated vacuum,  $\delta\hat{a}_2$ . More concretely, in our case, the required relative shot-noise levels of the input beams were smaller than 2.0 dB and 26 dB for the driving and spring beams, respectively, based on Eqs. (2.63) and (2.64). Thus, the power injected to the photodetector (PD1; in-loop) used for the intensity stabilization was two-times larger than the power injected to the photodetector (PD2; out-of-loop) for monitoring the intensity fluctuation. This power balance allows intensity stabilization of the beam at a relative shot-noise level of 1.8 dB. Besides, there were picomotors-actuated mirrors before these two PDs so as to adjust the position of the beam spot on the detectors in order to find the spot position where the effect of the beam jitter is minimized. Moreover, the incident angles to these two PDs were adjusted to the Brewster angle in order to minimize the effect of the back scattering.

A sufficiently stabilized beam was injected into the cavity, and the cavity reflected beam was detected with the fast-responding PD (PD3; HAMAMATSU, G10899-01K, InGaAs photodiode). The output of this PD was demodulated with a 15 MHz RF signal to obtain the cavity length signal. We used this signal for cavity length control, and also to extract a quantum back-action signal. One of the transmitted beams from the cavity was monitored by CCD1 or PD4 (flipped by a flipped mirror), and the other one was eventually rejected at the Faraday isolator.

The frequency of the spring beam was shifted by 82 MHz with an AOM in the double pass configuration, before injecting into the cavity. The cavity-reflected beam was monitored with PD5. One of the transmitted beams was monitored by PD6, and the other one was monitored by PD7 and CCD2.

**Technical Features** There are three main technical features in our experiment: an extremely thin suspension wire, the triangular geometry of the cavity and the use of double optical spring. The thin wire assures that the amount of energy stored in the pendulum is dominated by the gravitational potential over the elastic bending energy of the wire [85]. Since any loss of the energy is only associated with the elastic part of the stored energy, the total mechanical loss of the pendulum is diluted with gravity by a factor of  $k_{\text{grav}}/k_{\text{el}} = 4l\sqrt{mg/\pi Y}/r^2 = 1 \times 10^3$ , where  $k_{\text{grav}}$  and  $k_{\text{el}}$  are the gravitational and elastic spring constants of the pendulum,  $r$  is the radius of the wire,  $l$  is the length of the wire,  $m$  is the mass of the mirror,  $Y$  is the Young's module of the wire, and  $g$  is the gravitational acceleration. Any reduction of the loss results in a reduction of a thermal fluctuation force, which also drives the mechanical motion similarly to the quantum back-action, by a factor of  $\sqrt{k_{\text{grav}}/k_{\text{el}}}$ .

The radiation pressure of the light induces a torque on the mirror when it is rotated. In a suspended linear cavity, this torque works as an optical anti-torsional spring, which causes a mechanical instability (so-called Sidles-Sigg instability [24, 25]). This is especially a serious issue because the mirror is suspended by the thin wire in order to reduce the thermal noise, which provides a small mechanical torsional spring constant ( $k_{\text{t,m}} \simeq 3 \times 10^{-11}$  Nm/rad) to compete against the optical anti-torsional spring. In order to circumvent this limitation, we used a triangular cavity, which has a positive optical torsional spring, and exhibits no instability in the rotation around the suspension axis. In our setup, the optical torsional spring constant is  $k_{\text{t,opt}} = +1 \times 10^{-9}$  Nm/rad, whereas it is  $k_{\text{t,opt}}^{(\text{linear})} \simeq -3 \times 10^{-9}$  Nm/rad for a linear cavity with otherwise the same parameters. As a result, we can store a about 100-times higher optical power in our cavity than the instability limit for the linear cavity. Besides, compared with mechanical springs, the optical torsional spring is free from the thermal noise penalty because the optical field is almost in its ground state.

The third feature is the double optical-spring technique [20], which used to increase the resonant frequency of the pendulum without increasing the thermal noise, similarly to the optical torsional spring. By detuning a cavity from its resonance, one can create an optical-spring effect for the position of a mirror. However, the optical-spring (anti-spring) effect is always accompanied by optical anti-damping (damping), and thus it is unstable by itself. Since our pendulum has a low mechanical decay rate ( $\gamma_{\text{m}}/2\pi = 2.3 \times 10^{-6}$  Hz)

due to the large dilution, the anti-damping effect cannot be compensated by the mechanical damping. In order to avoid this problem, we used the combination of two optical springs, by injecting two laser beams, in order to cancel out the instability (Fig. 2.5c). With this technique, we can increase the resonant frequency of the pendulum to 130 Hz, where the technical noises, such as ground vibration and laser frequency noise, are smaller.

In conclusion, the geometrical advantages of the triangular cavity enables for the mirror to be isolated from the thermal bath under high intracavity power, thus allowing us to use the powerful double optical spring, which also enables isolation from any technical noise sources. As a consequence, we were able to observe the quantum back-action imposed on a mg scale object, which is far beyond the Plank mass, at room temperature (See Chapter 6).

## 5.2 Partial aspects of the experiment

In this section, we discuss a mechanical oscillator (i.e., a suspended mirror consisting of a mirror and a tungsten wire), which is fluctuated by quantum back-action, and a vibration isolation system for it.

### 5.2.1 Mechanical oscillator

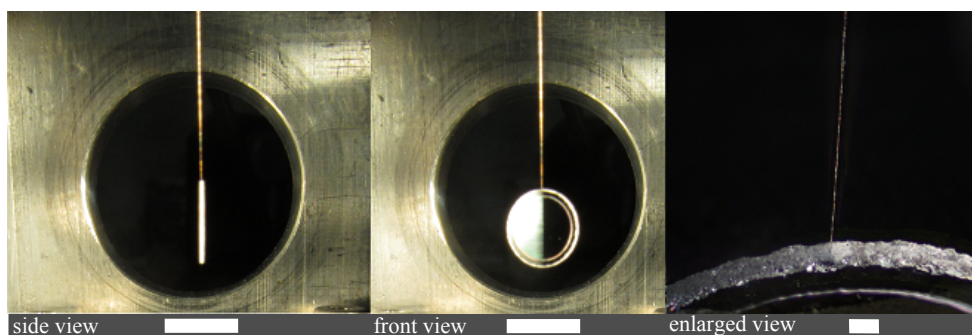


Figure 5.4: **Mechanical oscillator.** The mirror was manufactured by SIGMA KOKI. It has a radius of 2 mm, a thickness of 0.2 mm, and a mass of 5 mg. A tungsten wire of 3  $\mu\text{m}$  diameter and 50 mm length was attached to the mirror with epoxy resin. In both side and front views, it appears to be much larger than the real size of the tungsten wire because of an overexposure of the camera. The enlarged view photographed by a stereoscopic microscope (Olympus, SZ61) shows the interface between the wire and the mirror. Scale bars, 4 mm in both side and front views, and 0.2 mm in an enlarged view.

- **Details of the mechanical oscillator**

The mechanical oscillator is one of the key components in our experiment because it mainly determines the magnitude of the quantum back-action in terms of both the mechanical susceptibility and the optical power gain inside the cavity. In addition to the signal level, it also determines the noise level of a suspension thermal noise through material dissipation and gravitational dilution (shown in Fig. 5.1). It is the main noise source driving the mechanical oscillator, similarly to the quantum back-action. To reduce the difficulty for detection, the mechanical oscillator was designed to have a low mass (5.0 mg), a high

(power) reflectivity (the designed values are 0.99957 for p-polarized light and 0.99997 for s-polarized light), and a low mechanical loss of the pendulum (the estimated value is  $Q_m = 4.7 \times 10^4$ ; see Chapter 6). The low mass was achieved using a thin (the radius was 0.2 mm) flat mirror. [Furthermore, the flat mirror reduces the noise, which is leaked from the residual side-motion (i.e., orthogonal to the pendulum).] Unlike a conventional *linear* optical cavity, the geometrical advantages of a *triangular* cavity enables us to stably trap the flat mirror due to the optical torsional spring effect. (In general, the dissipation of substrate material, which is related to the mirror thermal noise, increases as the object becomes thin due to only surface loss. Therefore, we estimate that its mechanical quality factor of the substrate is  $10^5$ . This is relatively lower, but is sufficient to observe the quantum back-action, partially because of an enhancement of the quantum back-action through the lightening.) The low mechanical loss of the pendulum was achieved by using an ultra-thin wire (the radius was 1.5  $\mu\text{m}$ ) to suspend the mirror, and high reflectivity was achieved using Ion Beam Sputtering (IBS) to coat it.

- **Dimensions and spot size**

The dimensions of the triangular cavity and the spot size on the movable mirror are important factors in terms of a frequency noise of the laser and any mirror thermal noise, respectively. By designing the path length and the spot size to be as small as possible, these sensing noises are depressed. We set the cavity round-trip length as short as possible, 9 cm, from the viewpoint of easy handling. The beam radii on the movable mirror and on the controlled mirror, as determined by the cavity parameters, are 110  $\mu\text{m}$  and 178  $\mu\text{m}$ , respectively. Based on the choices of the cavity length, the substrates of the thin mirror and of the beam spot sizes, the theoretical frequency and thermal noise levels are shown in Fig.5.1.

- **Vibration isolation system**

Seismic noise is the most serious problem in the low-frequency region (i.e., the vibration level is usually about  $10^{-7}/f^2$  m/ $\sqrt{\text{Hz}}$  above 1 Hz) because it is not only increased, but also becomes difficult to be mitigated using passive filter, such as a pendulum. To avoid this difficulty, we used the double optical spring technique to enhance the resonant

frequency of the pendulum from 2.20 Hz up to 130 Hz. The double optical spring also mitigates other requirements for technical noises, such as the frequency noise and an other degrees of freedom of the seismic motion. The other seismic motions, such as a bobbing motion of the pendulum, leaks into the direction of the beam axis through asymmetries of the isolation system. Therefore, a sufficient level of attenuations for all degrees of freedom has to be achieved as well. To meet this criteria, the isolation system was made of two parts: a double pendulum and a double stack.

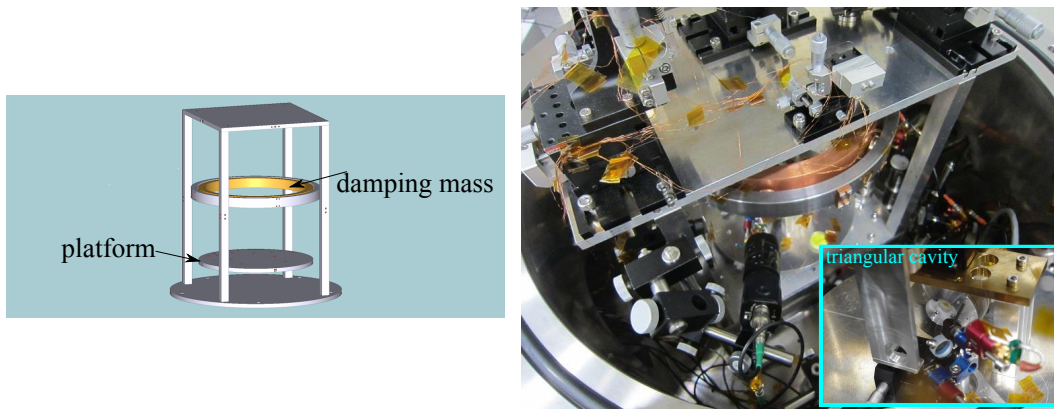


Figure 5.5: **Double-pendulum system.**

Figure 5.5 shows the suspension system designed for this experiment. The triangular cavity was placed on a platform made of aluminum, which was suspended by the double pendulum on a double stage pre-isolation stack. Common-mode rejection of seismic noise is expected by using the common platform for the triangular cavity. The intermediate ring mass (made of copper) of the double pendulum was also suspended with three tungsten wires (radius of 150  $\mu\text{m}$ ) and vertical coil springs. For the purpose of damping, another larger intermediate ring mass (made of steel) with strong magnets was suspended next to the (smaller) intermediate mass of copper. In order to avoid any re-injection of seismic noise from the damping magnet, the intermediate mass of steel was also isolated from any seismic motion. In order to decouple the seismic motion from other degrees of freedom, the slope of the platform of aluminum was adjusted using x-y-z stages, which were attached onto stages located on the top of the double pendulum.

Then, the slope of the intermediate mass of steel was also adjusted by using the other x-y-z stages, which were attached on stages in order to decouple the eddy-current damping from other degrees of freedom. The double-pendulum system theoretically provides 160 dB of isolation at the resonant frequency of the movable mirror in the horizontal plane. In the vertical plane, the coil springs provide 80 dB of isolation at the resonance.

The pre-isolation stack, designed and constructed by Kenji Numata [119], can provide further isolation for all degrees of freedoms, although the double pendulum ensures sufficient isolation. The stack was composed of two stainless-steel blocks, separated by isolation rubbers. The isolation performance of this stack was also measured by Numata using a vibration exciter. It was better than 70 dB for the vertical direction, and 80 dB for horizontal direction at resonance [119].

The total performance of this suspension and the stack system is estimated by multiplying the simulated isolation ratio of the suspension and the measured isolation ratio of the stack to 150 dB and 240 dB. The required level of displacement noise was very likely achieved.

### 5.2.2 Intensity stabilized laser

One of the main noise sources for the quantum back-action measurement is the classical back-action force generated by the classical intensity noise of the laser. By making a high finesse cavity (i.e., high optical power gain inside the cavity), we can decrease the power of the input driving beam to 5 mW, such that the requirement of the classical intensity noise level is reduced in terms of the relative *intensity* noise level. Note that the requirement of the noise level in terms of the relative *shot*-noise level is unchanged. Intensity stabilization is performed based on an active feedback control.

In this section, the intensity stabilized laser, composed of the laser source, the photodetector, and the stabilization servo system will be explained.

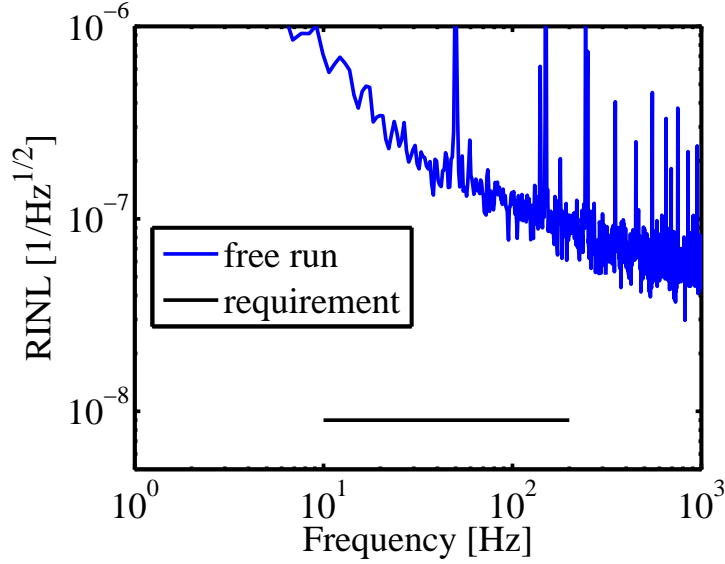


Figure 5.6: **Requirement for intensity stability.** The observed spectra of intensity fluctuation without stabilization. The black line represents the requirement for achieving the shot-noise level inside the cavity.

- **Requirement for the intensity stability**

Figure 5.6 shows the free-run intensity noise of the laser that we used. Our goal sensitivities converted into a relative intensity noise level is shown. To reduce the requirement of the relative *intensity* noise level, the input driving beam (main source of quantum back-action) power was suppressed to 5 mW (i.e., simply put, the requirement of the relative intensity noise level is about  $9 \times 10^{-9} 1/\sqrt{\text{Hz}}$ ).

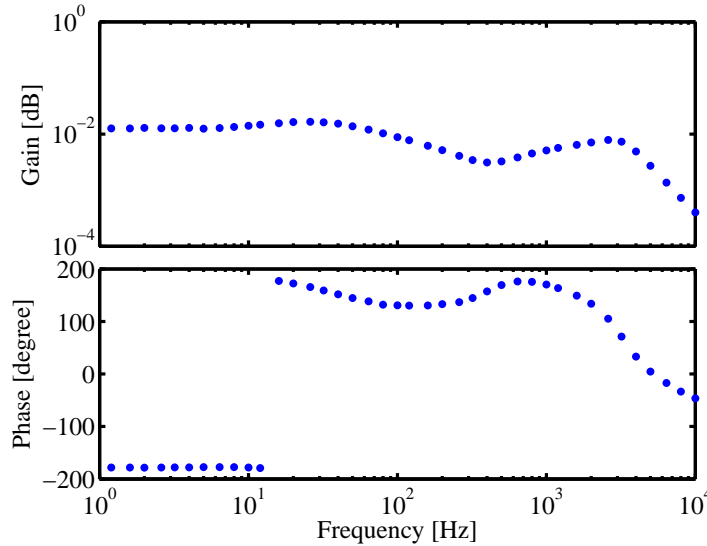


Figure 5.7: **Transfer function from the intensity modulation of the laser to the PD1.**

- **Laser source**

As a laser source we used a monolithic non-planar Nd:YAG ring laser with 2 W continuous wave single-mode output power at 1064 nm. The wavelength is the most common choice in the current GW detectors. Nonplanar ring oscillators (NPROs) are monolithic lasers where the laser radiation circulates along a nonplanar ring in a single laser crystal. This is believed to give the best performance as a continuous-wave laser. The laser intensity can be modulated by applying a voltage signal to its current actuator. Our intensity stabilization was done by using this actuator. The tuning efficiency was measured before its installation into the injection bench of our setup. Figure 5.7 shows the initially measured transfer function, from the applied voltage on the tuning current to the laser-intensity-change, as a function of the control signal frequency.

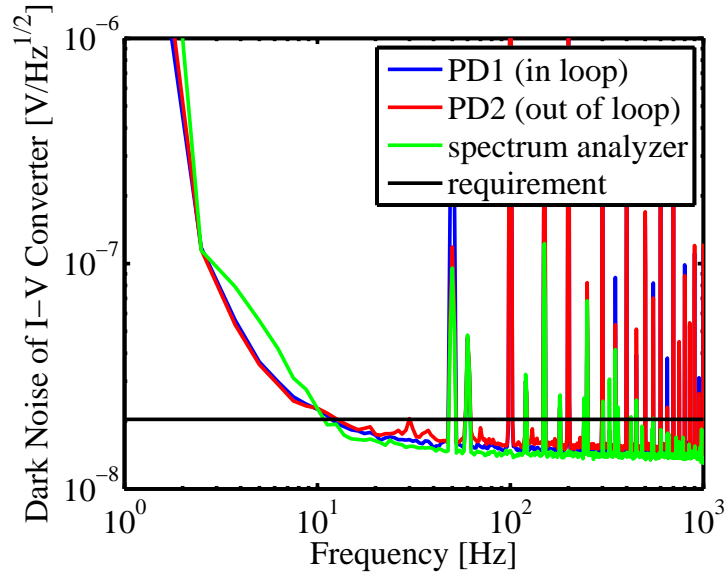


Figure 5.8: **Dark noise of photodetectors.** Observed spectra of the voltage fluctuation of the photodetectors. Both detectors satisfy the requirement (black).

- **Photodetectors for intensity stabilization**

The two beam-splitter output fields were focused onto Perkin Elmer C30642 InGaAs photodiodes with an active diameter of 2 mm. The electronics was designed by referring to that specified in Ref. [120]. Since intensity stabilization is performed by measuring the intensity fluctuation, the dark noise of the detectors has to be under the required intensity noise level. To confirm this, we measured the dark noise as shown in Fig 5.8.

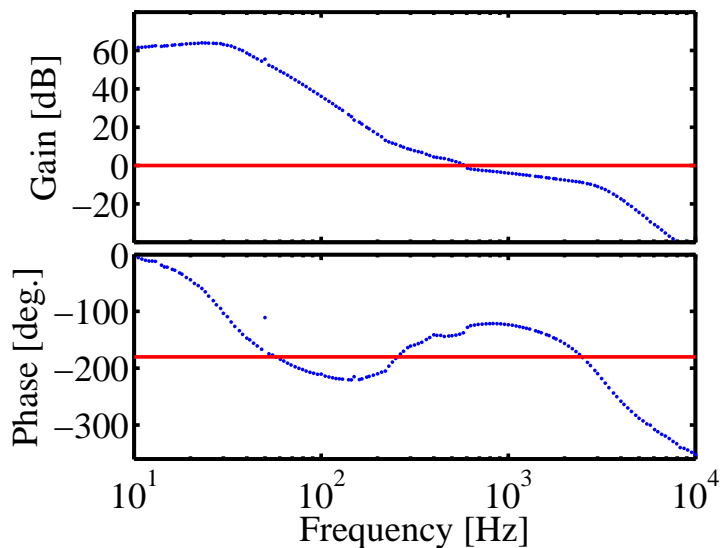


Figure 5.9: **Open-loop transfer function of the intensity stabilization.** The unity-gain frequency was approximately at 600 Hz.

- **Servo system**

We designed the servo system to have a sufficiently high gain to achieve the goal sensitivity. The control signal is fed back to a current actuator of the laser head. Figure 5.9 shows the measured openloop transfer function of the stabilization loop. The unity gain frequency was about 600 Hz, and phase margin was 55 deg. The stabilization gain was 28 dB at 130 Hz, which is larger than the required gain (about 20 dB).

### Achieved stability

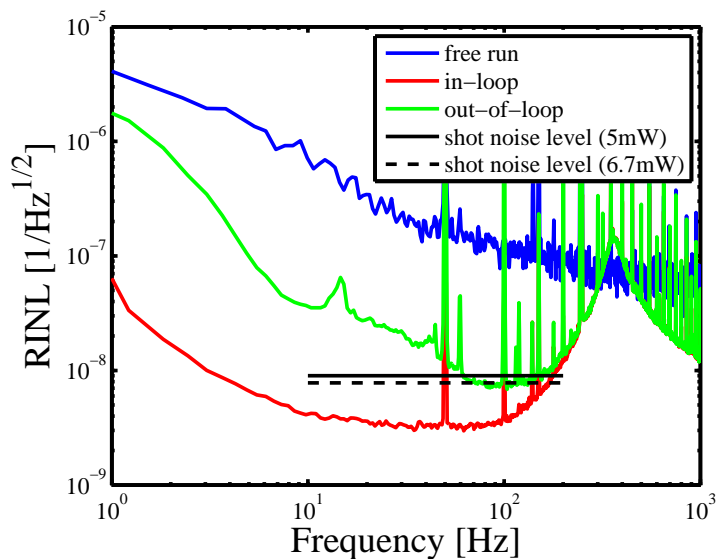


Figure 5.10: **Measured intensity fluctuation.** Observed spectra of intensity fluctuation of the input driving beam. The measured intensity fluctuation (blue), measured intensity fluctuation before the stabilization (red), and the requirement for achieving the shot-noise level inside the cavity (green) are shown.

Figure 5.10 shows the measured intensity noise. The actual stability of the stabilized laser was measured by the error signal of the non-stabilization loop (out of loop). According to the measurement, the stability satisfies our requirement near the resonance.

### 5.2.3 Actuator efficiency

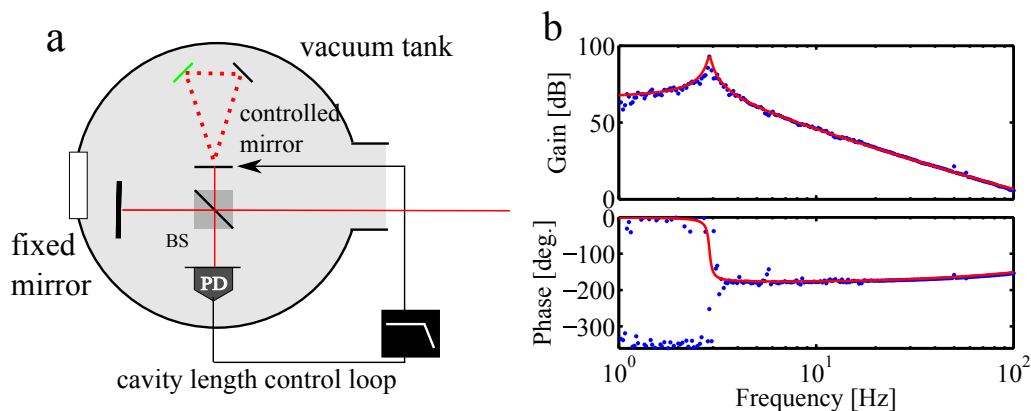


Figure 5.11: **Measurement of the efficiency of the coil-magnet actuator.** **a:** Experimental setup. The laser beam was fed into the Michelson interferometer (MI). Light was detected using a photodetector (PD), and the MI was locked at the mid-fringe point. **b:** Measured open loop transfer functions of the displacement control are shown as blue points, while the red solid lines are the fitting curves. From this measurement, the actuation efficiency,  $(1.4 \pm 0.1) \times 10^{-6}$  N/V, was estimated.

In order to calibrate the displacement noise spectrum from the voltage signal, we firstly measured the actuator efficiency and determined the voltage-to-force conversion factor. Here, we present an estimation of the factor using a Michelson interferometer.

Fig.5.11 a shows the configuration used to measure the actuation efficiencies. We locked the Michelson interferometer using a PD, an appropriate servo circuit and the same coil-magnet actuator as the main measurement for observing the quantum back-action. From this measurement, we could estimate the voltage-to-force conversion factor of the actuator because the others composing the loop, such as the response of MI, the pendulum, PD, and servo filter, had been measured by other experiments. As a result, we experimentally determined the actuation efficiency  $(1.4 \pm 0.1) \times 10^{-6}$  N/V.

Secondly, we determined the force-to-voltage conversion factor from Eq. (6.5). As a result, the voltage-to-displacement conversion factor at  $\omega \ll \omega_m$  was estimated  $(8.5 \pm 0.6) \times 10^{-11}$  m/V.

### 5.2.4 Detection system, control system and vacuum system

In this section, we will describe the signal detection system, control system for the triangular cavity and the vacuum system. The signal detection system is composed of a modulator, a RF photo detector, and a demodulator.

- **Modulator**

We used the Pound-Drever-Hall technique to control the triangular cavity. The laser beam was phase modulated by an EOM (New Focus Inc., model 4003) on the injection bench. The EOM is made up of a LiNbO<sub>3</sub> crystal and a tank circuit tuned at 15 MHz. The EOM is driven by a commercial oscillator at 15.000 MHz. We set the output voltage of the oscillator at 1 V, and the modulation depth was about 0.1 rad.

- **RF photo detector and demodulator**

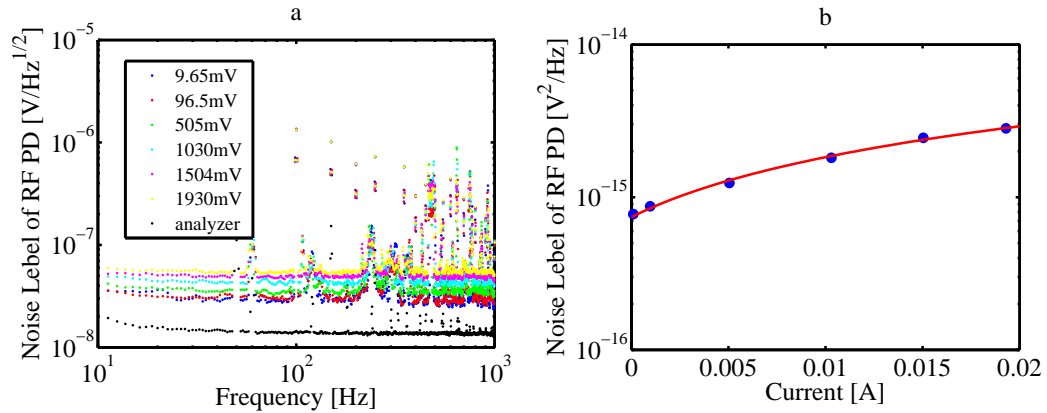


Figure 5.12: **Characterization of the RF PD.** **a:** Observed spectra for various input laser power. **b:** PD3 output noise at the modulation frequency.

The PDH error signal is extracted at PD3 (HAMAMATSU, G10899-01K), which detects the intensity changes at the modulation frequency in the reflected light. The PD3 is followed by an RLC circuit that converts its photocurrent to voltage with high efficiency, and preamplifiers. The  $Q$  of the circuit was measured to be 30. The detected RF

signal is demodulated and down-converted to an AF signal by a Double Balanced Mixer (DBM; Mini Circuit, SBL-1).

The output voltage noise from the demodulator,  $V_n$ , represents the sum of the shot noise and of the detector noise in general [119]. The equivalent photo current noise,  $I_{\text{det}}$ , is defined by

$$V_n^2 = 2eR_{\text{det}}^2(I_{\text{DC}} + I_{\text{det}}). \quad (5.1)$$

Here,  $R_{\text{det}}$  is the equivalent resistance for the current-to-voltage conversion, and  $I_{\text{DC}}$  is the DC photocurrent. To make the noise of the detection system negligible compared to the shot noise,  $I_{\text{det}}$  has to be smaller than  $I_{\text{DC}}$ . In our case, the shot noise is not a serious problem because the input laser power was increased such that the radiation pressure shot noise dominates. On the other hand, an equivalent resistance is necessary to check the consistency of a calibration. Figure 5.12 shows the measured demodulated output voltage of PD3 as a function of the DC photocurrent. The response was fitted by Eq. 5.1. The noise equivalent photocurrents,  $I_{\text{det}}$ , were estimated to be 6.8 mA. The equivalent resistance was estimated to be 583  $\Omega$ . Typical photocurrents operations occurs at 4 mA, which is slightly less than the noise equivalent photocurrents; however, the photodetector and demodulation system does not limit the sensitivity.

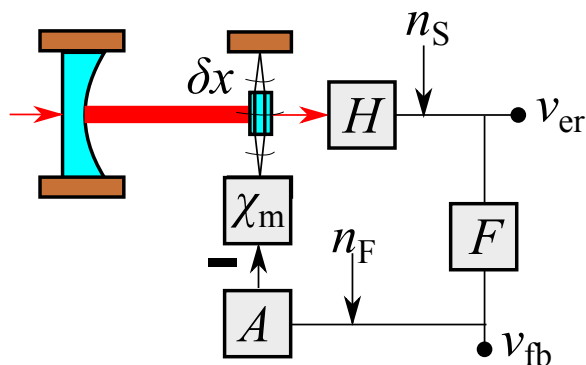


Figure 5.13: **Block diagram of the triangular cavity servo.**  $\delta x$ , displacement of the movable mirror;  $H$ , displacement-to-voltage conversion factor;  $F$ , servo filter;  $A$ , the efficiency of the actuator;  $\chi_m$ , mechanical susceptibility;  $v_{er}$ , error signal;  $v_{fb}$ , feedback signal;  $n_s$ , sensor noise;  $n_f$ , filter noise. In practice, the PDH signal was extracted by the reflected light and the actuator was attached not to the movable mirror, but the controlled mirror (See Chapter 6).

- **Servo system for the cavity length control**

The detected signal at the PD3 was demodulated by the DBM, and then sent to a control servo circuit. The displacement fluctuation can be extracted from error/feedback signals (labeled  $v_{er}$  and  $v_{fb}$ , respectively) of the servo loop. In the following, we describe the open-loop transfer function of the triangular cavity loop.

Figure 5.13 shows a diagram of the triangular cavity servo system. The displacement of the movable mirror,  $\delta x$ , is converted by the PDH method into a voltage through a displacement-to-voltage conversion factor,  $H$  [V/m] (consists of the transfer function of the optical cavity and the RF photodetector), producing an error signal,  $V_{er}$  [V]. It is filtered by an electric servo circuit,  $F$  [V/V], producing a feedback signal,  $V_{fb}$  [V]. The feedback signal pushes the movable mirror  $\chi_m$  [m/N] through the coil with an efficiency of  $A$  [N/V]. Here, an open-loop transfer function of the triangular cavity loop,  $G = HFA\chi_m$ , is obtained. From the error signal, the displacement can be estimated as

$$\delta^{(er)}x = \frac{1+G}{H}v_{er} \xrightarrow{G \rightarrow 0} \frac{1}{H}v_{er} = \delta x + \frac{n_s}{H} + A\chi_m n_f. \quad (5.2)$$

On the other hand, based on the feedback signal, it is given by

$$\begin{aligned}\delta^{(\text{fb})}x &= \frac{1+G}{FH}v_{\text{fb}} = \delta x + \frac{n_S}{H} + \frac{A\chi_m}{G}n_F \\ \xrightarrow{G \rightarrow \infty} A\chi_m v_{\text{fb}} &= \delta x + \frac{n_S}{H}.\end{aligned}\quad (5.3)$$

Based on the viewpoint of the filter noise, the estimation from the feedback signal is appropriate; however, it can not *directly* measure the resonant motion. If one can not measure the mechanical susceptibility from any other measurement, the estimation from the error signal is appropriate for the resonant motion. In our case, the imaginary part of the mechanical susceptibility was not measured by any other measurement (See Chapter 6, Figs. 6.3, 6.5). Therefore, we estimated it from the error signal. In order to reduce the feedback gain at the resonance, we used a notch filter, described below.

- **Notch filter**

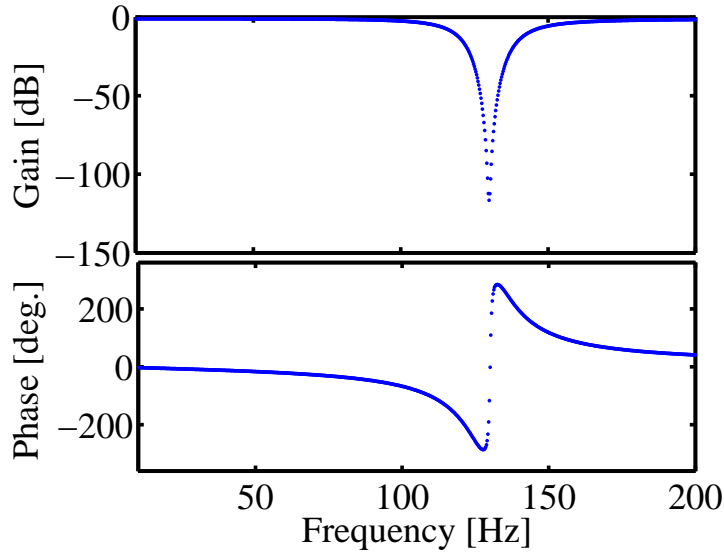


Figure 5.14: **Characterization of notch filter.** Measured transfer function of the notch filter.

In order to *directly* measure the resonant motion of the pendulum, the feedback gain has to be reduced at the resonance under 0 dB. To meet the demand, we used the notch filter. The effective quality factor of our pendulum was estimated to be about 4300, and thereby the notch should have more than a 70 dB attenuation and less than a quality factor of 4300. According to the measurement, the demand was satisfied.

### **Vacuum system**

Every component of the system, except for the input optics on the injection bench, was housed in a vacuum system in order to reduce the effect of sound, air motion, changes in the refraction index along the optical path, and so on. Figures 5.3 and 5.5 (right) show the vacuum system used in this experiment. Two almost identical vacuum tanks were used for the intensity stabilization and for the observation of quantum back-action. The system is relatively compact - their inner diameter is about 50 cm. Every component was designed to fit inside. The system was evacuated with a rotary pump and a turbomolecular pump connected to the tank in which the intensity stabilization signal was extracted. The typical vacuum level was a  $10^{-3}$  Pa.

# CHAPTER 6

## Experimental Results

In this chapter, we describe the experimental results of direct measurements of the quantum back-action imposed on the 5-mg mirror. In order to show the validity of our measurement, we also show the characterization of the optical, mechanical, and optomechanical systems. These measurements give us the information about the intracavity power, cavity linewidth, suspension thermal noise, effective mechanical susceptibility, quantum back-action, and so on.

## 6.1 Optical characterization

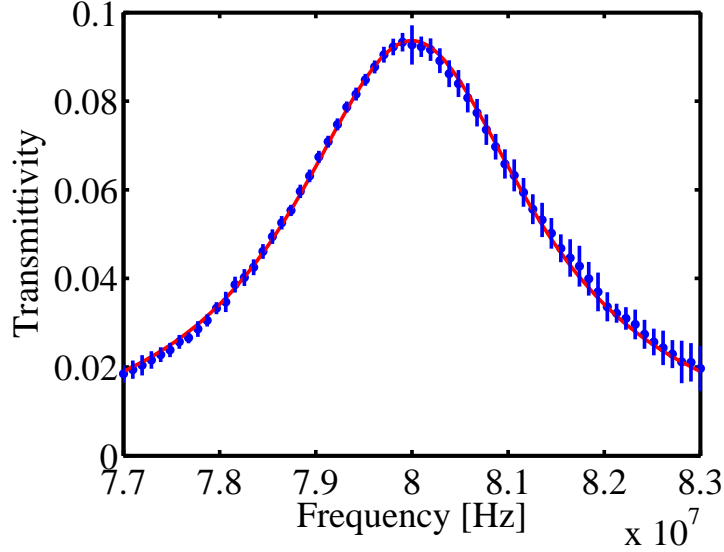


Figure 6.1: **Cavity scan.** The optical characterization of our devices was done by sweeping the laser frequency across the optical resonance while detecting the transmitted light in a photo-detector. The blue circles are measured values and the vertical blue lines are the statistical errors; the red line is the fitting line. From this measurement, the total decay rate,  $\kappa/2\pi = (1.52 \pm 0.03) \times 10^6$  Hz (i.e. finesse,  $\mathcal{F}_p = (1.10 \pm 0.02) \times 10^3$ ), was estimated against the p-polarized light. We also estimated it against s-polarized light, which resulted in  $\mathcal{F}_s = (3.86 \pm 0.09) \times 10^3$ . Here, we used the p-polarized light because the priority was given to the easiness of cavity control.

From Eq. (2.63), the optical parameters  $\kappa$ ,  $\kappa_{\text{in}1}$ , and  $\kappa_{\text{in}2}$  are necessary for estimating the power spectrum of the quantum back-action. Here, we provide estimations of these parameters.

The experimental setup for making the estimations is shown in Fig. 5.2. We measured the transmittance of the triangular cavity using the spring beam (blue line in Fig. 5.2), which was not used to control the cavity length. The shifted frequency of the spring beam was changed within the range from 77 MHz to 83 MHz by AOM, while the driving (control) beam was shifted at

80 MHz. Thus the transmittance of the cavity for the broadband frequency could be measured using PD6 and PD7. Figure 6.1 shows the result. From this measurement, the total cavity decay rate,  $\kappa$ , and the combination of  $\kappa_{\text{in}2}(\kappa_{\text{in}1} + \kappa_{\text{in}3} + \kappa_{\text{in}4})$  could be estimated. In addition to this information, the ratio of the decay rate of the fixed mirror to that of the controlled one (indexed in1 and in2, respectively), which was measured from the ratio of the tuned-transmittance of the driving beam to one of the spring beams, was used to separate them. As a result,  $\kappa/2\pi = (1.52 \pm 0.03) \times 10^6$  Hz (i.e. finesse,  $\mathcal{F}_p = (1.10 \pm 0.02) \times 10^3$ ),  $\kappa_{\text{in}1}/2\pi = 1.3 \times 10^6$  Hz, and  $\kappa_{\text{in}2}/2\pi \simeq 3.2 \times 10^4$  Hz were estimated.

## 6.2 Mechanical characterization

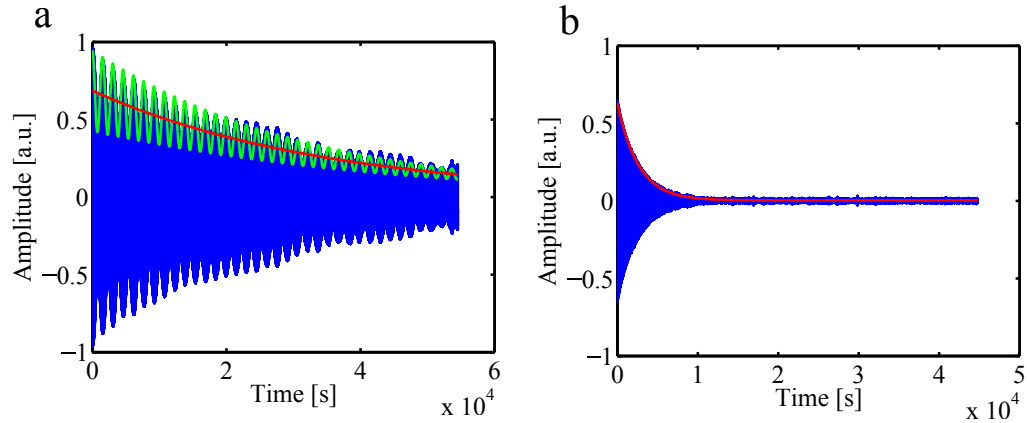


Figure 6.2: **Ringdown measurement.** The measured damped oscillations for the pendulum and the yawing motion are shown, respectively. The blue solid curve is the measured value and the red lines are the fitting curve to the pendulum and the yawing motions, respectively. The green line represents an unknown amplitude modulation of about  $600 \mu\text{Hz}$ , which might be from the temperature change of the vacuum chamber or a difference between the resonant frequency of the pendulum and that of the side-motion. **a:** Decay of the pendulum motion. The mechanical Q-value of the pendulum,  $Q_{\text{pend}} = 4.7 \times 10^5$ , was estimated. **b:** Decay of the yaw mode. The mechanical Q-value of the yaw,  $Q_{\text{yaw}} = 3.8 \times 10^3$ , was estimated.

Here we present the details of the Q-value measurement of the mechanical oscillator. The mechanical Q-value can be written as  $Q_m = \omega_m/2\gamma_m$ , using  $\omega_m$  and  $\gamma_m$  in Eq. (2.42). Also, from the fluctuation-dissipation theorem, the thermal noise can be written as

$$S_{\text{FF,th}}^{(2)} = 4k_{\text{B}}T\gamma_m m. \quad (6.1)$$

Thus, by measuring the Q-value of the pendulum, the thermal noise level can be estimated. Here,  $T$  is the temperature of the pendulum and  $k_{\text{B}}$  is the Boltzmann constant. From Eq. (6.1), it follows that the thermal noise level is proportional to the pendulum loss,  $\gamma_m$ , and so the displacement sensitivity can be improved by trapping the pendulum with the gravitational potential and diluting the loss. Our oscillator was also trapped by the optical fields. This stabilizes the system without changing the thermal noise level, since the force fluctuation caused by the thermal fluctuation does not change with the optical springs. Our oscillator is effectively cooled down to

$$T_{\text{eff}} = T \frac{\omega_m Q_{\text{eff}}}{\omega_{\text{eff}} Q_m}. \quad (6.2)$$

It is worth pointing out that this effective cooling reduces the thermal noise at the resonant frequency, but it does not change the signal-to-noise ratio (SNR) with respect to the quantum back-action. This is because the reduction of the thermal noise at the resonant frequency is caused by the change in the susceptibility, not the reduction in the force fluctuation. The change in the susceptibility also reduces the quantum back-action, and therefore SNR remains the same.

In our experiment, we used a thin wire to suspend a mirror in order to dilute the mechanical loss by the gravitational potential and to increase the pendulum Q-value. Generally, a thin wire has a low material Q-value because the loss of a material comes mainly from the surface loss. Ultra-thin wires have been used for discharging test masses for inertia sensors. There is some literature that reports on measurements of the Q-value for golden thin wires; one example reports the Q-value of a 10  $\mu\text{m}$  diameter golden wire at  $Q=270$  [121]. However, the Q-value of an ultra-thin tungsten wire, as far as we know, has not yet been reported.

Our experimental setup for the Q-value measurement was almost the same as that shown in Fig. 5.2, except that the fixed mirror was removed. The incident beam was aligned such that the beam would hit the movable mirror

at its edge, and the mirror would block the portion of the beam before the beam could be detected by PD4. The amplitude of the resonant motion can be obtained by demodulating the output of PD4 with the resonant frequencies of the pendulum mode and the torsional mode because a small oscillation of the mirror creates amplitude modulation of the beam. The Q-values were measured by exciting the mirror motion and measuring the decay time of each mode.

Our pendulum had a very high Q-value, since the loss was diluted by the gravitational potential by a factor of 1000. Therefore, the pendulum mode had a very long decay time, and measuring the Q-value without excitations was difficult. In order to prevent an overestimation of the Q-value (i.e. thermal noise), we also measured the Q-value of the yaw mode, which had a shorter decay time, to have estimated the maximum Q-value of the pendulum. In addition to the shorter decay time, the yaw mode has tolerance to the mechanical loss of the clamping mechanism, such as the epoxy due to its mode function, which represents the mechanical displacement patterns associated with mechanical motion. Therefore we can estimate the Q-value of the yaw mode as being the intrinsic mechanical Q-value of the wire. As a result, the measured pendulum Q-value should be smaller than the maximum Q-value of the pendulum estimated from  $Q_{m,\max} = Q_{t,m} \times 1.0 \times 10^3$ .

The result of the ring-down measurement is shown in Fig. 6.2. The measured Q-value for the pendulum mode was  $Q_m = 4.7 \times 10^5$  (the resonant frequency was  $\omega/2\pi = 2.2$  Hz). There was an amplitude modulation at a period of approximately 30 min, which might be from the temperature change of the vacuum chamber. However, the error caused by this amplitude modulation was negligible. The measured Q-value for the torsion mode was  $Q_{t,m} = 3.8 \times 10^3$  (the resonant frequency was  $\omega_{\text{yaw}}/2\pi = 0.23$ Hz). This means that the upper limit of the Q-value for the pendulum mode would be  $Q_{m,\max} = 3.8 \times 10^6$ , which is consistent with the Q-value from the direct measurement mentioned above. From  $Q_m = 4.7 \times 10^5$ , we estimated the suspension thermal noise level as in Figs. 5.1 and 6.4 (red).

### 6.3 Optomechanical characterization

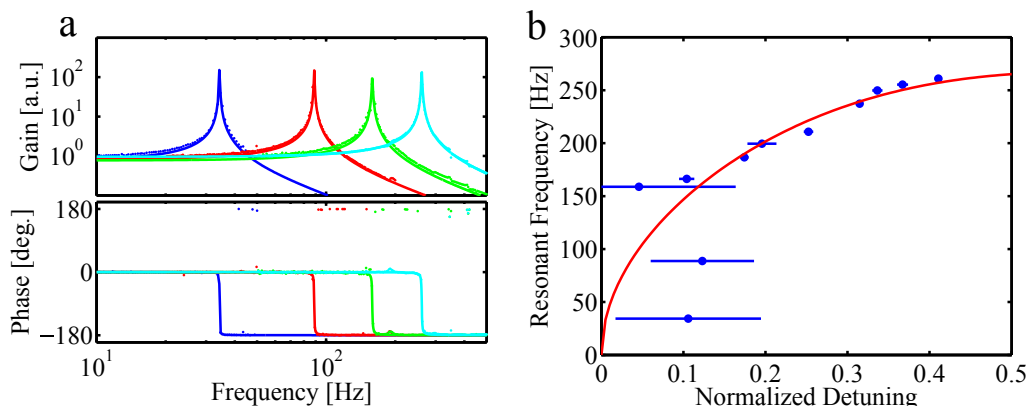


Figure 6.3: **Optical spring response for various detunings of the cavity.** **a:** Measured open-loop transfer functions of the displacement control shown as points, while the solid lines are fitting curves. **b:** Resonant frequency of the pendulum against the detuning of the cavity. The blue circles are the measurement data and the blue horizontal lines are the statistical errors. The solid red curve is the fitting curve to Eq.(2.60). From this measurement, the optomechanical coupling constant,  $g/2\pi = (2.8 \pm 0.1)\omega_c$  Hz/m, was estimated.

Here, we present the characterization of the optical spring of our optomechanical system. We measured the effect of the restoring force from the optical spring in order to estimate the optomechanical coupling constant,  $g$ , of the cavity using Eq. (2.60). Together with the measured value of  $\kappa$ ,  $\kappa_{\text{in1}}$ , and  $\kappa_{\text{in2}}$  from the optical characterization, the amplitude of the quantum back-action can be estimated.

The optical restoring force was measured using the same setup as shown in Fig. 5.2, at a higher pressure ( $1 \times 10^3$  Pa) than that for the main quantum back-action measurement. The driving beam (shown as the red line in Fig. 5.2) at 2 mW was injected to the cavity, and the cavity length was controlled using the same light (PD3). Under these conditions, the decay rate from the gas damping was  $\gamma_{\text{gas}}/2\pi \simeq +1$  Hz, and the minimum decay rate from the optical spring was  $\Gamma_{\text{opt,min}}/2m \cdot 2\pi \simeq -0.03$  Hz. Thus, the cavity stays sufficiently stable without using the double optical spring technique. After closing the cavity length control loop, a small electrical signal was injected

into the loop in order to measure the resonant frequency of the movable mirror.

Our optomechanical system can be modeled by the following coupled oscillators without the damping term:

$$M\ddot{x}_c = -(k_c + k_{\text{opt}})x_c + k_{\text{opt}}x_m + F_c, \quad (6.3)$$

$$m\ddot{x}_m = k_{\text{opt}}(x_c - x_m) - k_m x_m. \quad (6.4)$$

Here,  $k_c$  is the mechanical spring constant of the controlled mirror,  $F_c$  is the feedback force acting on the controlled mirror, and  $k_m$  is the mechanical spring constant of the movable mirror;  $x_c$  and  $x_m$  are the displacements of the controlled mirror and the movable mirror, and  $M$  and  $m$  are the masses of the controlled mirror and the movable mirror, respectively.

In our setup, the controlled mirror was heavier ( $M = 97$  g) and had a higher mechanical spring constant ( $k_c \simeq 32$  N/m). The movable mirror was lighter ( $m = 5$  mg) and had a lower mechanical spring constant ( $k_m \simeq 1 \times 10^{-3}$  N/m). The optical spring connected the controlled mirror and the movable mirror with the spring in between ( $k_{\text{opt}} \simeq 10$  N/m). Thus, the cavity length change caused by the force on the controlled mirror can be written as

$$\frac{x_c(\omega) - x_m(\omega)}{F_c(\omega)} \simeq \frac{1}{M} \frac{1}{\omega_{\text{eff}}^2 - \omega^2}, \quad (6.5)$$

in the frequency domain, where  $\omega_{\text{eff}}$  is the effective resonant frequency of the movable mirror. This means that the resonant frequency of the movable mirror can be measured by exciting the controlled mirror and measuring the cavity length change.

Figure 6.3 shows the changes in the resonant frequency of the movable mirror under different detunings of the cavity. The measured dependence of the resonant frequency to the cavity detuning was fitted by least-squares method and an estimated value of  $g/2\pi = (2.8 \pm 0.1)\omega_c$  Hz/m was obtained.

## 6.4 Direct measurement of quantum back-action

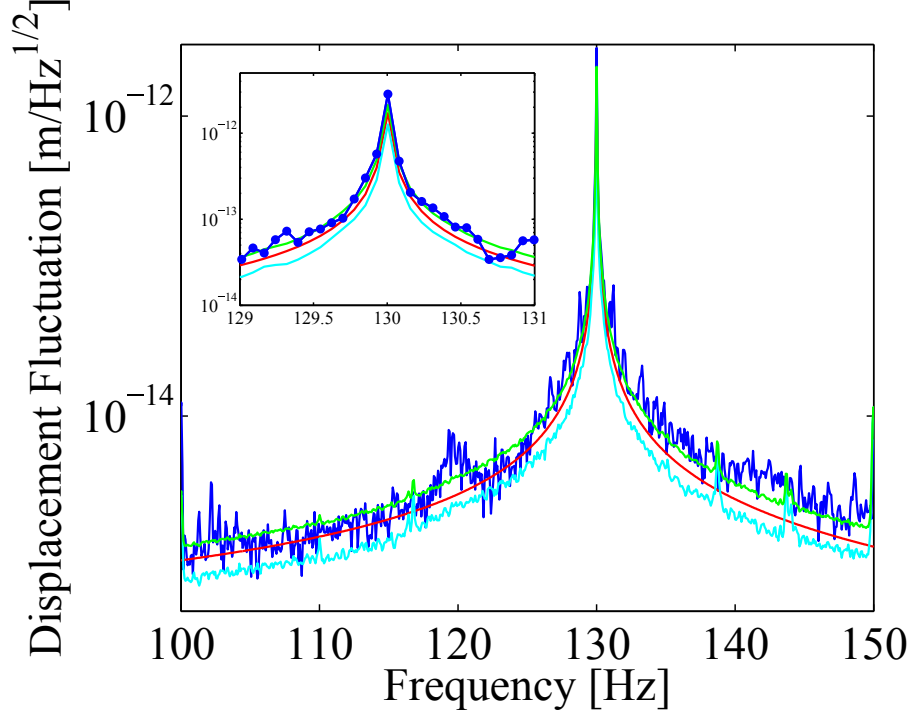


Figure 6.4: **Quantum back-action.** Observed spectra of displacement fluctuations at an optical power of  $P_{\text{circ}} = 3.4$  W; half linewidth of  $\kappa/2\pi = 1.5$  MHz; effective amplitude decay rate of  $\gamma_{\text{eff}}/2\pi = 1.53 \times 10^{-2}$  Hz; and effective resonant frequency of  $\omega_{\text{eff}}/2\pi = 130$  Hz. The measured peak displacement spectral density (blue), the estimated thermal contribution (red), the estimated back-action contribution (cyan), and the theoretical prediction (green) are shown. Then, measured peak is consistent with the theoretical estimation in Fig.2.5c, both in terms of the resonant frequency and the mechanical decay rate.

The measured amplitude power spectrum of the pendulum motion of the mirror is shown in Fig. 6.4. The result agrees well with the sum of the estimated thermal noise, the estimated classical back-action (which is generated based on the classical intensity fluctuation, not by vacuum fluctuation) and estimated the quantum back-action. Generally, the photon number fluctua-

tion of the laser is larger than the vacuum fluctuation below the MHz region. The classical back-action is also large at our measurement frequency band (100–150 Hz). In order to assure the classical back-action to be smaller than the quantum one, the intensity fluctuation of the laser should be stabilized. The required power variations of the input beams relative to the shot noise limit have to be smaller than 2.0 dB and 26 dB for the driving and spring beams, respectively. To meet this criteria, we stabilized and monitored the intensity of the driving beam with active feedback (Fig. 6.5a). We also measured the optically modified dynamics of our movable mirror just before the measurement without the notch filter. This was performed by intentionally adding a small disturbance to the cavity length control loop in order to directly confirm the resonant frequency of the pendulum (Fig. 6.5b).

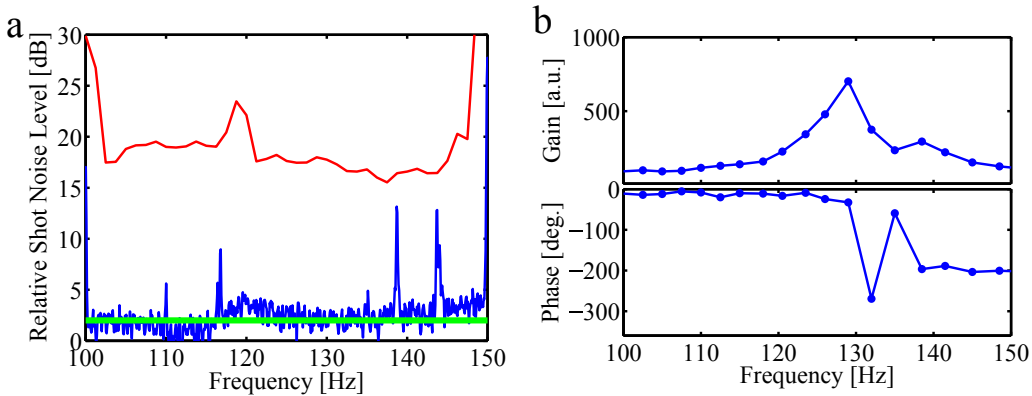


Figure 6.5: **Characterization of the light and the mechanical oscillator.** **a:** Observed spectra of intensity fluctuation of the input driving beam. Measured intensity fluctuation (blue), measured intensity fluctuation before the stabilization (red), and the requirement for achieving the shot noise level inside the cavity (green) are shown. **b:** Mechanical response of the pendulum. The measured values (blue) are given. The peak at around 130 Hz represents the pendulum resonance. The measured resonant frequency is consistent with the theoretical estimation (Fig. 2.5c). A low resolution of the measurement disables us from measuring the mechanical decay rate.

The measured resonant frequency and the mechanical decay rate of the pendulum give us precise information about the optical spring, and thus enabling us to make a consistency check on the cavity conditions (e.g. intra-cavity power, detuning) –namely, our estimate of the amount of the quantum

back-action. As a result, we estimated the ratio of the quantum back-action to the thermal noise to be  $0.33 \pm 0.03$ .

## 6.5 Discussions

Lastly of this chapter, we discuss the results. Firstly, Fig. 6.4 represents the fact that the achieved stability of the laser intensity fluctuation under the measurement was comparable to those of the requirement, although the preliminary result shown in Fig. 5.6 represents the more stable result. This is due to the difference in the measurement condition, i.e., the degree of the vacuum and laser power. The observation of the quantum back-action requires a high vacuum, such that any gas damping is sufficiently decreased ( $10^{-3}$  Pa, i.e., quality factor is  $\sim 10^6$ ). To meet this demand, the observation was performed under the operation both of the rotary and turbomolecular pumps connected to the tank, in which the intensity stabilizing signal was detected. We used relatively large 1-inch-beam-splitters (BSs) (labeled BS in Fig. 5.2) to split the signals for in-loop and the out-of loop in order to reduce the noise of the beam jitters, which are induced by the vibration of the pumps. Although the large BSs decreased the noise, there was still slight noise. This residual classical back-action noise induced by the classical noisy state could be further reduced using an interferometer, such as a Mach-Zehnder interferometer.

Secondly, Fig. 6.5b represents the fact that the measured peak shown in Fig. 6.4 was certainly the resonant motion of the pendulum. This is because of the fact that our measurement of the open-loop transfer function, in principle, reacts only to translation motion of the mirror. The slight differences between the peak frequencies shown in Figs. 6.4 and 6.5b are due to the low-resolution of the measurement concerning the open-loop transfer function. After measuring the open-loop function, the notch filter was switched on so as to reduce the feedback gain on the resonance.

Thirdly, Fig. 6.4 not only represents the displacement fluctuation, but also the effective resonant frequency and the effective quality factor of the pendulum, because we obtained it from Eq. (5.2). Especially, the information of the effective quality factor is important because we were not able to measure it from other experiments. From Eqs. (2.60) and (2.63), the validity of the measured optical spring effect implies the validity of the magnitude of the quantum back-action. Here, we emphasize that there is no inconsistency

between the measured values and the estimated values summarized in Table 6.1.

Finally, it is worth pointing out that the ratio of the displacement due to the quantum back-action force versus the thermal fluctuating force can be accurately estimated, although the displacement fluctuation due to them has relatively large errors. This is because the errors of the displacement fluctuation were mainly due to the errors of the effective susceptibility of the pendulum. The ratio, however, is not affected by the effective susceptibility. Thus, we can accurately estimate it to be  $0.33 \pm 0.03$ .

Table 6.1: parameters

parameter	symbol	unit	measured value	estimated value
input power (d)	$P_{\text{in1}}$	mW	5.0	-
input power (s)	$P_{\text{in2}}$	W	0.10	-
intracavity power (d)	$P_{\text{in1,circ}}$	W	-	$2.9 \pm 0.1$
intracavity power (s)	$P_{\text{in2,circ}}$	W	-	$0.45 \pm 0.06$
normalized detuning (d)	$\Delta_{\text{a}}/\kappa$	-	$0.048 \pm 0.005$	-
normalized detuning (s)	$\Delta_{\text{b}}/\kappa$	-	$1.30 \pm 0.07$	-
optomechanical coupling	$g/2\pi$	Hz/m	$(2.8 \pm 0.1)\omega_{\text{c}}$	(design) $2.84\omega_{\text{c}}$
cavity decay rate	$\kappa/2\pi$	Hz	$(1.52 \pm 0.03) \times 10^6$	-
finesse	$\mathcal{F}_{\text{p}}$	-	$(1.10 \pm 0.02) \times 10^3$	-
effective resonant frequency	$f_{\text{eff}}$	Hz	$130.0 \pm 0.1$	$117 \pm 22$
effective quality factor	$Q_{\text{eff}}$	-	$4 \times 10^3$	$(4.4 \pm 1.8) \times 10^3$
quality factor	$Q_{\text{m}}$	-	$4.7 \times 10^5$	$< 3.8 \times 10^6$
thermal noise level (@130 Hz)	$\sqrt{S_{\text{xx,th}}^{(2)}}$	m/ $\sqrt{\text{Hz}}$	-	$(1.9 \pm 0.7) \times 10^{-12}$
back-action level (@130 Hz)	$\sqrt{S_{\text{xx,q+cl}}^{(2)}}$	m/ $\sqrt{\text{Hz}}$	-	$(1.4 \pm 0.7) \times 10^{-12}$
actuator efficiency	$A$	N/V	$(1.4 \pm 0.1) \times 10^{-6}$	-
relative shot noise level(@130 Hz)	-	dB	$< 4.1$	-
displacement fluctuation (@130 Hz)	-	m/ $\sqrt{\text{Hz}}$	$(2.8 \pm 1.0) \times 10^{-12}$	$(2.4 \pm 1.0) \times 10^{-12}$
signal to noise ratio (@130 Hz)	-	-	-	$0.33 \pm 0.03$

# CHAPTER 7

## The Future

---

In this chapter, two possible future investigations are proposed and discussed.

First, as compared with the experiment described above, it is necessary to improve several parameters: (i) the mechanical quality factor of the pendulum; (ii) the mechanical quality factor of the substrate; and (iii) the finesse.

(i) The Q-value of the pendulum can be improved by: increasing the dilution factor by using a longer wire from 5 cm to 20 cm; changing the lossy aluminium clamp to a relative lossless steel clamp; and the degree of vacuum can be improved from  $10^{-3}$  Pa to  $10^{-4}$  Pa by changing the devices in the vacuum tank to devices with only little gas release. It is presumed that the Q-value of the pendulum can be increased from  $4.7 \times 10^5$  to  $5 \times 10^6$  at least by these improvements because the Q-value without only clamping loss was estimated to be  $3.8 \times 10^6$  in chapter 6, and further dilution enlarges the value by 4 times.

(ii) We estimated the mechanical quality factor of the substrate to be  $10^5$  by taking the thinness of the mirror into consideration. However, it was an underestimation because the mirror thermal noise was not observed. Therefore, it turned out that the value is larger than  $4 \times 10^5$ . Although it may be a slight overestimation, we estimate the Q-value of the substrate to be  $10^6$  here. If this is an overestimate, it may be necessary to change the lossy thin form of the mirror.

(iii) In this thesis, we used p-polarized light because it enabled us to easily control the optical cavity. Here, we assume that by using s-polarized light and an input coupler for the driving beam (labeled in1) better reflectivity is possible. By making these changes, the finesse would rise to 10000.

Under these assumptions, we propose the following.

## 7.1 Towards ground-state cooling

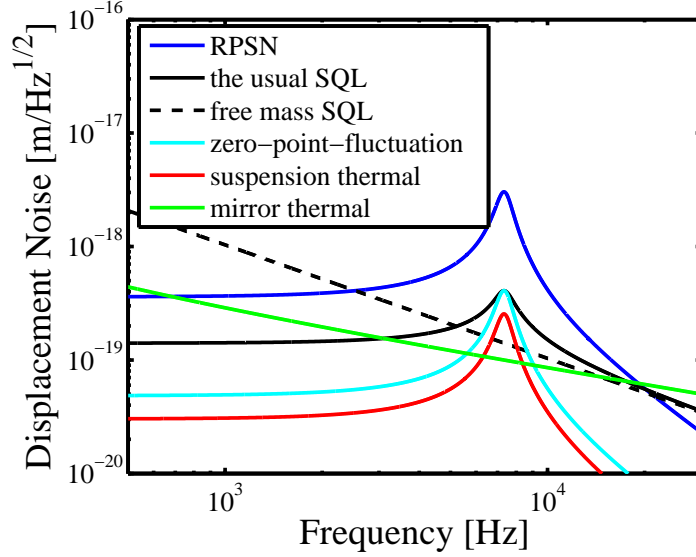


Figure 7.1: **Plan1**. The quantum back-action (blue), the suspension thermal noise (red), the mirror thermal noise (green), the zero-point fluctuation (cyan), the SQL for the free mass (dotted black) and the usual (for the people belonged to GW detectors) SQL for the modified mirror (black line) are shown. The parameters are listed in Table 7.1.

Table 7.1: **Parameter list of Fig. 7.1**

Parameter	Value	Unit
finesse	$1.0 \times 10^4$	-
cavity decay rate	0.9	MHz
Q-value of the pendulum	$5.0 \times 10^6$	-
Q-value of the substrate	$1.0 \times 10^6$	-
effective resonant frequency	7.4	kHz
effective Q-value	8.4	-
input power (driving)	250	mW
input power (spring)	1500	mW
normalized detuning (driving)	-1.0	-
normalized detuning (spring)	2.5	-

In order to experimentally test a quantization of spacetime for exploring quantum gravitational phenomena, a massive object should be cooled almost in its ground state[111]. Ground-state cooling has been realized[10, 11, 12]; however, it has not been realized on the macroscopic mass scale.

From Eqs. (1.1) and (6.1), the relationship between the thermal fluctuation force and the SQL is given by

$$\frac{S_{\text{FF,th}}^{(2)}}{S_{\text{FF,SQL}}^{(2)}} = \frac{4k_{\text{B}}T\gamma_{\text{m}}m}{\hbar|\chi_{\text{m}}(\omega)|^{-1} + 2\hbar\omega_{\text{m}}\gamma_{\text{m}}m} \xrightarrow{\omega \rightarrow \omega_{\text{m}}} \frac{k_{\text{B}}T}{\hbar\omega_{\text{m}}}. \quad (7.1)$$

Therefore, (it is regarded as at the high-temperature limit), the occupation number becomes unity when the thermal noise and the SQL are equal. (Correctly, the occupation number,  $1/(\exp(\hbar\omega_{\text{m}}/k_{\text{B}}T) - 1)$ , becomes about 0.58, in this case.)

In our case, due to the bad cavity condition, reducing the quantum back-action is challenging; however, the thermal excitation can be sufficiently removed. The phonon occupation number,  $\langle n \rangle = 0.22$ , is reachable, as shown in Fig. 7.1. To reduce the effect of back-action, one can use the QND method like the variational readout; however, the optical loss,  $\mathcal{L}$ , which makes the vacuum fluctuation to be superposed with the signal, degrades the effect. The SQL beating ratio by the variational readout method is given by  $\mathcal{L}^{1/4}$ [109]. In our case, the loss must be smaller than  $10^{-4}$  for sufficiently removing the effect of the back-action. This is currently impossible due to the detection loss.

## 7.2 Towards beating the SQL

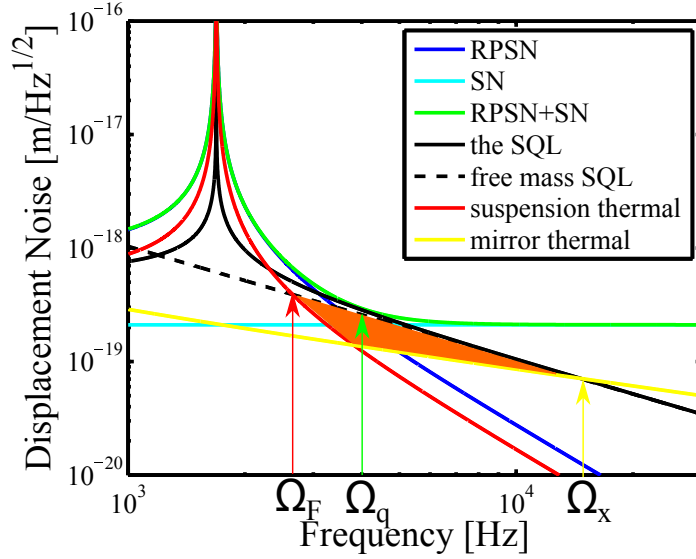


Figure 7.2: **Plan2**. The quantum back-action (blue), the shot noise (cyan), the suspension thermal noise (red), the mirror thermal noise (yellow), the SQL for the free mass (dotted black) and the SQL for the modified mirror (black line) are shown.  $\Omega_F$ ,  $\Omega_q$ , and  $\Omega_x$  are the frequencies at which the classical force noise (i.e., suspension thermal noise), quantum back-action, and classical sensing noise (i.e., the mirror thermal noise) intersect the free-mass SQL, respectively. The parameters are listed in Table 7.2.

Table 7.2: **Parameter list of Fig. 7.2**

Parameter	Value	Unit
finesse	4400	-
cavity decay rate	2.1	MHz
Q-value of the pendulum	$5.0 \times 10^6$	-
Q-value of the substrate	$1.0 \times 10^6$	-
effective resonant frequency	1.7	kHz
effective Q-value	1700	-
input power (driving)	10	mW
input power (spring)	100	mW
normalized detuning (driving)	-0.06	-
normalized detuning (spring)	3	-

In order to develop the gravitational-wave astronomy and testing quantum mechanics, respectively, it is necessary to overcome the SQL. To meet the criteria, we firstly have to realize the condition of  $\Omega_x/\Omega_F > 2$ . Under this condition, there is a nonzero frequency band (in between  $\Omega_F$  and  $\Omega_x$ ) in which the classical noise is completely below the SQL.

Fig. 7.2 shows the possible sensitivity ( $\Omega_F \sim 2700, \Omega_x \sim 15000$ ). The criteria can easily be realized, and thereby this is a suitable platform to experimentally study the QND technique.

Although the future view has been described as mentioned above, more detailed theoretical research is required.

# Conclusion

---

The observation of quantum back-action imposed on a macroscopic 5-mg mirror has been performed, and presented in this thesis. The quantum back-action is one of the most significant issues to be investigated regarding the interferometric gravitational-wave (GW) detectors because it will directly limit the sensitivity in next-generation detectors. Although the quantum back-action is just a noise for weak-force measurements, such as GW detectors, it is one of the key milestones concerning macroscopic quantum mechanics, such as the testing quantum measurement problems (Chapter 3). Until now, no one had observed the quantum back-action on the macroscopic scale (Chapter 1). To increase the optomechanical coupling and to reduce the thermal fluctuating force, an optical cavity with high circulating optical power must consist of a freely suspended mirror. However, the fundamental instability, called the Siddles-Sigg instability (i.e., optical anti-torsional spring effect), prevents their coexistence.

We thus developed an optical triangular cavity to overcome this limitation. In the case of this triangular cavity, the anti-torsional spring in pitch motion still occurs without any dependence on the isolation of the pendulum from the thermal bath. On the other hand, the anti-torsional spring in yaw motion changes the stable positive torsional spring (Chapter 4). The geometrical advantages of the triangular cavity enables for the mirror to be isolated from the thermal bath under a high intracavity power, and thus allowing us to use the powerful double optical spring, which also enables isolation from technical noise sources (Chapter 2 & 6). As a result, we were able to observe the quantum back-action (Chapter 5 & 6). Our result opens a new route to investigate ultra-sensitive force measurements and macroscopic quantum mechanics (Chapter 3 & 7). Both of them certainly go toward beating the standard quantum limit (SQL), and the only difference is the viewpoint from them. The former regards it as significant noise, and the latter regards it as a benchmark. Although reaching the SQL at the resonant point (so-called ground state cooling) is still challenging, due to the bad cavity condition, it can be reached at off-resonance by using our method in the future (Chapter 7). This condition is necessary to experimentally study the QND scheme for

GW detectors, and to generate macroscopic entanglement states. It is, therefore, a critical step toward gravitation wave astronomy and of macroscopic quantum measurements.

# APPENDIX A

## Intensity stabilization

---

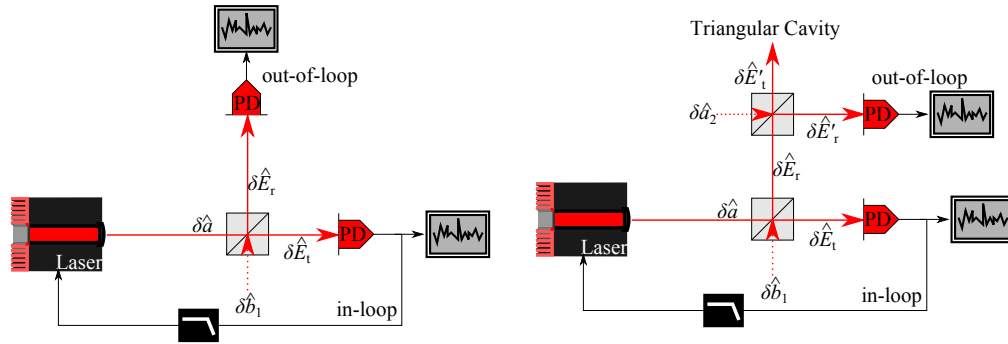


Figure A.1: **Intensity stabilization system. Left: Simplest case. Right: Our case.**

Here, we describe intensity stabilization using active feedback control. To start with, consider the simplest case, as shown in Fig. A.1(left). Since we only pay attention to the amplitude fluctuation of the electromagnetic field, only the amplitude quadrature is considered. The input laser and the vacuum fluctuation entering the unused port of the beam-splitter (BS) can be given by  $\delta\hat{a}$ ,  $\delta\hat{b}_1$ , respectively. A fluctuation component of a transmitted light from the BS labeled as  $\delta\hat{E}_t$  is given by

$$\delta\hat{E}_t = t_1\delta\hat{a} + r_1\delta\hat{b}_1, \quad (\text{A.1})$$

where  $r_1$  represents the amplitude reflectivity of the BS and  $t_1$  represents the amplitude transmittivity of the BS. On the other hand, the reflected light  $\delta\hat{E}_r$  is given by

$$\delta\hat{E}_r = -r_1\delta\hat{a} + t_1\delta\hat{b}_1. \quad (\text{A.2})$$

## A Intensity stabilization

---

If the transmitted light is used for stabilization, the negative-feedback system ideally reduces  $\delta\hat{E}_t$  to zero, and then

$$\delta\hat{a} = -\frac{r_1}{t_1}\delta\hat{b}_1 \quad (\text{A.3})$$

is obtained. The anti-correlation between  $\delta\hat{a}$  and  $\delta\hat{b}$  increases the noise level in the out-of-loop (i.e., the reflected field). It is given by

$$\delta\hat{E}_r = \frac{1}{t_1}\delta\hat{b}_1. \quad (\text{A.4})$$

Therefore, the maximum stability in the out-of-loop is  $1/t_1$ -times larger than the vacuum fluctuation. This effect is called the “noise penalty”. In our case, we used two half-BSs shown in Fig. A.1(right). Then, the maximum stability can be calculated as

$$\delta\hat{E}'_r = \sqrt{\left(\frac{r_2}{t_1}\right)^2 + t_2^2}\delta\hat{b}_1 \xrightarrow{t_1, t_2 \rightarrow 1/\sqrt{2}} \sqrt{\frac{3}{2}}\delta\hat{b}_1. \quad (\text{A.5})$$

Therefore, the achievable relative shot-noise level is reduced to about 1.8 dB. This satisfies our requirement (2 dB).

# Bibliography

---

- [1] Kepler, J. *De Cometis*, (1619).
- [2] Bartoli, A. G. *Sopra i movimenti prodotti dalla luce e dal calore*, (1876).
- [3] Lebedew, P. Untersuchungen über die Druckkräfte des Lichtes. *Ann. Phys.* **311**, 433 (1901).
- [4] Nichols, E.F & Hull, G.F. The Pressure due to Radiation, *The Astrophysical Journal*. **17**, 5 p.315-351 (1903).
- [5] Einstein, A. Entwicklung unserer Anschauungen über das Wesen und die Konstitution der Strahlung, *Phys. Z.* **10**, 817-825 (1909).
- [6] Hirakawa, H., Hiramatsu, S., & Ogawa, Y. DAMPING OF BROWNIAN MOTION BY COLD LOAD. *Phys Lett.* **63**, 3 (1977).
- [7] Ashkin, A. Trapping of Atoms by Resonance Radiation Pressure. *Phys. Rev. Lett.* **40**, 12 (1978).
- [8] Ashkin, A., Dziedzic, J. M., Yamane, T. Optical trapping and manipulation of single cells using infrared laser beams. *Nature*. **330**, 769-771 (1987).
- [9] Tongcang, L., Kheifets, S., Medellin, D., & Raizen, M. G. Measurement of the Instantaneous Velocity of a Brownian Particle. *Science*. **328**, 1673 (2010).
- [10] O'Connell, A. D., et al. Quantum ground state and single-phonon control of a mechanical resonator. *Nature*. **464**, 697-703 (2010).
- [11] Teufel, J. D., et al. Sideband cooling of micromechanical motion to the quantum ground state. *Nature*. **475**, 359-363 (2011).
- [12] Chan, J., et al. Laser cooling of a nanomechanical oscillator into its quantum ground state. *Nature*. **478**, 89-92 (2011).

- 
- [13] Purdy, T.P., Peterson, R. W., & Regal, C.A. Observation of radiation pressure shot noise on a macroscopic object. *Science*. **339**, 801 (2013).
- [14] Purdy, T.P., Yu P.-L., Peterson R.W., Kampel N.S., & Regal C.A. Strong optomechanical squeezing of light. *Phys. Rev. X*. **3**, 031012 (2013).
- [15] Matsumoto, N., Michimura, Y., Hayase, G., Aso, Y., & Tsubono, K. Classical Pendulum Feels Quantum Back-Action. *arXiv:1312.5031* (2013).
- [16] Braginsky, V. B., & Manukin, A. Ponderomotive Effects of Electromagnetic Radiation. *Sov. Phys. JETP* **25**, 653 (1967).
- [17] Braginsky, V. B., Gorodetsky, M. L., & Khalili, F. Ya. Optical bars in gravitational wave antennas. *Phys. Lett. A*. **232**, 340 (1997).
- [18] Braginsky, V. B., & Khalili, F. Ya. Low noise rigidity in quantum measurements. *Phys. Lett. A*. **257**, 241 (1999).
- [19] Sheard, B. S., Gray, M. B., Mow-Lowry, C. M., & McClelland, D. E. Observation and characterization of an optical spring. *Phys. Rev. A*. **69**, 051801(R) (2004).
- [20] Corbitt, T. et al. An all-optical trap for a gram-scale mirror. *Phys. Rev. Lett.* **98**, 150802 (2007).
- [21] Dorsel, A., McCullen, J. D., Meystre, P., Vignes, E., & Walther, H. Optical bistability and mirror confinement induced by radiation pressure. *Phys. Rev. Lett.* **51**, 17 (1983).
- [22] Braginsky, V. B., Vyatchanin, S. P. Parametric oscillatory instability in Fabry-Perot interferometer. *Phys. Lett. A*. **287**, 331-338 (2001).
- [23] Carmon, T., Rokhsari, H., Yang, L., Kippenberg, J., & Vahala, J. Temporal Behavior of Radiation-Pressure-Induced Vibrations of an Optical Microcavity Phonon Mode. *Phys. Rev. Lett.* **94**, 223902 (2005).
- [24] Sidles, J.A., & Sigg, D. Optical torques in suspended Fabry-perot interferometers. *Phys. Lett. A*. **354**, 167-172 (2006).
- [25] Sakata, S., Miyakawa, O., Nishizawa, A., Ishizaki, H., & Kawamura, S. Measurement of angular antispring effect in optical cavity by radiation pressure. *Phys. Rev. D*. **81**, 064023 (2010).

- [26] Heisenberg, W. Über den anschaulichen Inhalt der quantentheoretischen Kinematik und Mechanik. *Z. Phys.* **43**, 172-198 (1927).
- [27] Braginsky, V. B., & Khalili, F. Ya. *Quantum Measurement*. Cambridge University Press, Cambridge, England, (1992).
- [28] Braginsky, V. B., & Khalili, F. Ya., *Quantum Measurements*. (Cambridge University Press). (1995).
- [29] Caves, C. M. Quantum-mechanical noise in an interferometer. *Phys. Rev. D.* **23**, 8 (1981).
- [30] Kimble, H. J., Levin, Y., Matsko, A. B., Thorne, K. S., & Vyatchanin, S. P. Conversion of conventional gravitational-wave interferometers into quantum nondemolition interferometers by modifying their input and/or output optics. *Phys. Rev. D.* **65**, 022002 (2001).
- [31] Goda, K. et al. A quantum-enhanced prototype gravitational-wave detector. *Nature Physics.* **4**, 472-476 (2008).
- [32] Buonanno, A., & Chen, Y. Optical noise correlations and beating the standard quantum limit in advanced gravitational-wave detectors. *Class. Quantum Grav.* **18**, L95-L101 (2001).
- [33] Buonanno, A., & Chen, Y. Quantum noise in second generation, signal-recycled laser interferometric gravitational-wave detectors. *Phys. Rev. D.* **64**, 042006 (2001).
- [34] Buonanno, A., & Chen, Y. Signal recycled laser-interferometer gravitational-wave detectors as optical springs. *Phys. Rev. D.* **65**, 042001 (2002).
- [35] Braginsky, V. B., Vorontsov, Y. I., & Thorne, K. S. Quantum Nondemolition Measurements. *Science.* **209**, 4456 (1980).
- [36] Purdue, P., & Chen, Y. Practical speed meter designs for quantum nondemolition gravitational-wave interferometers. *Phys. Rev. D.* **66**, 122004 (2002).
- [37] Chen, Y., Danilishin, S. L., Khalili, F. Ya., & Müller-Ebhardt, H. QND measurements for future gravitational-wave detectors. *Gen. Relativ Gravit.* **43**, 671-694 (2011).

- [38] Mancini, S., & Tombesi, P. Quantum noise reduction by radiation pressure. *Phys. Rev. A*. **49**, 5 (1994).
- [39] Fabre, C., et al. Quantum-noise reduction using a cavity with a movable mirror. *Phys. Rev. A*. **49**, 2 (1994).
- [40] Brooks, D.W.C., et al. Non classical light generated by quantum-noise-driven cavity optomechanics. *Nature*. **488**, 476-480 (2012).
- [41] Safavi-Naeini, A.H., et al. Squeezed light from a silicon micromechanical resonator. *Nature*. **500**, 185-189 (2013).
- [42] Mancini, S., Giovannetti, V., Vitali, D., & Tombesi, P. Entangling Macroscopic Oscillators Exploiting Radiation Pressure. *Phys. Rev. Lett.* **88**, 12 (2002).
- [43] Pinard, M., et al. Entangling movable mirrors in a double-cavity system. *Europhys.* **72**, 747-753 (2005).
- [44] Müller-Ebhardt, H., Rehbein, H., Schnabel, R., Danzmann, K., & Chen, Y. Entanglement of Macroscopic Test Masses and the Standard Quantum Limit in Laser Interferometry. *Phys. Rev. Lett.* **100**, 013601 (2008).
- [45] Mazzola, L., & Paternostro, M. Distributing fully optomechanical quantum correlations. *Phys. Rev. A*. **83**, 062335 (2011).
- [46] Vitali, D., et al. Optomechanical Entanglement between a Movable Mirror and a Cavity Field. *Phys. Rev. Lett.* **98**, 030405 (2007).
- [47] Paternostro, M., et al. Creating and Probing Multipartite Macroscopic Entanglement with Light. *Phys. Rev. Lett.* **99**, 250401 (2007).
- [48] Joshi, C., Larson, J., Jonson, M., Andersson, E., & Öhberg, P. Entanglement of distant optomechanical systems. *Phys. Rev. A*. **85**, 033805 (2012).
- [49] Mial, H., Danilishin, S., & Chen, Y. Universal quantum entanglement between an oscillator and continuous fields. *Phys. Rev. Lett.* **81**, 052307 (2010).
- [50] Korneev, L. K.; Tssander, F. A. *Problems of flight by jet propulsion interplanetary flights*.

- [51] Jiang, H-R., Yoshinaga, N., & Sano, M. Active Motion of a Janus Particle by Self-Thermophoresis in a Defocused Laser Beam. *Phys. Rev. Lett.* **105**, 268302 (2010).
- [52] Cole, G. D., & Aspelmeyer, M. Cavity optomechanics Mechanical memory sees the light. *Nature Nanotechnology.* **6**, 690-691 (2011).
- [53] Wang, Y-D., & Clerk, A. A Using Interference for High Fidelity Quantum State Transfer in Optomechanics. *Phys. Rev. Lett.* **108**, 153603 (2012).
- [54] Stannigel, K., Rabl, P., Sørensen, A. S., Zoller, P. & Lukin, M. D. Optomechanical Transducers for Long-Distance Quantum Communication. *Phys. Rev. Lett.* **105**, 220501 (2010).
- [55] Weis, S. et al. Optomechanically Induced Transparency. *Science.* **330**, 1520 (2010).
- [56] Zhang, J., Peng, K., & Braunstein L. Quantum-state transfer from light to macroscopic oscillators. *Phys. Rev. Lett.* **68**, 013808 (2003).
- [57] Palomaki, T. A., Harlow, J. W., Teufel, J. D., Simmonds, R. W., & Lehnert, K. W. Coherent state transfer between itinerant microwave fields and a mechanical oscillator. *Nature.* **495**, 14 (2013).
- [58] Tsuda, Y. et al. Achievement of IKAROS – Japanese deep space solar sail demonstration mission. *Acta Astronautica.* **82**, 183-188 (2013).
- [59] Harry, G.M., et al. Advanced LIGO: the next generation of gravitational wave detectors. *Class Quantum Gravity.* **27**, 084006 (2010).
- [60] Somiya, K. Detector configuration of KAGRA-the Japanese cryogenic gravitational-wave detector. *Class. Quantum Grav.* **29**, 12 (2012). ; Aso, Y. et al. Interferometer design of the KAGRA gravitational wave detector. *Phys. Rev. D.* **88**, 043007 (2013). ;<http://gwcenter.icrr.u-tokyo.ac.jp/en/>
- [61] <http://www.geo600.uni-hannover.de>
- [62] <http://wwwcascina.virgo.infn.it>
- [63] Giessibl, F. J. Advances in atomic force microscopy. *Rev. Mod. Phys.* **75**, 949-983 (2003).

- [64] Westphal, T., et al. Interferometer readout noise below the standard quantum limit of a membrane. *Phys. Rev. A*. **85**, 063806 (2012).
- [65] Khalili, F. Ya., et al. Quantum back-action in measurements of zero-point mechanical oscillations. *Phys. Rev. A*. **86**, 033840 (2012).
- [66] Braginsky, V. B., et al. Noise in gravitational-wave detectors and other classical-force measurements is not influenced by test-mass quantization. *Phys. Rev. D*. **67**, 082001 (2003).
- [67] Braginsky, V. B. & Khalili, F. Ya. Quantum nondemolition measurements: the route from toys to tools. *Rev. Mod. Phys.* **68**, 1-11 (1996).
- [68] Murch, K.W., Moore, K.L., Gupta, S., & Stamper-Kurn, D.-M. Observation of quantum-measurement backaction with an ultracold atomic gas. *Nature Phys.* **4**, 561-564 (2008).;  
<http://ultracold.physics.berkeley.edu/pmwiki/Main/E3>
- [69] Safavi-Naeini, A.H., et al. Observation of quantum motion of a nanomechanical resonator. *Phys. Rev. Lett.* **108**, 033602 (2012).
- [70] Okutomi, A., Yamamoto, K., Miyoki, S., Ohashi, M., & Kuroda, K. Development of a radiation pressure noise interferometer. *Journal of Physics: Conference Series*. **32**, 327-332 (2006).
- [71] Mow-Lowry, C. M., et al. Towards the SQL: Status of the direct thermal-noise measurements at the ANU. *Journal of Physics: Conference Series*. **32**, 362-367 (2006).
- [72] Verlot, P., et al. Towards the experimental demonstration of quantum radiation pressure noise. *C. R. Physique*. **12**, 826-836 (2011).
- [73] Weinberg, S. *The Quantum Theory of Fields*. Cambridge University Press, (1995).
- [74] Scully, M. O., & Zubairy, M. S. *Quantum Optics*. Cambridge, (1997).
- [75] Rüdiger, A. et al. A mode selector to suppress fluctuations in laser beam geometry. *Optica. Acta*. **28**, 641 (1981).
- [76] Walls, D. F. & Milburn, G. J. *Quantum Optics*. Springer-Verlag, (1994).

- [77] White, A. G. Classical and quantum dynamics of optical frequency conversion. PhD thesis, Physics Department, The Australian National University, Canberra, Australia, (1995).
- [78] McKenzie, K. Squeezing in the Audio Gravitational Wave Detection Band. PhD thesis, Physics Department, The Australian National University, Canberra, Australia, (2008).
- [79] Callen, H. B., & Welton, T. A. Irreversibility and Generalized Noise. *Phys. Rev.* **83**, 1 (1951).
- [80] Gonzalez, G. I., & Saulson, P. R. Brownian motion of a mass suspended by an anelastic wire. *J. Acoust. Soc. Am.* **96**, 1 (1994).
- [81] Numata, k., et al. Measurement of the intrinsic mechanical loss of low-loss samples using a nodal support. *Phys. Rev. A.* **276**, 37 (2000).
- [82] Numata, K., et al. Measurement of the mechanical loss of crystalline samples using a nodal support. *Phys. Rev. A.* **284**, 162 (2001).
- [83] Cole, G. D., Wilson-Rae, I., Werbach, K., Vanner, M. R., & Aspelmeyer M. Phonon-tunnelling dissipation in mechanical resonators. *Nat. Commun.* **2**, 231 (2011).
- [84] Gonzalez, G., & Saulson, P. R. Brownian motion of a torsion pendulum with internal friction. *Phys. Rev. A.* **201**, 1 (1995).
- [85] Saulson, P.R. Thermal noise in mechanical experiments. *Phys. Rev. D.* **42**, 8 (1990).
- [86] Corbitt, T., et al. Optical Dilution and Feedback Cooling of a Gram-Scale Oscillator to 6.9 mK. *Phys. Rev. Lett.* **99**, 160801 (2007).
- [87] Chang, D. E., Ni, K. -K., Painter, O., & Kimble, H. J. Ultrahigh-Q mechanical oscillators through optical trapping. *New Journal of Physics.* **14**, 045002 (2012).
- [88] Ni, K. -K., et al. Enhancement of Mechanical Q Factors by Optical Trapping. *Phys. Rev. Lett.* **108**, 214302 (2012).
- [89] Law, C. K. Interaction between a moving mirror and radiation pressure: A Hamiltonian formulation. *Phys. Rev. A.* **51**, 3 (1995).

- [90] Wilson-Rae, L., Nooshi, N., Zwerger, W., & Kippenberg, T. J. Theory of Ground State Cooling of a Mechanical Oscillator Using Dynamical Back-action. *Phys. Rev. Lett.* **99**, 093901 (2007).
- [91] Marquardt, F., Chen, J. P., Clerk, A. A. & Girvin, S. M. Quantum Theory of Cavity-Assisted Sideband Cooling of Mechanical Motion. *Phys. Rev. Lett.* **99**, 093902 (2007).
- [92] Einstein, A. Näherungsweise Integration der Feldgleichungen der Gravitation. *Sitzungsbericht Preuss. Akad. Wiss.* **688**, (1916).
- [93] Taylor, J. H., & Weisberg, J. M. Further experimental tests of relativistic gravity using the binary pulsar PSR 1913+ 16. *Astrophys. J.* **345**, 434 (1989).
- [94] Saulson, P. R. If light waves are stretched by gravitational waves, how can we use light as a ruler to detect gravitational waves? *Am. J. Phys.* **65**, 6 (1997).
- [95] Heidmann, A., Hadjar, Y., & Pinard, M. Quantum nondemolition measurement by optomechanical coupling. *Appl. Phys.* **64**, 173-180 (1997).
- [96] Chelkowski, S., et al. Experimental characterization of frequency-dependent squeezed light. *Phys. Rev. A.* **71**, 013806 (2005).
- [97] Isogai, T. (personal communication).
- [98] Arndt, M., et al. Wave-particle duality of C<sub>60</sub> molecules. *Nature.* **401**, 680-682 (1999).
- [99] Gerlich, S., et al. Quantum interference of large organic molecules. *Nat. Commun.* **2**, 263 (2011).
- [100] Joos, E., & Zeh, H.D. The emergence of classical properties through interaction with the environment. *Z. Phys. B - Condensed Matter.* **59**, 223-243 (1985).
- [101] Zurek, W.H. Decoherence, einselection, and the quantum origins of the classical. *Reviews of Modern Physics.* **75**, 3 (2003).

- 
- [102] Hackermüller, L., Hornberger, K., Brezger, B., Zeilinger, A., & Arndt, M. Decoherence of matter waves by thermal emission of radiation. *Nature*. **427**, 19 (2004).
- [103] Pikovski, I., Zych, M., Costa, F., & Brukner, C. Universal decoherence due to gravitational time dilation. arXiv:1311.1095v1 (2013).
- [104] Everett, III, H. "Relative State" formulation of quantum mechanics. *Rev. Mod. Phys.*, **29**, 454 (1957).
- [105] Bassi, A., Lochan, K., Satin, S., Singh, T.P., & Ulbricht, H. Models of wave-function collapse, underlying theories, and experimental tests, *Rev. Mod. Phys.* **85**, 2 (2013).
- [106] Diósi, L. Models for universal reduction of macroscopic quantum fluctuations. *Phys. Rev. A*. **40**, 3 (1989).
- [107] Penrose, R. On gravity's role in quantum state reduction. *Gen. Relativ. Gravit.* **28**, 5 (1996).
- [108] Kaltenbaek, R., et al. Macroscopic quantum resonators (MAQRO). *Exp. Astron.* **34**, 123-164 (2012).
- [109] Miao, H. Exploring Macroscopic Quantum Mechanics in Optomechanical Devices. PhD thesis, Physics Department, The University of Western Australia, Australia, (2010).
- [110] Miao, H., et al. Probing macroscopic quantum states with a sub-Heisenberg accuracy. *Phys. Rev. A*. **81**, 012114 (2010).
- [111] Pikovski, I., Vanner, M.R., Aspelmeyer, M., Kim, M.S., & Brukner, C. Probing Planck-scale physics with quantum optics. *Nature Physics*. **8**, 2262 (2012).
- [112] Müller-Ebhardt, H., et al. Quantum-state preparation and macroscopic entanglement in gravitational-wave detectors. *Phys. Rev. A*. **80**, 043802 (2009).
- [113] Aurelian, I. ENTANGLEMENT DYNAMICS IN OPEN SYSTEMS. *Romanian Reports in Physics*. **61**, 4 (2009).

- 
- [114] Kawazoe, F., Schilling, R., & Lück, H. Eigenmode changes in a misaligned triangular optical cavity. *J. Opt.* **13**, 055504 (2011).
- [115] Sigg, D. Angular stability in a triangular fabry-perot cavity. LIGO-T030275-00, [www.ligo.caltech.edu/docs/T/T030275-00.pdf](http://www.ligo.caltech.edu/docs/T/T030275-00.pdf) (2003).
- [116] Neben, A. R., et al. Structural thermal noise in gram-scale mirror oscillators. *New Journal of Physics.* **14**, 115008 (2012).
- [117] Kawamura, S. (personal communication).
- [118] Taubman, M. S., Wiseman, H., McClelland, D. E., & Bachor, H-A. Intensity feedback effects on quantum-limited noise. *J. Opt. Soc. Am.* **12**, 10 (1995).
- [119] Numata, K. Direct measurement of mirror thermal noise, PhD thesis, Department of Physics, Faculty of Science, University of Tokyo, Tokyo, Japan, (2002).
- [120] Kwee, P., Willke, B., & Danzmann, K. Shot-noise-limited laser power stabilization with a high-power photodiode array. *Optics Letters.* **34**, 19 (2009).
- [121] Liu, L., et al. Measurement of the effect of a thin discharging wire for an electrostatic inertial sensor with a high-quality-factor pendulum. *Class. Quantum Grav.* **29**, 055010 (8pp) (2012).